Data Driven Control of DERs & Hybrid PV Plants for Enhancing Voltage Stability with TSO-DSO Interactions Over Multiple Timescales

Final Project Report

S-96

Power Systems Engineering Research Center
Empowering Minds to Engineer
the Future Electric Energy System

Data Driven Control of DERs & Hybrid PV Plants for Enhancing Voltage Stability with TSO-DSO Interactions Over Multiple Timescales

Final Project Report

S-96

Project Team
Venkataramana Ajjarapu, Project Leader
Iowa State University

Hugo Villegas Pico
Iowa State University

Sanjeev Pannala
Washington State University

Graduate Students
Muhammad Sarwar
Abdelrehman Mannan
Iowa State University

Liadi Akande
Washington State University

PSERC Publication 23-05

November 2023

For information about this project, contact:

Venkataramana Ajjarapu,
Iowa State University,
Department of Electrical and Computer Engineering,
Ames, Iowa, USA 50011-3060
Phone: 515-294-7687
Email: vajjarap@iastate.edu

Power Systems Engineering Research Center

The Power Systems Engineering Research Center (PSERC) is a multi-university Center conducting research on challenges facing the electric power industry and educating the next generation of power engineers. More information about PSERC can be found at the Center's website: http://www.pserc.wisc.edu.

For additional information, contact:

Power Systems Engineering Research Center
Arizona State University
527 Engineering Research Center
Tempe, Arizona 85287-5706
Phone: 480-965-1643
Fax: 480-727-2052

Acknowledgments

We express our appreciation for the support provided by PSERC's industry members and thank the industry advisors for this project:

- Bruno Leonardi, EPRI
- Deepak Ramasubramanian, EPRI
- Alberto Del Rosso, EPRI
- Fathalla Eldali, NRECA
- Venkat Banunarayanan, NRECA
- Chetan Mishra, Dominion
- Harvey Scribner, SPP
- Casey Cathey, SPP
- Doug Bowman, SPP
- Sally Thomas, First Energy
- Kun Zhu, MISO
- Yingchen Zhang, NREL
- Ben Kroposki, NREL
- Panitarn Chongfuangprinya, Hitachi
- Wei Qiu, NERC
- Manu Parashar, GE
- Aftab Alam, CAISO
- Ran Xu, CAISO

Executive Summary

There is increasing pressure on power system operators and electric utilities to utilize the existing grid infrastructure to the maximum extent possible. This mode of operation leads the system to operate close to its limits and can lead to instability problems. There are several forms of voltage instability, and each type requires different techniques to monitor and control.

According to MISO's Renewable Integration Impact Assessment (RIIA) Report, as the penetration of Inverter-based Resources (IBRs) approaches greater than 30%, voltage and converter-driven stability concerns arise in the system. Fault-induced delayed voltage recovery (FIDVR) occurs when the post-fault voltage recovers to a pre-fault voltage very slowly. If left untreated, FIDVR can lead to a complete voltage collapse. Inverter-based resources (IBRs) have the potential to improve delayed voltage recovery by providing dynamic reactive power support. This work investigates the potential of IBRs to enhance power system voltage performance.

This project is divided into three major research thrusts:

Thrust 1: (V. Ajjarapu, Iowa State University)

- Thrust-1 focuses mainly on identifying control set-points for the hybrid-PV plants and DERs. It deals with the questions:
    - How do we coordinate hybrid PV plants and DERs with load control for the optimal voltage response?
    - How to properly exploit the capability of several inverters within a single hybrid power plant (PV + battery)?
    - How do we measure the effect of GFL/GFM inverter controls on the FIDVR performance?

Thrust 2: (Hugo Villegas, Iowa State University)

- Grid forming inverter controls to improve FIDVR while respecting inverter current limitation.

Thrust 3: (Sanjeev Pannala, Washington State University)

- Validation utilizing realistic T&D co-simulation testbed using RTDS and Opal-RT

Part I: Data-driven Hybrid PV Plant Control for mitigation of short-term voltage instability

As the bulk electric system operation is moving into an operation regime where the economics are more important than in the past, the system operates close to the operating points with more chance of voltage instability. An essential type of voltage instability is the short-term large disturbance voltage instability that is caused by increasing penetration of the induction motor and electronic loads.

The problem of monitoring and mitigating Fault-Induced Delayed Voltage Recovery (FIDVR) is addressed by utilizing the high sampling rate of PMUs and using data-driven control techniques to orchestrate hybrid PV plants to provide optimal dynamic var support to the system.

To find the optimal control settings of IBRs for dynamic reactive power support, the problem can be formulated as an optimal control problem. Due to the high dimensionality and high non-linearity in power systems, optimal control problems are computationally expensive to solve. So, a data-driven approach that only depends on the sensor measurements can overcome the curse of dimensionality. The data-driven agent can be trained in offline simulation and then can operate and control the system online.

To improve short-term voltage stability, deep RL-based control is used to train on the synthetic PMU measurements from the system. A deep RL agent requires an observations tuple, an action tuple, and a scalar reward function to evaluate each action. For voltage stability improvement, the observations are voltage measurements at specific buses. Control actions are real and reactive power setpoints for IBRs and the amount of flexible load to be controlled.

The key takeaway from this part is that utilizing PMU measurements and offline training of the deep RL agent will enable the utilities to detect the FIDVR phenomenon and automatically compute the control setpoints for hybrid PV plants to mitigate delayed voltage recovery. This capability, combined with flexible load control of the single-phase induction motors, can ensure that the FIDVR recovery meets the transient voltage criterion set by the reliability coordinators.

Part II: Grid forming Inverter Controls to Improve FIDVR While respecting Inverter Current Limitations

At present, grid-forming (GFM) inverter-based resources (IBRs), such as wind and solar, are expected to power the U.S. grid-like synchronous machines. However, one problem with this transition is that GFM IBRs powered by hybrid resources are still under research. Further, a major concern is that GFM IBRs cannot source over-rated currents, jeopardizing the starting up of SPIMs and the riding through of FIDVR events. Grid-forming inverters must optimally transfer power from dc-coupled photovoltaic arrays and batteries into an ac grid. Further, they must be able to restore single-phase induction motors (SPIMs) and withstand fault-induced delayed-voltage-recovery (FIDVR) events.

These resilience and reliability challenges are addressed here by:

(i) engineering a controller to operate dc-coupled hybrid resources optimally.
(ii) modeling residential air-conditioning compressors for restoration/FIDVR studies; and
(iii) analyzing SPIM thermal-relay performance under limited inverter currents and designing an electronic protection for stalled SPIMs.

These contributions are demonstrated via electromagnetic-transient simulations to satisfy recommendations by the North American Electric Reliability Corporation.

Part III: Real-Time Synchrophasor Measurements Based Long Term Voltage Stability Monitoring and Control

The WSU team worked on three topics under this task to validate the system using a real-time simulation testbed. The first task considered the ZIP load estimation from the distribution system to produce the aggregated load models to reflect accurate models at bulk power system levels considering DERs. Solar PV and Battery energy storage systems are considered within the distribution system and created an equivalent simulation model for different operating conditions. Besides, the team also worked on network-level aggregation to complement different feeder levels to generate a single equivalent network.

T&D co-simulation analysis was performed using benchmark systems from transmission and distribution sectors and applied different testing conditions from a distribution systems perspective to understand how noisy DER control impacts power system behavior.

Finally, the IEEE 9 bus system replicates the typical fault-induced delayed voltage recovery (FIDVR) from single-phase induction motors with and without a Hybrid Solar PV system. A detailed discussion with results is included in the report under specific sections.

Project Publications:

[1] M. Sarwar, A. R. R. Matavalam and V. Ajjarapu, "*Deep Reinforcement Learning Framework for Short-Term Voltage Stability Improvement*," 2023 IEEE Texas Power and Energy Conference (TPEC), College Station, TX, USA, 2023, pp. 1-6, doi: 10.1109/TPEC56611.2023.10078572.

[2] M. Sarwar, A. Reddy Ramapuram Matavalam and V. Ajjarapu, "*Characterization and Mitigation of Fault Induced Delayed Voltage Recovery with Dynamic Voltage Support by Hybrid PV Plants*," 2022 North American Power Symposium (NAPS), Salt Lake City, UT, USA, 2022, pp. 1-6, doi: 10.1109/NAPS56150.2022.10012146.

[3] Abdel Mannan, Hugo Pico, "*FIDVR Capability of Hybrid Grid-Forming PV Power Plants During Feeder Restoration*", submitted to IEEE Transactions on Energy Conversion

[4] Muhammad Sarwar and V. Ajjarapu, "*Deep Reinforcement Learning based Control of Inverter Based Resources for Voltage Stability Improvement*", To be submitted for publication, submitted to arXiv repository.

[5] S. M. H. Rizvi and A. K. Srivastava, "*Integrated T&D Voltage Stability Assessment Considering Impact of DERs and Distribution Network Topology*," in IEEE Access, vol. 11, pp. 14702-14714, 2023, doi: 10.1109/ACCESS.2023.3243100.

[6] N.Patari, S.Rizvi ,S.Pannala and A. Srivastava "*Aggregated ZIP Load Estimation Method for DER Integrated Distribution Systems",* submitted to IEEE PES Transaction.

Student Theses:

[1] Muhammad Sarwar, *Data Driven Control of Inverter Based Resources to Enhance Power System Voltage Performance*, PhD dissertation, Iowa State University, Ames IA, (In Progress).

[2] Abdelrehman Mannan, *Investigating the Performance of Grid-forming Hybrid Photovoltaic Systems in Residential A/C Dominated Networks: An analysis during distribution feeder restoration and FIDVR*, master's thesis, Iowa State University, Ames IA, (submitted).

[3] Qin, C. (2022). *Data-driven situational awareness for distribution system resiliency (Order No. 29326873)*. Available from Dissertations & Theses @ Washington State University WCLP

Part I

Data-driven DER and Hybrid PV Plant Control

Venkataramana Ajjarapu
Muhammad Sarwar, Graduate Student

Iowa State University

For information about this project, contact

Venkataramana Ajjarapu,
Iowa State University,
Department of Electrical and Computer Engineering,
Ames, Iowa, USA 50011-3060
Phone: 515-294-7687
Email: vajjarap@iastate.edu

Power Systems Engineering Research Center

The Power Systems Engineering Research Center (PSERC) is a multi-university Center conducting research on challenges facing the electric power industry and educating the next generation of power engineers. More information about PSERC can be found at the Center's website: http://www.pserc.wisc.edu.

For additional information, contact:

Power Systems Engineering Research Center
Arizona State University
527 Engineering Research Center
Tempe, Arizona 85287-5706
Phone: 480-965-1643
Fax: 480-727-2052

Notice Concerning Copyright Material

Table of Contents

List of Figures

List of Tables

1. Introduction

1.1 Background and Motivation

Electric power systems worldwide are undergoing a transformative phase, increasingly incorporating renewable energy resources, like photovoltaic (PV) systems and distributed energy resources (DERs), into the traditional grid. The promise of these technologies, coupled with data-driven approaches, brings forth the possibility of enhanced grid reliability and efficiency. This research delves deep into leveraging such opportunities, especially in the domain of voltage stability and coordination between transmission system operators (TSOs) and distribution system operators (DSOs).

In recent years, there has been a noticeable surge in the penetration of inverter-based resources in power system, particularly solar power plants, in the power system. This trend is primarily driven by a combination of technological advancements, decreasing costs, subsidies by federal & state governments, and global commitments to sustainable and renewable energy.

With the increasing penetration of renewable energy sources, power systems face new challenges in terms of voltage stability, especially during disturbances and high variability scenarios. DERs, including hybrid PV plants with storage, offer a promising solution by providing real-time active/reactive power support to stabilize voltage levels. However, effective control and coordination of these resources remain a significant challenge due to the intricate interplay between TSOs and DSOs, rapid changes in solar irradiance affecting PV outputs, and the real-time demands of the modern grid.

Solar power, while promising, presents inherent challenges such as intermittency and unpredictability. Hybrid PV plants, which couple solar PV plants with battery storage, are emerging as a promising solution. By storing excess energy produced during peak solar hours, these systems can provide a more consistent and reliable power supply. This integration effectively addresses the seasonal variations of solar generation, ensuring a smoother power curve and mitigating grid instability issues.

The US Energy Information Administration (EIA) anticipates a significant increase in the deployment of hybrid PV plants in the coming years as shown in Figure 1.1. Of the 14.5 gigawatts (GW) of battery storage power capacity planned to come online in the United States from 2021 to 2024, 9.4 GW (63%) will be co-located with a solar photovoltaic (PV) power plant. These forecasts are based on an increasing recognition of the benefits of combining solar generation with storage. As per EIA's estimates, this rise can be attributed to various factors, including economic advantages, grid resiliency, and federal/state incentives promoting renewable integrations. Regional trends also follow the EIA’s estimated, as shown from MISO’s generation interconnection queue of hybrid resources, as shown in Figure 1.2.

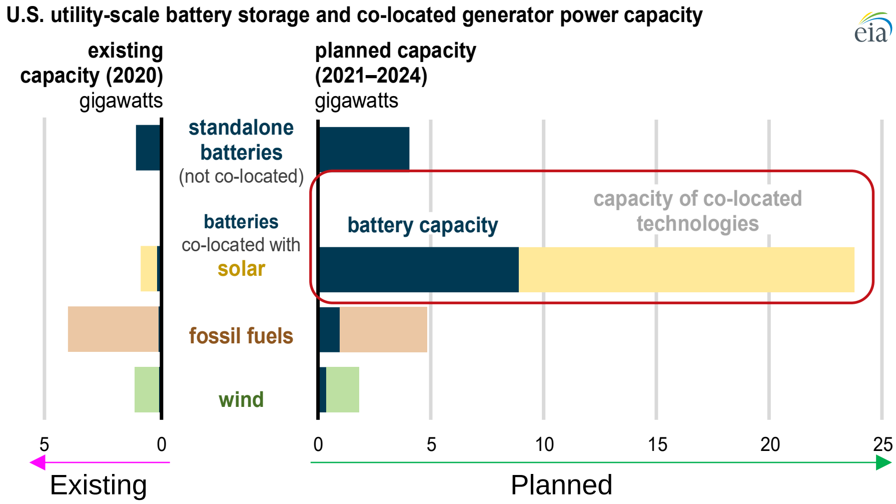

Figure 1.1 Planned capacity of renewable energy resources in the US according to US Energy Information Administration [1]

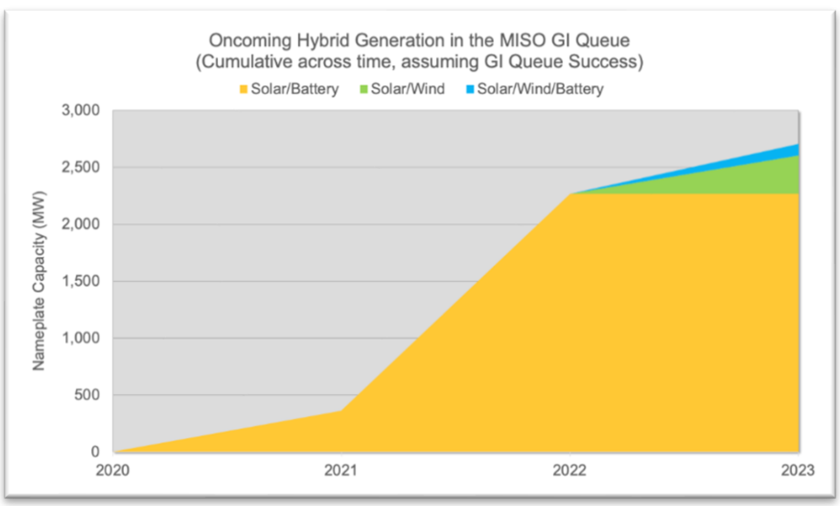

Figure 1.2 MISO's Generation Interconnection queue shoring the planned capacity for hybrid generation [2]

1.2 Problem Statement

As the bulk electric system operation is moving into an operation regime where the economics are more important than in the past, the system is operating close to the operating points with more chance of instability. Figure 1.3 provides the classification of power system stability as defined by the IEEE and CIGRE task force.

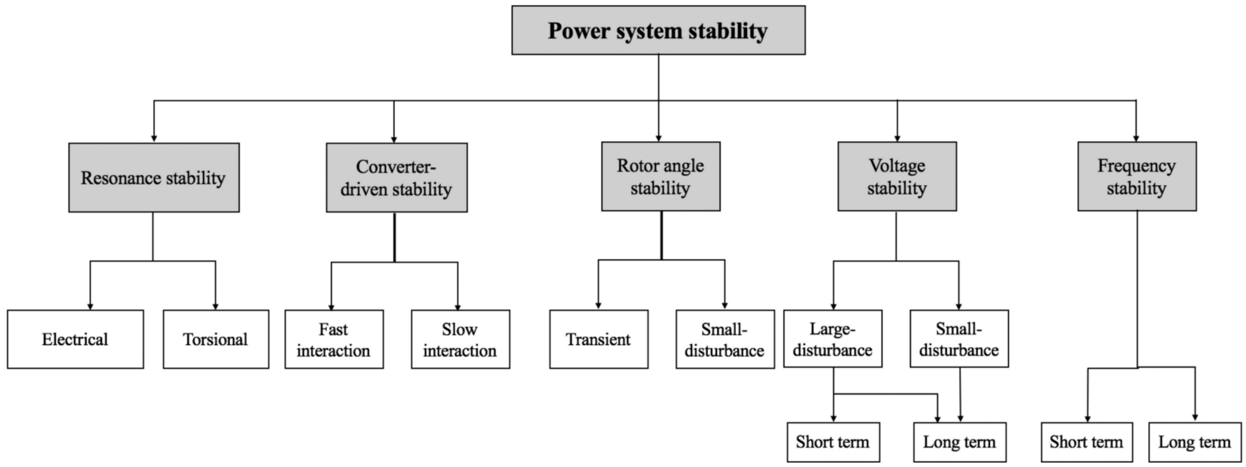

Figure 1.3 Classification of the various stability phenomenon in power systems [3]

As the percentage of renewable energy resources increases the power system, converter-driven and voltage stability issues arise in the system. According to MISO's Renewable Integration Impact Assessment (RIIA) Report [4], as the penetration of Inverter-based Resources (IBRs) approach greater than 30%, voltage and converter-driven stability concerns arise in the system. It is estimated that more than 90% of investments will be made to mitigate voltage and converter-driven stability problems for systems with greater than 30% penetration of IBRs. Fault-induced delayed voltage recovery (FIDVR) occurs when the post-fault voltage recovers to a pre-fault voltage very slowly. If left untreated, FIDVR can lead to a complete voltage collapse.

Inverter-based resources (IBRs) have the potential to improve delayed voltage recovery by providing dynamic reactive power support. To find the optimal control settings of IBRs for dynamic reactive power support, the problem can be formulated as an optimal control problem. Due to the high dimensionality and high non-linearity in power systems, optimal control problems are computationally expensive to solve. So, a data-driven approach which only depends on the sensor measurements can overcome the curse of dimensionality. The data-driven agent can be trained in offline simulation and then can operate and control the system in an online manner.

1.2.1 Objectives and Scope

As discussed in the previous section, this research focuses on the optimal utilization of hybrid PV to improve power systems voltage performance. The fundamental challenge is twofold: First, developing a controller for hybrid PV plants that reliably delivers the required active/reactive power to the bulk grid while being robust to disturbances and PV variability. Second, leveraging data-driven control techniques to develop a system-level control scheme to provide optimal dynamic voltage support from the hybrid PV plants. Addressing these challenges requires a data-driven approach that can make the most of real-time measurements from Phasor Measurement Units (PMUs) and accommodate the dynamics of hybrid PV plants while respected the physical limits of each inverter.

This research aims to:

- Detailed investigation of the delayed voltage recovery problem for solution through deep reinforcement learning
- Development of deep reinforcement learning (DRL) based control framework utilizing open-source libraries and industry-standard power system solver. A case study using the framework is given for optimal load control to mitigate FIDVR.
- Integration of hybrid PV plants using generic inverter-based resources control with conventional power system
- To characterize the delayed voltage recovery, an index based on the probability density function of the voltage waveform is studied, and two such indices are compared. It is shown that these indices fully characterize the voltage recovery of the system after a motor stalling.
- Moreover, this work analyzes different dynamic voltage support controls for PV plants and BESS and measures their impact on FIDVR using the indices developed.
- Use physics-based, data-driven techniques to exploit the full potential of hybrid PV plants, particularly storage, in mitigating voltage instability.

The scope of this project encompasses both the development of control strategies and their practical implementation, considering real-world challenges like noisy measurements and communication delays.

1.3 Report Organization

The report is organized as follows. Section 2 describes the Fault Induced Delayed Voltage Recovery phenomenon in detail and illustrates the various requirements by the reliability coordinators to ensure the compliance with voltage recovery criterion. The load model that can demonstrate FIDVR in software simulations (composite load model) and generic positive-sequence hybrid PV plant modes approved by WECC are also discussed in detail to illustrate the various components involved in the phenomenon. Section 3 gives the metric to characterize and quantify FIDVR using entropy-based measures. Section 4 describes the role of inverter-based resources in mitigating FIDVR. We explore different control modes to measure their impact on the delayed voltage recovery. Section 5 details of the data-driven control based on Deep Reinforcement learning and how it is used to mitigated FIDVR. Section 6 gives the conclusion and future extensions of this work.

2. Fault-Induced Delayed Voltage Recovery

Short-term large disturbance voltage stability is an increasing concern for industry because of the increasing penetration of induction motors and electronically controlled loads. While it is not analytically proven which power system components cause angle and voltage instability, recent work based on an information transfer metric in dynamical systems [5] seems to suggest that the induction motor loads are very much related to voltage instability. The short-term voltage instability is mainly caused by the stalling of induction motor loads and can manifest in the form of fast voltage collapse or delayed voltage recovery. One form of voltage stability is Fault Induced Delayed Voltage Recovery (FIDVR), which is the phenomenon in which the recovery of the voltage after a disturbance is delayed, resulting in sustained low voltages for several seconds (~15 sec).

2.1 Literature Review

The FIDVR phenomenon causes slow recovery of post-fault voltage and can cause a voltage collapse if the system is already operating on the verge of voltage stability. With faster converter response from inverter-based resources like PV plants and battery energy storage systems (BESS), the FIDVR response of the system can be improved. So, the central thesis of this research is that the output of hybrid PV plants (PV plants with BESS) can be controlled to enhance voltage response after a severe fault and decrease the voltage recovery time.

The problem of providing reactive power support using PV plants and BESS has attracted much interest from the research community. Reference [6] analyzes the impact of increasing penetration of PV generation on the power system. Although, the authors have not considered BESS in this paper.

2.1.1 Detection and Mitigation of FIDVR

The phenomenon of FIDVR has been studied by the authors of [7] and [8] using a simplified version of the WECC (Western Electricity Coordinated Council) Composite Load Model (CMLD) [9]. A delayed voltage recovery mitigation scheme using smart thermostats has been derived and tested using numerical simulations. Reference [10] proposes a dynamic voltage support capability using PV systems to improve short-term voltage stability. The proposed approach injects active and reactive power coordinated as a function of the terminal voltage.

A delayed voltage recovery mitigation scheme using linear optimization-based load control is given in [11]. PV inverters are used to inject additional reactive power to support the grid and improve post-fault voltage response [12].

Authors of reference [13] proposed a decentralized adaptive control system to prevent power system voltage instability. Intelligent agents monitor bus voltage and relative generator power in each zone to detect any possibility of voltage collapse when the system is stressed. In [14], a smart PV inverter has been developed to improve system response to frequency and voltage excursions. Different control schemes have been tested and validated to use smart PV inverters, and their effects on voltage and frequency are presented.

Since planning and commissioning a battery energy storage system is dictated mainly by either financial benefit or to provide reliability support mandates by regulatory authorities, it is imperative to look at the financial aspects of the battery energy storage system. A techno-economic analysis of the PV plants with a battery storage system is given in [15], [16].

NERC conducted a study to analyze the impact of electrochemical utility-scale BESS on the bulk power system [17]. The detailed report emphasizes some potential reliability benefits BESSs can provide, such as delivering peaking capacity, minimizing the need for the new generation and transmission infrastructure, and providing essential reliability services (e.g., frequency response, ramping, and voltage support).

Volt-var support by hybrid PV plants is an attractive strategy explored by researchers in the power system community. This technique intends to utilize the existing inverter installed for PV and BESS to provide dynamic voltage support to the bulk power system for improved system stability and reliability. The problem of volt-var support by hybrid PV plants needs further exploration in light of the NERC reliability guideline for inverter-based resources [18] and the latest IEEE Draft Standard for Interconnection and Interoperability of Inverter-Based Resources (IBR) Interconnecting with Associated Transmission Electric Power Systems [19].

2.1.2 Optimal Decision-Making in Power System

Current decision-making for emergency power system control can be categorized into

1) conventional optimal control [20],
2) conventional machine learning, such as decision trees [21], deep learning [22], and conventional reinforcement learning (RL) [23].

Optimal control methods are generally hard to scale to handle large-scale power systems with an increasing number of control devices as the distribution system is becoming more active. RL methods have been recently applied to various decision-making and control problems in power systems, including demand response [24], energy management, automatic generation control, and emergency control [25].

Conventional reinforcement learning is not salable for problems with high dimensional states and action spaces. Also, the quality of conventional RL methods is dependent on handcrafted features. So, they are generally not suitable for large, complex problems where an accurate system model is not available, e.g., power system dynamic control problems.

Recently, significant progress has been made in solving challenging large-scale problems using deep reinforcement learning (DRL), a combination of deep learning and conventional RL. Conventional RL uses hand-crafted features from input (such as Q-table); however, DRL uses deep learning for automatic high-dimensional feature extraction, thus dealing with large-scale complex environments efficiently.

Authors of [26] have explored the application of deep reinforcement learning (DRL or Deep RL) methods on power system emergency control to improve system short-term voltage performance using under-voltage load shedding (UVLS). The developed framework uses InterPSS [27] to simulate the power system.

The use of industry-standard software in DRL applications is very limited in literature and thus limits the adaptation by industry of any proposed solutions.

2.2 The phenomenon of Delayed Voltage Recovery in Power Systems

FIDVR is mainly caused in systems with a moderate amount of single-phase induction motor loads (25% ~ 30%). After a large disturbance (fault, etc.), these motors, which are connected to mechanical loads with constant torque, stall and typically draw 5-6 times their nominal current, and this leads to the depression of the system voltage for a significant amount of time. The low voltages in the system inherently lead to some load being tripped by protection devices close to the fault. However, even after this, the concern is that the sustained low voltages (>10 s) can lead to cascading events in the system, steering toward a blackout. A typical delayed voltage response after a fault, along with the various features, is shown in Figure 2.1.

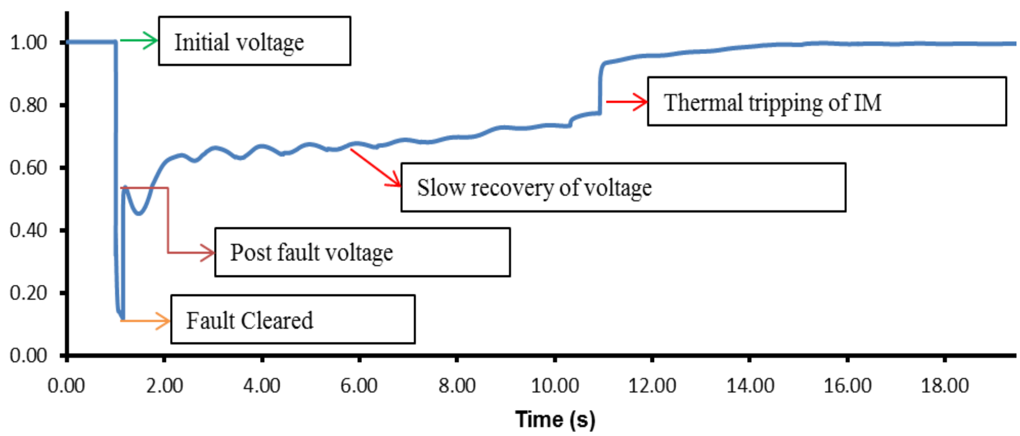

Figure 2.1 Conceptual delayed voltage recovery waveform at a bus.

Most single-phase induction motors are used in residential air-conditioners, and so the FIDVR phenomenon has been historically observed in systems where a large number of residential ACs are operational at the same time (e.g., summer in California or Arizona). Most of these devices do not use Under Voltage protection schemes and are only equipped with thermal protection with an inverse time-overcurrent feature, delaying the tripping up to 20s.

Description of several FIDVR events observed in the field are listed in [28], and almost all of the occur in high residential load areas during a period of high temperature. As an example, Figure 2.2 shows an FIDVR event on a 115kV bus in Southern California on July 24, 2004. The sustained low voltage is likely caused by stalled AC IMs, and the voltage finally recovered to pre-contingency voltage around 25s after the fault. Out of the substation load of 960 MW, 400 MW of load was tripped by protection devices in residential and commercial units to recover the voltage.

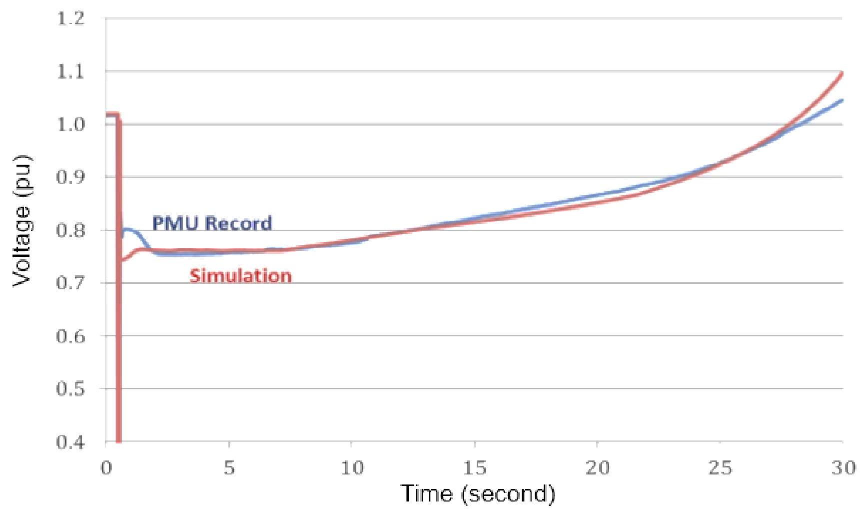

Figure 2.2 Recorded delayed voltage recovery waveform at a 115kV bus in Southern California on July 24, 2004 [28].

2.2.1 Transient Voltage Recovery Criteria

To prevent uncontrolled loss of load in the bulk electric system, NERC, WECC, and other regulatory bodies have specified transient voltage criteria that utilities and system operators need to satisfy after a fault has been cleared. Figure 2.3 provides a pictorial representation of the WECC criteria and the PJM criteria.

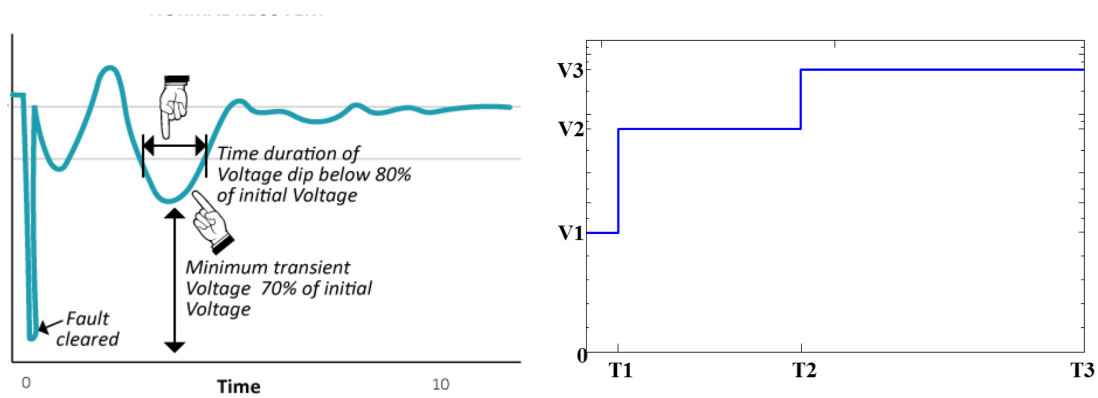

(a) (b)

Figure 2.3 (a) WECC transient voltage criteria [29] (b) Simplified voltage criteria [30].

The WECC transient criteria are defined as the following two requirements [29]

1. Following fault clearing, the voltage shall recover to 80% of the pre-contingency voltage within 20 seconds of the initiating event.
2. Following fault clearing and voltage recovery above 80%, the voltage at each applicable bulk electric bus serving load shall neither dip below 70% of pre-contingency voltage for more than 30 cycles nor remain below 80% of pre-contingency voltage for more than two seconds.

A simplified voltage criterion is generally used by utilities, and the trajectory of the recovering voltage must be above the curve in Figure 2.3(b), where $V_1 = 0.5, V_2 = 0.7$ & $V_3 = 0.95$ and $T_1 = 1\ s, T_2 = 5\ s$ & $T_3 = 10\ s$. The ERCOT criteria for transient voltage response requires that voltages recover to 0.90 p.u. Within 10 seconds of clearing the fault [31].

The utilities ensure that the voltage recovery satisfies the guidelines specified by their regulatory authority during their planning phase and operational phase by either installing VAR devices (STATCOM, SVC, etc.) in critical regions and by ensuring that sufficient dynamic VARS are available during operation.

2.3 Load Modelling for Simulation

2.3.1 WECC Composite Load Model

To enable the utilities and system operators to simulate the FIDVR phenomenon to estimate the amount of VAR support required, a dynamic load model has been developed recently by WECC called the Dynamic Composite Load Model. The composite model essentially aggregates the various kinds of dynamic loads in the sub-transmission network into several 3-ϕ IM (representing high, medium, and low inertias) and an aggregate 1-ϕ IM (representing the AC loads). Furthermore, the protection schemes that trip a proportion of the loads are also implemented for each of the motors, representing the Under Voltage and Under Frequency protection policies. An equivalent feeder is also present that tries to emulate the impact of voltage drop in the distribution system when a large current is drawn. The overall structure of the composite load model is shown in Figure 2.4, and the performance-based model of the 1-phase induction motor that is used in compositive load is shown in Figure 2.5.

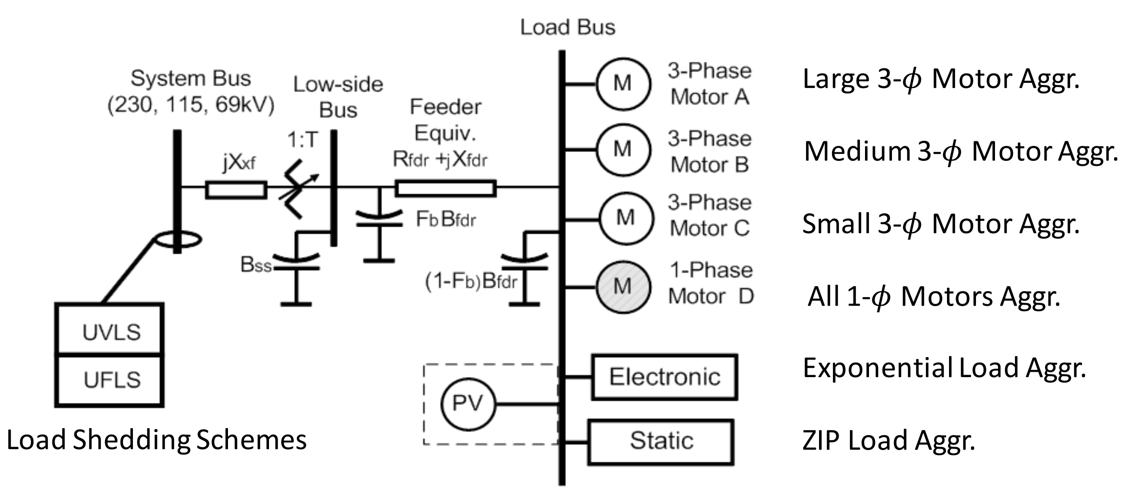

Figure 2.4 Structure of the composite load model [9]

This model has 132 parameters and has been implemented by vendors in commercial software such as PSSE, PSLF, and PowerWorld. More details, along with descriptions of the various parameters, can be found in [9]. As part of this project, the CMLD model is studied in detail in order to understand the behavior and simplify the model for control schemes to mitigate FIDVR or to ensure that the FIDVR phenomenon is taken care of within the time as specified by the corresponding operator (ERCOT/PJM/WECC).

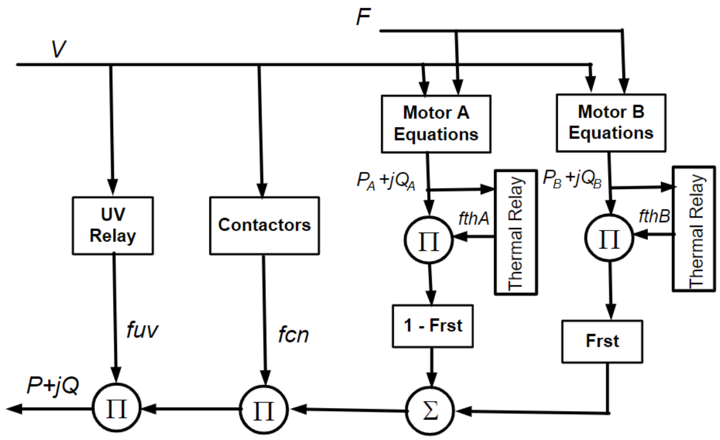

Figure 2.5 1-ph A/C motor performance-based model [9]

2.4 Examination of the WECC Composite Load Model

As the composite load model has a comparatively large number of parameters and discrete controls compared to a conventional load model, understanding the model and how the various parameters impact the voltage performance is important. Moreover, the model specifications [9] only mention the behavior of most of the components and do not specify the actual equations used. Thus, engineering judgment needs to be made with regard to developing equations for analysis. For this purpose, understanding the 3-phase IM model and the 1-phase IM model, along with their protection components, is key. These are detailed in the following sub-section.

2.4.1 3-Phase Motor Modelling

The 3-phase motor model block diagram is shown in Figure 2.6. The input parameters for this model are as follows:

- LFm --Loading factor –used to set motor MVA base
- Rs –Stator resistance (pu)
- Ls –Synchronous reactance (pu)
- Lp –Transient reactance (pu)
- Lpp –Subtransient reactance (pu)
- Tpo –Transient open circuit time constant (sec.)
- Tppo –Subtransient open circuit time constant (sec.

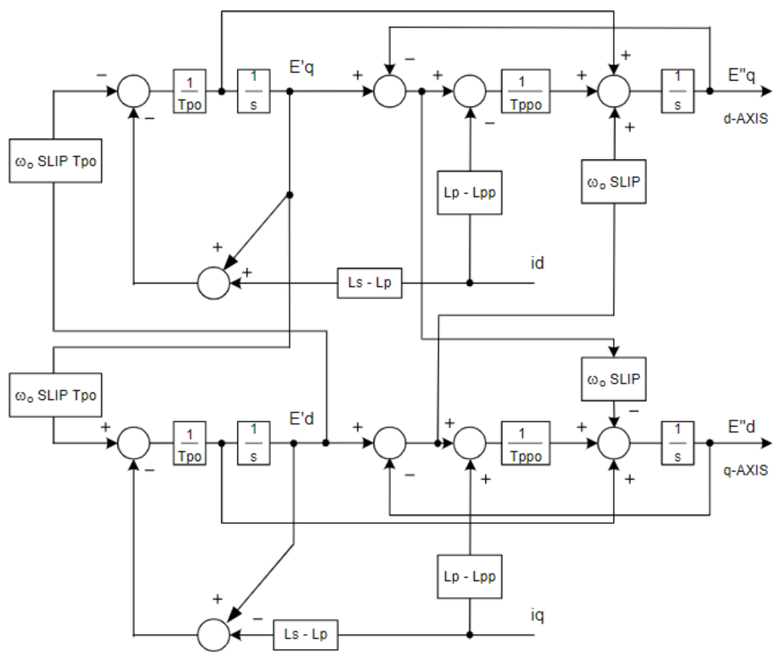

Figure 2.6 3-ph motor performance-based model for composite load [9]

A detail that is often overlooked is the behavior of the motor when a percentage of the load is tripped by UV relays. An intuitive method to achieve this is by reducing the mechanical torque by the same percentage to reflect this loss of load. While this indeed reduces the active power demanded, it does not reduce the reactive power demand. Some of the 3-ϕ motors are disconnected, and to properly reflect this physical scenario, the resistances of the equivalent circuit must be proportionally increased along with the reduction in the load torque. This ensures a reduction in both the active and reactive power demand.

2.4.2 1-Phase Motor Modelling

The 1-ϕ induction motor is the main reason why the FIDVR is observed. The 1-ϕ IM model has representations of the AC compressor motor, compressor motor thermal relay, under-voltage relays, and contactors. Depending upon the input voltage, the motor operates either in a 'running' or 'stalled' state. The behavior of the motor as a function of the voltage can be understood based on the power consumption of the motor, and Figure 2.7 plots the active and reactive power demand as a function of the voltage for the normal operation and stalled operation.

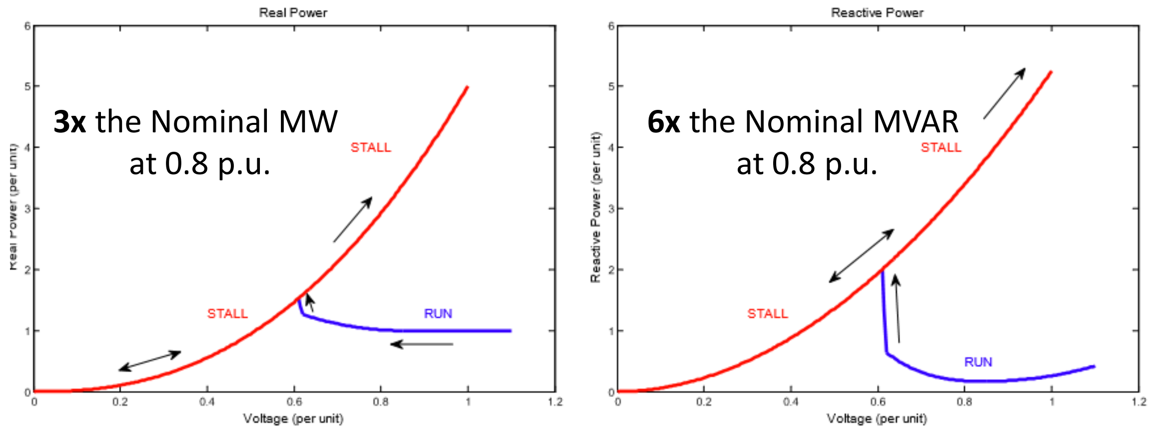

Figure 2.7 Active power (left) and Reactive power (right) versus the voltage for the normal operation and stalled operation for the $1-\phi$ induction motor [9].

From Figure 2.7, it can be seen that in the stalled state, the active power demand is 3 times the nominal amount, and the reactive demand is 6 times the nominal amount compared to the normal ‘running’ state. This large demand is the reason why the voltage reduces at the substation, causing FIDVR. This demand is naturally reduced via thermal protection, which takes around 10-15 seconds.

2.5 Modeling of IBRs (utility-scale and DERs) for Stability Studies

With the increasing penetration of Inverter-Based Resources (IBRs) in power systems, the complexity of power system dynamic response has increased due to intermittent characteristics of renewable energy resources and lower inertia. This restructuring of the power system has drastically impacted the system's dynamic performance, resulting in inter-area oscillations, lower synchronous coupling, frequency response, and voltage stability issues. Regulatory and balancing authorities have started mandating voltage support functionality from the hybrid PV plants to overcome some of these issues.

Traditionally, voltage regulation mainly relies on bulk synchronous generators' reactive power support, and FACTS devices-based voltage regulators, and load-side reactive power compensation. With increasing weather severity during summer, air conditioning load stresses the system due to increased reactive power demand and complicates the fault dynamics. As AC loads majorly consist of 1-phase induction motors, they have very peculiar post-fault load characteristics. After a fault, 1-phase motors stall and draw about 6-8 times more current than the nominal load current. This increased current further exacerbates the situation and causes a slow post-fault voltage recovery, formally known as Fault-Induced Delayed Voltage Recovery (FIDVR).

Voltage instability, often occurring in the form of a progressive decline or increase in voltage (long-term voltage stability), can lead to major system disturbances or blackouts if not addressed in a timely manner. In this context, the intrinsic characteristics of Hybrid PV Plants play an important role, especially with high inverter penetration. In this context, modeling of IBRs in the system plays an important role in studying the phenomenon of delayed voltage recovery.

To model hybrid PV plants for stability studies, we have followed WECC and EPRI guidelines using generic renewable energy converters (REGCA), electrical controllers for PV/BESS (REECB/REECC), and plant controllers (REPCA) included in PSS/E [32]. The topology of these controllers to model a utility-scale BESS or PV plant is shown in Fig. 2.8.

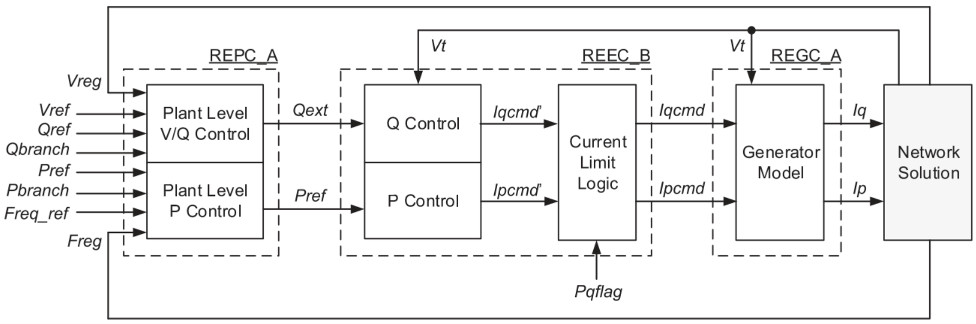

Figure 2.8: Block Diagrams of Different Modules of the WECC Generic Models for PV plant/BESS [32]

For DER modeling, we have considered aggregation at the composite load level. So, all the DERs within a distribution system have been aggregated on the transmission side in the form of DER in composite load. This reduced the computational complexity in the simulation. The block diagram of the plan and inverter level controllers are given in Figures 2.9 and 2.10.

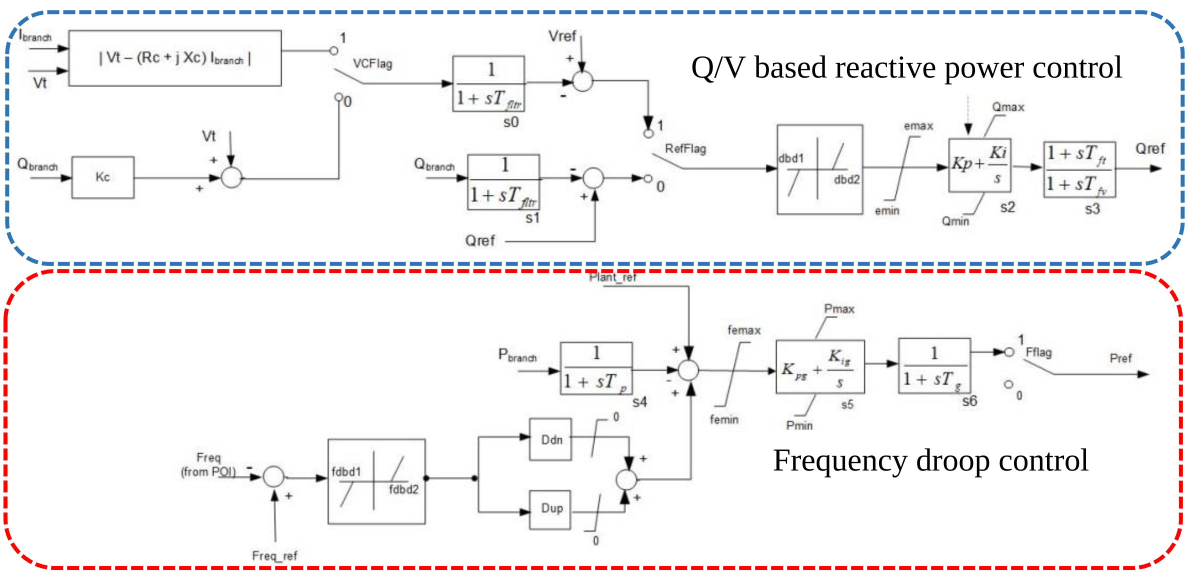

Figure 2.9 Plant level controller showing reactive and real power control loops based on REPC_* [32]

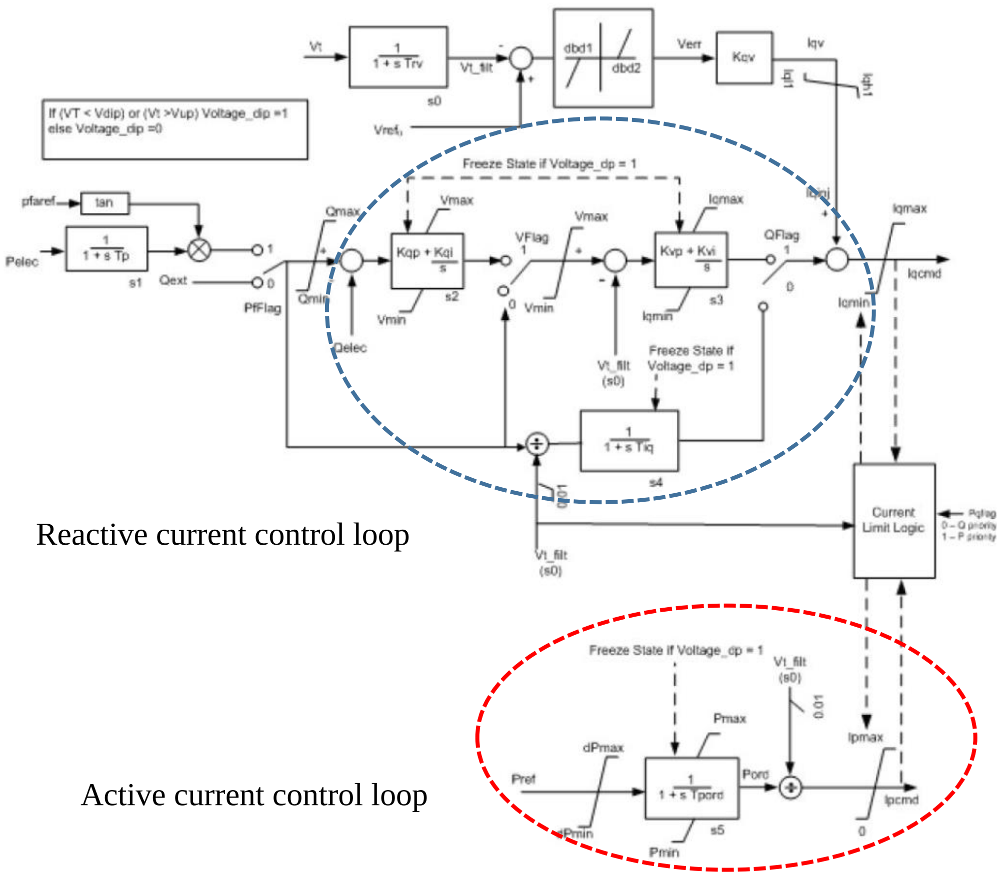

Figure 2.10 Inverter level controller based on REEC_* [32]

2.5.1 Grid Following (GFL) vs. Grid Forming (GFM) Inverters

Grid following and grid forming inverters differ in their operations, and this difference impacts the power system stability. Grid forming inverters use, e.g., a speed droop control law, to synthesize autonomously an artificial phase angle. Grid-following inverters use a phase-locked loop (PLL) to track the phase angle of externally generated voltages that are assumed to have stiff regulation, e.g., a set of synchronous machines in an interconnection (some are being displaced by inverters). A comparison of GFM vs. GFL inverters is given in Table 2.1.

Table 2.1 Comparison of grid-forming and grid-following inverters

	Grid-Forming Inverters	**Grid-Following Inverters**
Independency on externally generated voltages to operate?	yes (+)	no (-)
Semiconductor limitations to provide overrated currents?	yes	yes
Regulation of voltage waveform magnitudes?	yes	yes (if PLL is locked)

Regulation of voltage waveform angular frequency?	yes	no
Require stiff voltage sources for parallel operation?	no	yes (-)

2.5.2 EMT and Positive Sequence Domain Modeling

An EMT model for Grid Forming Inverter (GFM) was developed as part of the Thrust-2 of this project after prototyping and testing the GFM inverter model. It was converted to a positive sequence model for testing in the positive-sequence stability simulation in PSSE. The whole procedure for deducing the positive sequence model from the EMT model is shown in Figure 2.11-2.14.

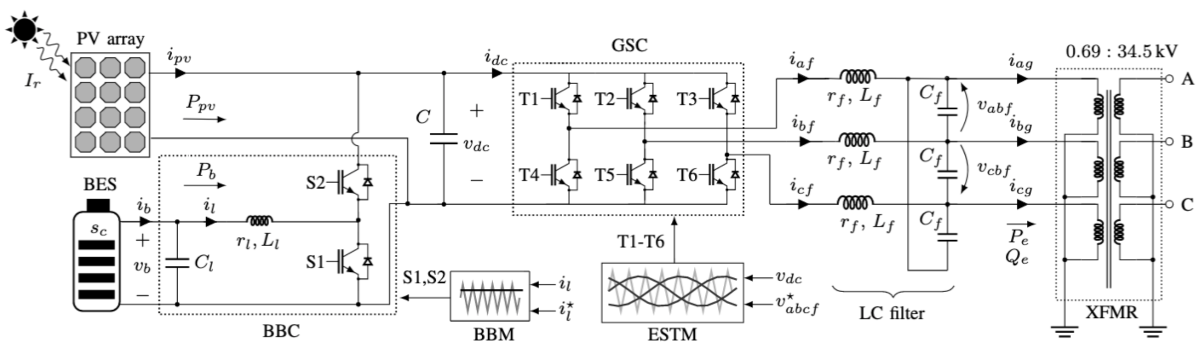

Figure 2.11 EMT model of hybrid PV plant

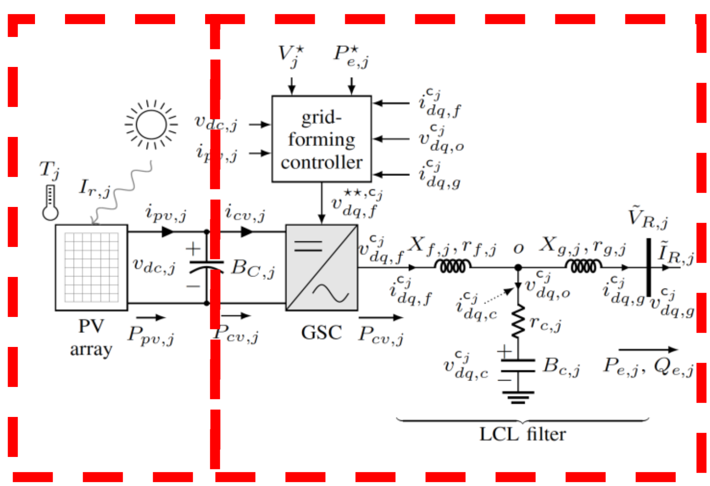

Figure 2.12 Positive sequence model of hybrid PV plant

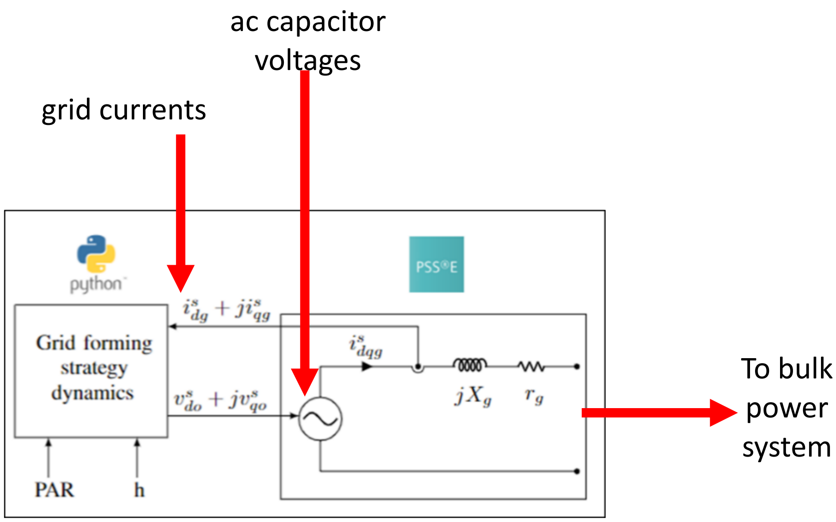

Figure 2.13 PSSE to python interface for custom developed positive sequence model

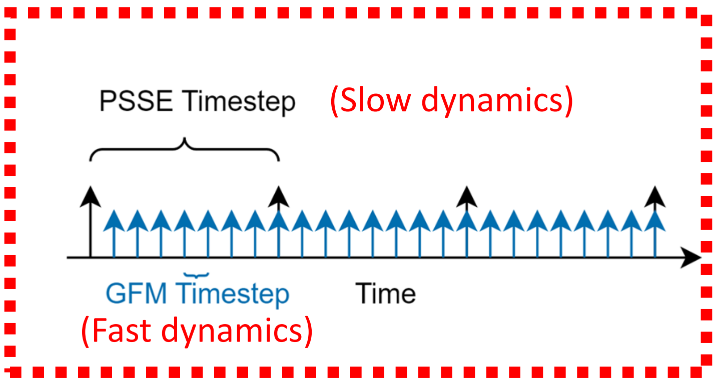

Figure 2.14 Comparison of dynamics of GFM inverter and the rest of network

3. Metrics for FIDVR Monitoring

This section introduces the metrics to detect and measure the occurrence of Fault-Induced Delayed Voltage Recovery (FIDVR) at the early onset. We also discuss the metrics to characterize and quantify the FIDVR and its use in the detection of mitigation of delayed voltage recovery.

To characterize the performance of the voltage response, WECC has provided guidelines to analyze the voltage performance following a fault. However, the criterion is a pass/fail criterion and does not give any means to quantify the deviation from a normal voltage recovery waveform.

In the literature, there are generally two methods used to quantify voltage recovery in FIDVR events [33]:

- Slope-based methods are based on the slope or derivative of the voltage after fault clearance. Slope-based methods have a major disadvantage as these are not suitable for discontinuous or sudden changes in the voltage.
- Integral-error-based methods measure the integral of the difference between pre-fault voltage and actual voltage after fault-clearance. However, these methods cannot distinguish between a voltage that recovers to about 0.8 pu and then takes a long time to recover to pre-fault voltage. The voltage initially recovers to a lower value, say 0.5 pu, then quickly recovers to the nominal value. An integral-error metric might quantify both voltages recovers as the same.

To deal with the limitations of the methods described in the literature, we utilize a PDF-based voltage recovery index known as the Kullback-Liebler divergence. The proposed index can differentiate the voltages that take longer to recover as described previously and also provides a critical value that demarcates a sharp boundary indicating non-compliance of voltage with a given voltage recovery criterion. The index was first proposed by the authors of [33] and is used here with some modifications.

To quantify the system's performance with different control schemes, a voltage recovery criterion is considered to compare and determine the acceptable post-fault voltage recovery with respect to time. We have used the North American Electric Reliability Corporation (NERC) voltage recovery criteria as given in [34] and shown in Figure 3.1.

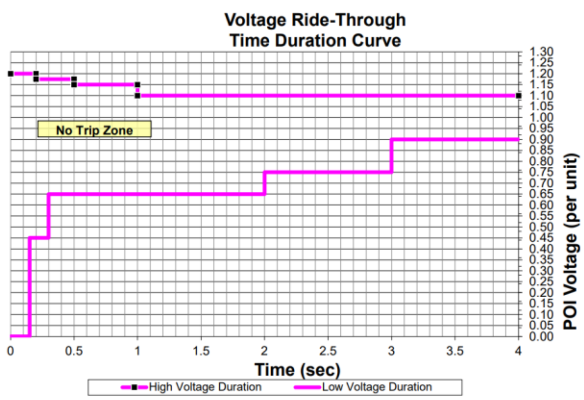

Figure 3.1 NERC voltage recovery criteria as per NERC PRC-024-2 [34]

3.1 Kullback-Liebler Divergence

To estimate the severity of FIDVR, we have used an entropy-based metric to compare the deviation of voltage from the transient voltage recovery criterion. This was inspired by the KL distance proposed to quantify FIDVR for planning of reactive reserves [33]. The divergence is the statistical distance between the probability distribution of the original voltage waveform and the probability distribution of the reference. A pictorial representation of the slow and fast voltage recovery with their respect probability density functions (PDFs) is shown in Figures 3.2 and 3.3. This specific probability density function is for the time after the fault (1.1 sec) to the end (5 sec). We use the idea in smaller time-windows to get a real-time implementation.

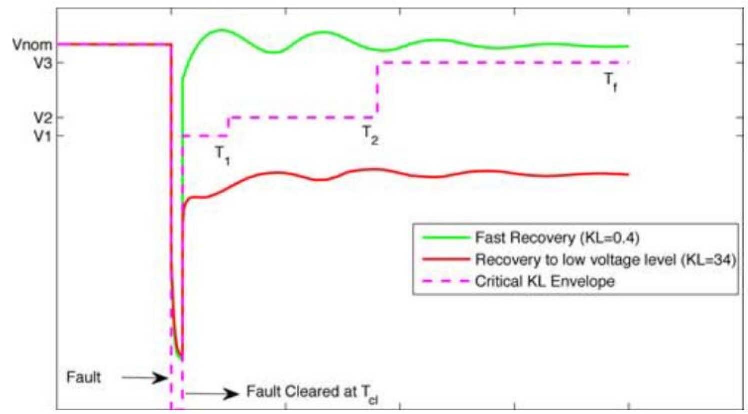

Figure 3.2 Slow and fast recovery of voltage post-fault [33]

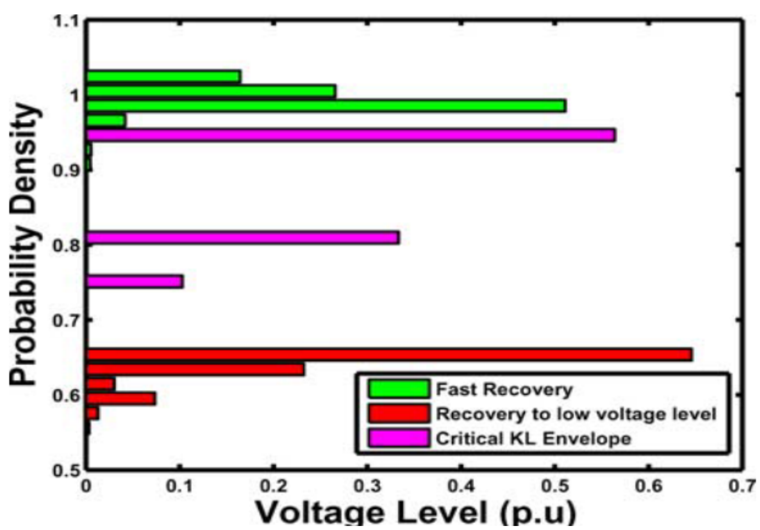

Figure 3.3 Discrete PDF of voltages in figure 3.2

The KL divergence measures the relative entropy between two probability density functions (PDFs). Borrowing the term from information theory, we call this relative distance the Kullback-Liebler (KL) divergence. We can define the KL divergence for the given PDF of a voltage waveform $p(x)$.

To calculate the KL divergence, the Probability Density Function (PDF) of the voltage waveform is computed and compared with the PDF of an ideal voltage recovery.

Since KL divergence is a relative entropy between two PDFs, we first define the entropy of a function, denoted by $H(p,T)$, with probability density function $p(x)$ as:

$$H(p,T) = -\int_{x} p(x) \ln p(x)\, dx \qquad (3.1)$$

The actual PDF $p(x)$ can be approximated by discretized PDF $\tilde{p}(n)$ over N discrete intervals, thus entropy $H(.)$ becomes:

$$H(\tilde{p},T) = -\sum_{i=1}^{N} \tilde{p} \ln (\tilde{p}) \qquad (3.2)$$

The Kullback-Liebler divergence between two PDFs, $p(x)\ and\ q(x)$, denoted by $D(p||q)$, is defined by:

$$D(p||q) = \int_{x} p(x) \ln\left(\frac{p(x)}{q(x)}\right) dx \qquad (3.3)$$

The KL divergence is a scalar value that is always non-negative and is zero only when both PDFs are equal. KL divergence gives a measure of relative entropy (or relative distance) between two PDFs. So, we will utilize this property of KL divergence to measure the voltage recovery when compared to an ideal or required voltage recovery. The value of KL divergence will increase when the difference between two PDFs is greater.

The absolute value of KL divergence can give a quantitative measure of the difference between the PDFs of voltages, but we are interested in comparing the voltage recovery performance against a voltage recovery criterion, i.e., the NERC voltage recovery criterion (V_{WECC}). To accomplish this, we define a critical value of KL divergence below which the voltage satisfies V_{WECC}. We divide the voltage recovery criterion according to different timeframes and voltage constraints.

The voltage satisfies the following condition for the time instants, T_1 and T_2, such that $T_{cl} < T_1 < T_2 < T_f$:

$$\boldsymbol{\mathcal{E}} \coloneqq \begin{cases} \boldsymbol{v(t) \geq V_1}; & \boldsymbol{T_{cl} \leq t < T_1} \\ \boldsymbol{v(t) \geq V_2}; & \boldsymbol{T_1 \leq t < T_2, V_2 > V_1} \\ \boldsymbol{v(t) \geq V_3}; & \boldsymbol{T_2 \leq t \leq T_f, V_3 > V_2} \end{cases} \qquad (3.4)$$

where $\Delta T_1 \coloneqq T_1 - T_{cl}$, $\Delta T_2 \coloneqq T_2 - T_{cl}$, $\Delta T_f \coloneqq T_f - T_{cl}$ and

$\boldsymbol{\mathcal{E}}$	Voltage envelope set of WECC voltage recovery criterion
$\boldsymbol{T_{cl}}$	Fault clearing time
$\boldsymbol{T_1}$	Time till the first voltage constraint
$\boldsymbol{T_2}$	Time till the second voltage constraint
$\boldsymbol{T_f}$	Final simulation time
$\boldsymbol{V_i}$	$\boldsymbol{i^{th}}$ voltage constraint, $\forall\ \boldsymbol{i = 1, 2, 3}$

The critical value of KL divergence, $\boldsymbol{\mathcal{K}}^*$, that shows compliance with the transient voltage recovery criterion is calculated using:

$$\begin{aligned}\mathcal{K}^* := &\frac{1}{\Delta T_f}\left(\Delta T_1 \log \Delta T_1 + (\Delta T_2 - \Delta T_1)\log(\Delta T_2 - \Delta T_1)\right)\\ &+ \frac{1}{\Delta T_f}(\Delta T_f - \Delta T_2)\log(\Delta T_f - \Delta T_2)\\ &+ \log Z - \log \Delta T_f\\ &+ \frac{\lambda}{\Delta T_f}\left(\Delta T_1(1-V_1)^2 + (\Delta T_2 - \Delta T_1)(1-V_2)^2\right)\\ &+ \frac{\lambda}{\Delta T_f}(\Delta T_f - \Delta T_2)(1-V_3)^2.\end{aligned} \tag{3.5}$$

If a post-fault voltage trajectory, $v(t)$, satisfies the given condition defined by envelope ϵ, then $\mathcal{K} \leq \mathcal{K}^*$ where

$\boldsymbol{\mathcal{K}}$	KL divergence between discrete PDFs
$\boldsymbol{\mathcal{K}}^*$	The critical value of KL divergence

Note that the value of $\mathcal{K}^*$ depends on $T_{cl}, T_1, T_2, T_f,\ and\ V_i$. For using specific values of voltages and times for V_{WECC} and $T_f = 20\ s$, the critical value of KL divergence is 9.75. This means that any voltage trajectory that follows the V_{WECC} will have a $\mathcal{K}$ of less than 9.75. Also, the critical value of KL divergence can change when the parameters of calculation change or the transient voltage recovery criterion changes.

3.2 Impact of Operating Conditions on Severity of FIDVR

The higher the IM percent, the longer they take to recover to their pre-fault voltage. Also, the response with the least amount of IM has the most negative KL, while the response with the largest amount of IM is the least Negative and goes positive for a small amount of time. The slope of the KL index can be used to estimate the time required for the FIDVR to recover; this cannot be done directly on the voltages due to the oscillations. However, there are sharp transitions in the KL index due to the logarithm function, and this needs to be improved as well for predictive capabilities.

As the system loading or the ratio of the SPIM in the load changes, the delayed voltage recovery characteristics of the system also change. This phenomenon is shown in Figure 3.4.

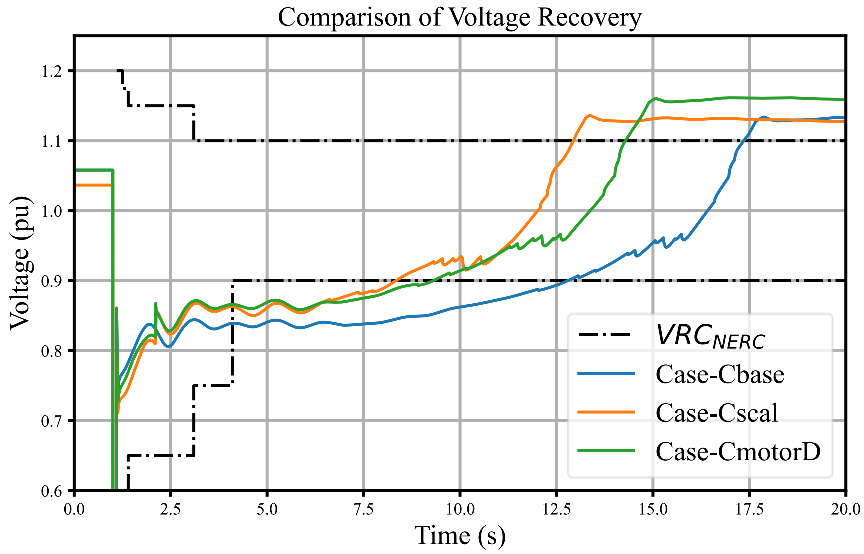

Figure 3.4 Severity of FIDVR with base case, load scaling and motor-D ratio change

4. Impact of IBR Controls on Voltage Stability

In this section, we give details of the impact of inverter-based resources on short-term voltage stability. We consider the phenomenon of delayed voltage recovery and show different control modes of IBRs can impact delayed voltage recovery. If not properly mitigated, the delayed voltage recovery can extend to a sudden voltage collapse.

We have developed a case study to study the impact of high penetration of utility-scale PV generation in the transmission system. More specifically, the objective is to develop a dynamic voltage support control to improve fault-induced delayed voltage recovery (FIDVR) and compare different mitigation techniques to import the system's short-term voltage stability by improving voltage recovery after a fault.

The system developed by the IEEE PES Power System Dynamic Performance Committee is used for testing different control modes [35]. The standard Nordic 74-bus system for voltage stability is modified by replacing some of the synchronous generators with hybrid PV plants, and the system performance is assessed with increased penetration of solar PV plants.

We replaced some of the synchronous generators with hybrid-PV plants as follows: g6 and g7are replaced with 5 hybrid PV plants (130 MVA each) connected to buses 1041 to 1045; g14 replaced 3 hybrid PV plants (240 MVA each) connected to buses 4042, 4043 and 4046; and g17 is replaced with 2 hybrid PV plants connected to bus 4061 and 4062. Some of the connected shunts are adjusted to make the system operate like the one described as operating point-B in [35]. The system diagram after replacing synchronous generators with hybrid PV plants is shown in Figure 4.1.

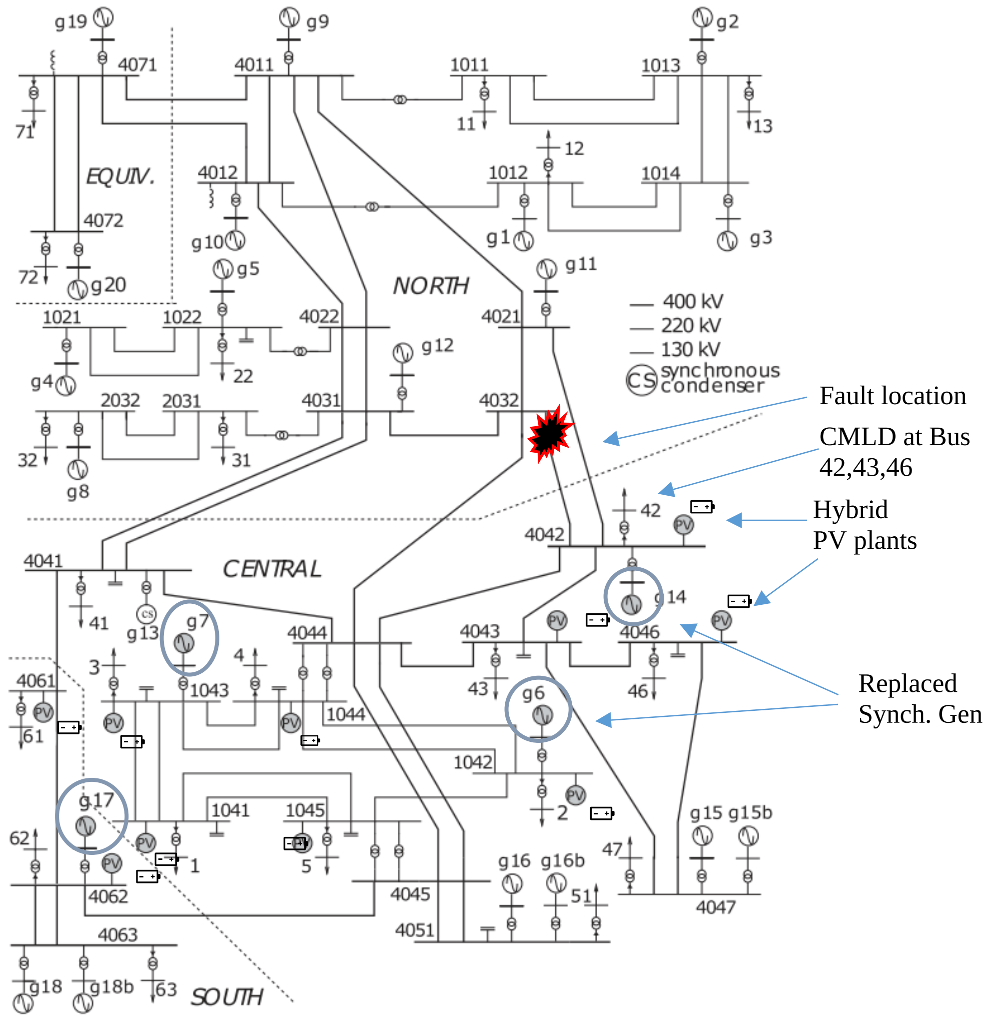

Figure 4.1: Modified Nordic voltage stability test system

To capture the Fault Induced Delayed Voltage Recovery (FIDVR) phenomenon, the load has been modeled as a composite load model to include the dynamics of single-phase induction motors, which are the primary cause of FIDVR due to stalling when the voltage drops due to a fault. The topology of a typical composite load model (CMLD) is given in Section 2.3. In this study, we have not included aggregated distributed generation with the composite load model, so only the CMLD (and not CMLDWG) model is used.

In the Nordic voltage stability test system, several loads in the system have been modeled as composite loads. For this case study, buses 42, 43, and 46 have been taken as composite load buses.

To quantify the performance of the system with different control schemes, a voltage recovery criterion is considered to compare and determine the acceptable post-fault voltage recovery with respect to time, as given in Section 3. The model of hybrid PV plants used is shown and discussed in Section 2.5.

4.1 Comparison of different control models of hybrid PV plants

As described in the previous section, time-domain simulations for the system are carried out to measure the impact of dynamic voltage support on the FIDVR.

The impact of different control parameters and control strategies is tested on the system for specific faults in the system. A 3-phase fault is considered on lines 4032-4044 close to bus 4032. The fault is applied for 100 ms and cleared by opening the line between bus 4032-4044. This fault location is selected because it influences the hybrid PV systems and causes the motor to stall on the nearby loads; thus, the FIDVR phenomenon is observed.

4.1.1 Hybrid PV Plant with Const. P&Q

In this case, we consider composite loads on Bus 42,43,46 in the Central area of the Nordic voltage stability test system. The BESS and PV plants are operated while fulfilling LVRT requirements, but no dynamic voltage and reactive power injection support are provided by any of the inverters in hybrid PV plants.

The results indicate significantly delayed voltage recovery in this case because of single-phase induction motor stalling in the buses close to the fault location. When compared to the NERC voltage recovery criterion, not only the buses close to the fault (Bus 42) show FIDVR but also neighbor buses that are not equipped with the CMLD model.

Also, since the hybrid PV plants operate in constant real and reactive power mode, for which setpoints are fixed from load flow during initialization, no extra reactive power support is provided by the PV plant to recover the voltage. The voltage profiles at the composite load buses and neighbor buses are shown in Figures 4.2-4.3

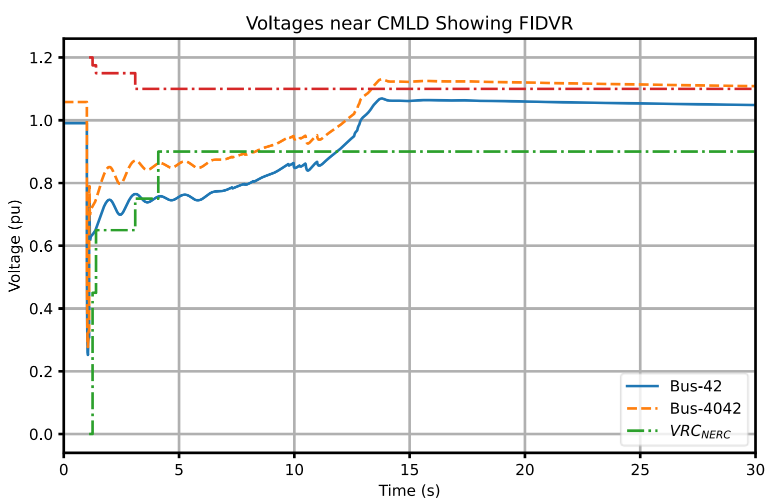

Figure 4.2 Voltage profile at the buses showing FIDVR

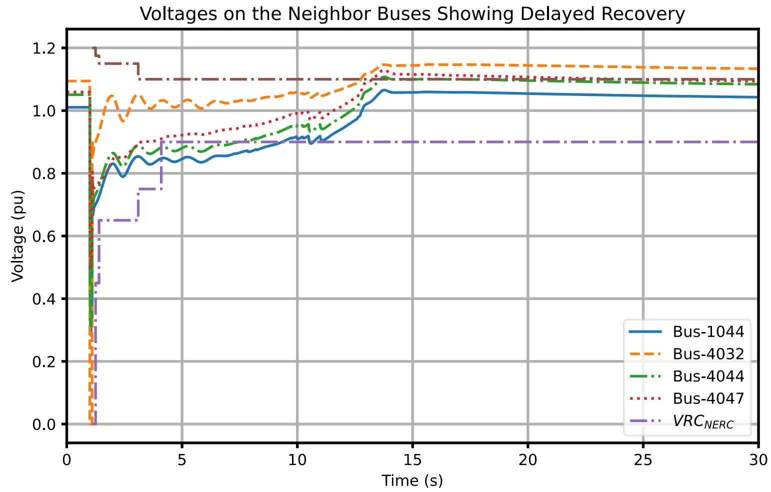

Figure 4.3 Voltage at the neighbor buses

4.1.2 Voltage Control Mode

In this case, both BESS and PV plant inverters have been included with a controller to control terminal voltage at the Point of Interconnection (POI). So, reactive power is injected at the POI proportional to the voltage deviation from the nominal voltage after the fault is cleared. Due to extra reactive power support from the hybrid PV plant, the voltage at the POI shows a significantly better recovery rate compared to the base case. The voltage profiles for this case are shown in Figures 4.4-4.5.

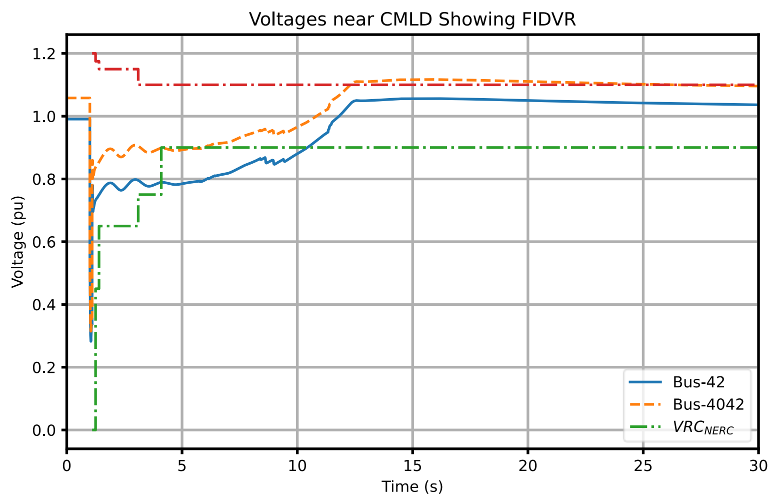

Figure 4.4 Voltage profile at the buses showing FIDVR

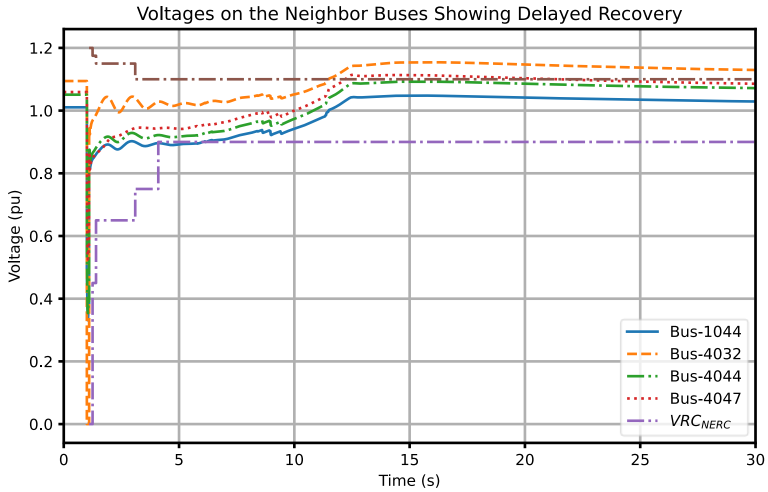

Figure 4.5 Voltage at the neighbor buses

4.1.3 Motor-D Tripping – 20%

As seen in previous cases, the reactive power injection capability of the hybrid PV plants is not fully utilized unless we optimally set the real and reactive power set points of the system.

When a single-phase induction motor (usually installed in residential AC units) stalls, it doesn't restart automatically. So, the motor is tripped by the thermal relays, which take some time in order of a few seconds to tens of seconds. Old motors are usually equipped with thermal relays but not Undervoltage (U/V) relays.

But the newer AC units are also equipped with U/V protection, which can trip the motor in a few cycles when low voltage is detected at the terminals.

In the next study, we assume that 20% of the single-phase motors (AC units) are equipped with U/V protection, which trips the motor almost immediately (within a few cycles) after the fault and thus prevents the loads from demanding huge amounts of reactive power. So, tripping of induction motors helps in voltage recovery, as evident in the results shown in Figures 4.6-4.7.

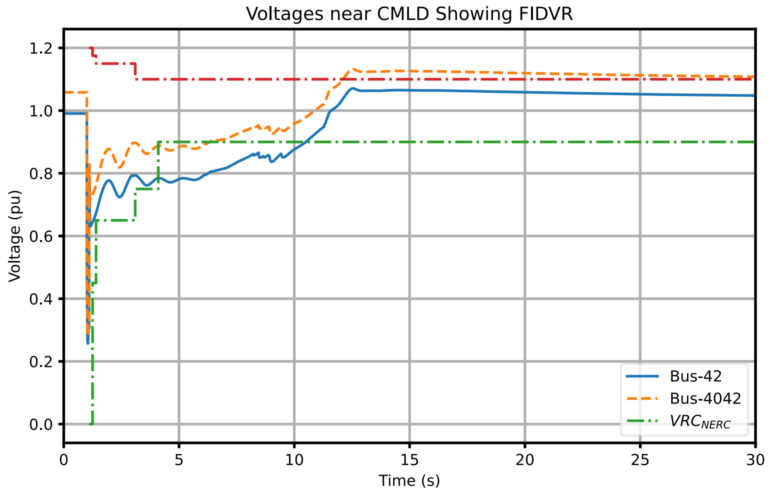

Figure 4.6 Voltage profile at the buses showing FIDVR

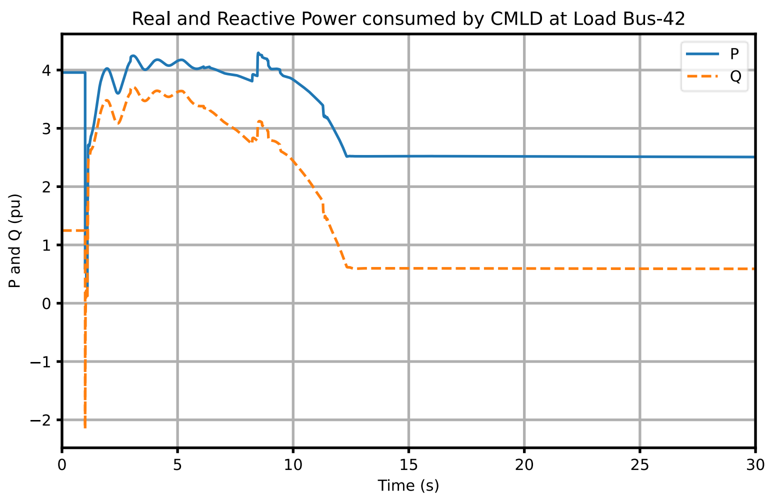

Figure 4.7: Real and reactive power demand by composite load

4.1.4 Entropy-based measurement of severity of FIDVR

As described in the previous section, time-domain simulations on the Nordic voltage stability test system are carried out to measure the impact of dynamic voltage support on the FIDVR.

The impact of different control parameters and control strategies is tested on the system for specific faults in the system. A 3-phase fault is considered on lines 4032-4044 close to bus 4032. The fault is applied for 100 ms and cleared by opening the line between bus 4032-4044. This fault location is selected because it influences the hybrid PV systems and causes the motor to stall on the nearby loads; thus, the FIDVR phenomenon is observed.

Table 4.1 Case study scenarios with different controls

Case	Description
Case-A	Const. real and reactive power injection
Case-B	REPCA voltage control and Inverter-level Q/V control
Case-C	Inverter-level coordinate Q/V control (No plant-level controller involved)
Case-D	Case-C + 25% Motor-D tripping for all CMLD loads

Table 4.1 gives the description of different control cases for the hybrid PV plants. Table 4.2 gives numerical values of the voltage recovery indices for all the case studies. The entropy value of a better voltage recovery case is less, so from Case-A to Case-D, the voltage recovery becomes better, as evident from Fig. 4.8, and 4.9. For more details, interested readers can refer to our paper [42].

Also, for KL divergence, the value decreases, and for Case-D, the value is less than 9.75, i.e., the critical value of KL divergence; this shows that the last case complies with the NERC voltage recovery criterion.

Table 4.2 Voltage recovery characterization indices for all case studies

Case	Entropy	KL Divergence
Case-A	1.1196	25.3434
Case-B	1.0641	19.4609
Case-C	0.9108	13.7850
Case-D	**0.8149**	**9.5197**

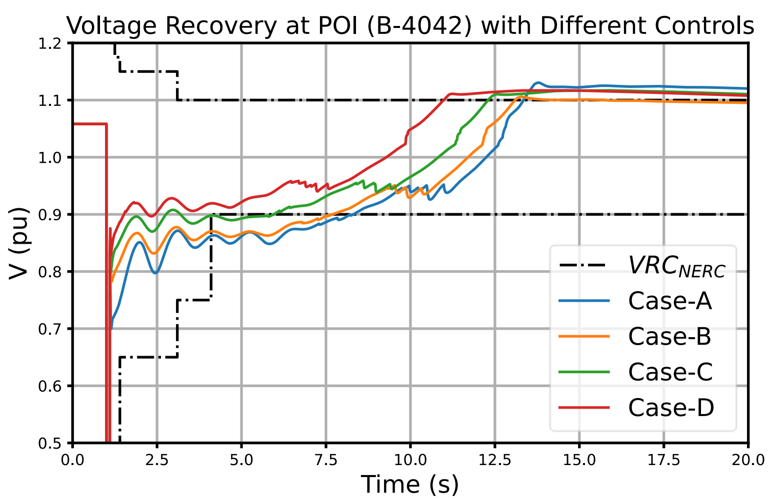

Figure 4.8 Voltage profile comparison for all control cases [42]

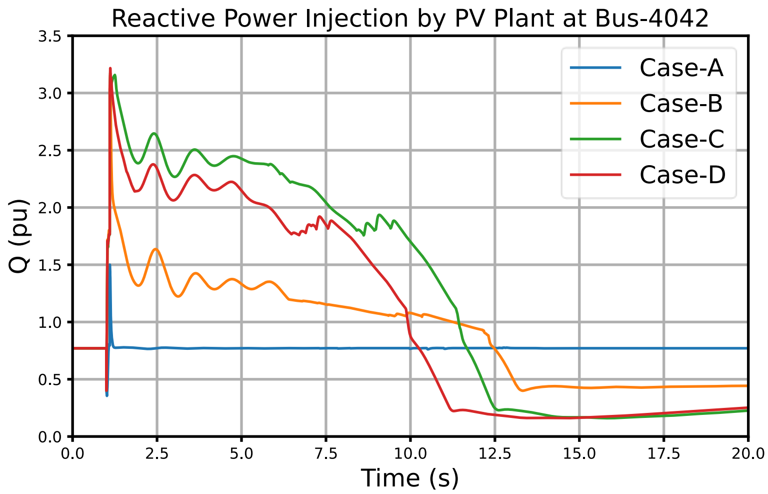

Figure 4.9 Reactive power injection by PV plant for different controls [42]

5. Data-driven control strategies using hybrid PV plants

In this task, we are developing data-driven online control strategies for DERs and hybrid PV plants to mitigate voltage instability. During the last two quarters, we have been investigating the impact of utility-scale solar PV power plants with Battery Energy Storage System (BESS), hereby referred to as hybrid PV plant, on the short-term voltage stability of the system. We developed a case study to study the impact of high penetration of utility-scale PV generation in the transmission system. More specifically, the objective was to develop a dynamic voltage support control to improve fault-induced delayed voltage recovery (FIDVR) and compare different mitigation techniques to import the system's short-term voltage stability by improving voltage recovery after a fault. The details are given in the previous report.

We worked on a Deep Reinforcement Learning (DRL) based data-driven load control by optimally tripping stalled induction motor loads to recover the voltage quickly in a FIDVR event. The amount of load tripping depends on system operating conditions, so the data-driven framework gives optimal load control adaptable to the system conditions. The results from numerical simulations show that the dynamic reactive power injection and DRL-based load control improve the voltage recovery and significantly decrease the amount of load tripped.

First proposed in [33], entropy-based metrics were used to quantify delayed voltage recovery. The KL divergence measures the relative entropy between two probability density functions (PDFs).

To calculate the KL divergence, the voltage waveform's Probability Density Function (PDF) is computed and compared with the PDF of an ideal voltage recovery. The Kullback-Liebler divergence between two PDFs, $p(x)\ and\ q(x)$, denoted by $D(p||q)$, is defined by:

$$D(p||q) = \int_x p(x) \ln\left(\frac{p(x)}{q(x)}\right) dx \qquad (5.1)$$

During FIDVR events, some load is tripped in a controlled manner to constrain the impact of delayed voltage recovery. Usually, it is done using under-voltage load shedding (UVLS) relays, which cannot adapt to the changing operating conditions and varying output by renewable energy resources. So, the optimal amount of load tripping is dependent on several factors, including but not limited to system loading conditions, location of the fault, percentage of motor-D in composite load, etc.

5.1 Reinforcement Learning for Power System

To optimally find out the amount of load to be tripped, the problem can be formulated as a dynamic programming problem. Due to the high dimensions of states in a power system, dynamic programming is computationally expensive to solve. So, a data-driven approach in which the system model is not needed can be used. The data-driven agent can be trained in offline simulation and then can operate and control the system in an online manner.

For large-scale power systems, the emergency control problem is a highly non-linear, non-convex optimal decision-making problem and can be formulated as follows:

5.1.1 Objective function:

$$min \int_{T_o}^{T_c} C(x_t, y_t, a_t)dt$$

Constraints:

$$\begin{aligned}
\dot{x}_t &= f(x_t, y_t, d_t, a_t) \\
0 &= f(x_t, y_t, d_t, a_t) \\
x_t^{min} &\leq x_t \leq x_t^{max}, \forall t \in [T_0, T_c] \\
y_t^{min} &\leq y_t \leq y_t^{max}, \forall t \in [T_0, T_c] \\
a_t^{min} &\leq a_t \leq a_t^{max}, \forall t \in [T_0, T_c]
\end{aligned} \tag{5.2}$$

Here $C(.)$ represents cost function, $d(t)$ represents any disturbances, x_t is a vector of dynamic state variables (rotor angles and speed, etc.), y_t is a vector of algebraic state variables (e.g., voltages at the buses), at are the control actions (reference change or load tripping, etc.), $[T_0, T_c]$ is the time horizon. The control problem given in the objective function can be formulated as a Markov Decision Process (MDP) and solved by Reinforcing Learning (RL) methods. Not all system states are observable, so this is a partially observable MDP problem.

5.1.2 Markov Decision Process

In RL, the agent learns to make optimal decisions by interacting with the environment through exploration and exploitation [36], as shown in Figure 5.1. The environment is modeled as a (partially observable) Markov decision process (MDP), defined by:

- A state space S that could be continuous or discrete.
- an action space A that could be continuous or discrete;
- an environment transition function P: S × A → S;
- a reward function $R: S \times A \rightarrow R$;
- a discount factor $\gamma \in [0, 1]$.

In this setting, at each time step t, the agent can observe the state $s_t \in S$ and receive reward signals $r_t \in R$ from the environment. At the same time, the agent can select an action at time t, $a \in A$ to change the environment. The goal is to apply the optimal action given the current state so that the agent can accumulate the most rewards over time, which are generally defined as discounted future return R_t.

$$R_t = \sum_{t'=t}^{T} \gamma^{t'-t} r_{t'} \tag{5.3}$$

where T means the time step when the interaction with the system ends.

To evaluate the result of the action based on the current state, the action-value function, also known as the Q function, is proposed as $Q(s, a)$. We define the optimal Q-value of the state-action pair (s, a) as $Q^*(s, a)$, which represents the maximum discounted future return after taking action at states. The Q function is updated by the iteration algorithm in the Bellman equation, defined by [36].

$$Q_{t+1}(s,a) = \mathbb{E}\left[r + \gamma max_{a'} Q_t(s',a')|(s,a)\right] \tag{5.4}$$

The iteration will converge to the optimal solution $Q^*(s, a)$ as $t \to \infty$ if the state signals have the Markov property. Q-Learning is a value-based RL algorithm that finds the optimal action-selection policy using:

$$\begin{aligned} Q(s_t, a_t) \leftarrow & Q(s_t, a_t) + \eta\, [r_{t+1} \\ & + \gamma max_{a'} Q_t(s_{t+1}, a) - Q(s_t, a_t) \end{aligned} \tag{5.5}$$

where η represents the learning rate.

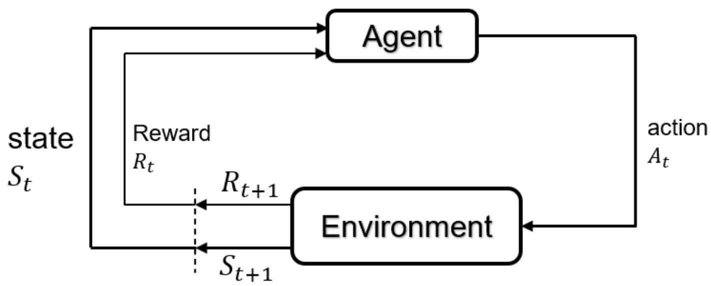

Figure 5.1: Reinforcement Learning at a Glance

5.1.3 Deep RL for Power System

For the power system environment, the system states are given by the solution from the differential and algebraic equations at each time step. For the load control problem, the system inputs are the voltages at the specified buses, which are continuous, and control actions are the percentage of load to be tripped at $t = 2.1$ sec (1 second after the fault clearance time), so the control action is also continuous. The overall framework of the deep reinforcement learning framework for the power system is shown in Figure 5.2 [41].

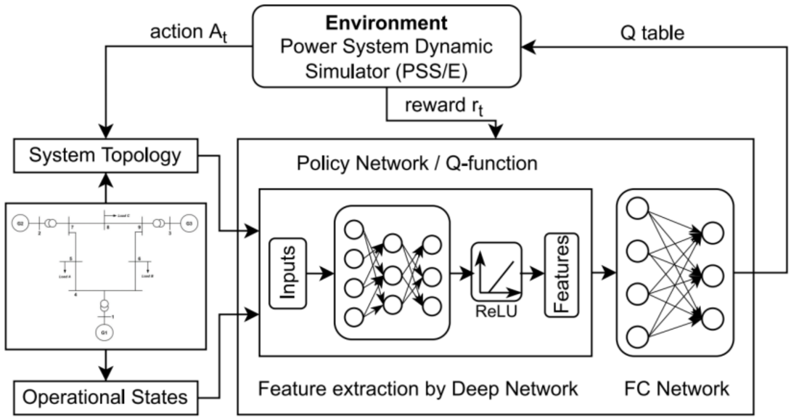

Figure 5.2. Deep Reinforcement Learning (DRL) framework for power system [41]

The Q-learning algorithms can only be applied to environments with discrete observation and action spaces. So, we used the continuous-space variant of Deep Q Networks (DQN), which is known as Deep Deterministic Policy Gradient (DDPG), first proposed in reference [36]. The algorithm for DDPG is shown in Figure 5.3.

Algorithm 1 DDPG algorithm

Randomly initialize critic network $Q(s, a|\theta^Q)$ and actor $\mu(s|\theta^\mu)$ with weights θ^Q and θ^μ.
Initialize target network Q' and μ' with weights $\theta^{Q'} \leftarrow \theta^Q$, $\theta^{\mu'} \leftarrow \theta^\mu$
Initialize replay buffer R
for episode = 1, M **do**
  Initialize a random process $\mathcal{N}$ for action exploration
  Receive initial observation state s_1
  for t = 1, T **do**
    Select action $a_t = \mu(s_t|\theta^\mu) + \mathcal{N}_t$ according to the current policy and exploration noise
    Execute action a_t and observe reward r_t and observe new state s_{t+1}
    Store transition (s_t, a_t, r_t, s_{t+1}) in R
    Sample a random minibatch of N transitions (s_i, a_i, r_i, s_{i+1}) from R
    Set $y_i = r_i + \gamma Q'(s_{i+1}, \mu'(s_{i+1}|\theta^{\mu'})|\theta^{Q'})$
    Update critic by minimizing the loss: $L = \frac{1}{N}\sum_i (y_i - Q(s_i, a_i|\theta^Q))^2$
    Update the actor policy using the sampled policy gradient:

$$\nabla_{\theta^\mu} J \approx \frac{1}{N}\sum_i \nabla_a Q(s, a|\theta^Q)|_{s=s_i, a=\mu(s_i)} \nabla_{\theta^\mu}\mu(s|\theta^\mu)|_{s_i}$$

    Update the target networks:

$$\theta^{Q'} \leftarrow \tau\theta^Q + (1-\tau)\theta^{Q'}$$

$$\theta^{\mu'} \leftarrow \tau\theta^\mu + (1-\tau)\theta^{\mu'}$$

  end for
end for

Figure 5.3: Deep Deterministic Policy Gradient (DDPG) algorithm [36]

To build the DRL framework for the power system for voltage stability studies, PSSE python API [37] is used as an environment to simulate the power system. OpenAI gym [38] is used to integrate the power system environment as a valid environment for reinforcement learning training. The algorithm for Deep RL is implemented using StableBaselines3 [39]. The complete workflow of the framework is shown in Figure 5.4.

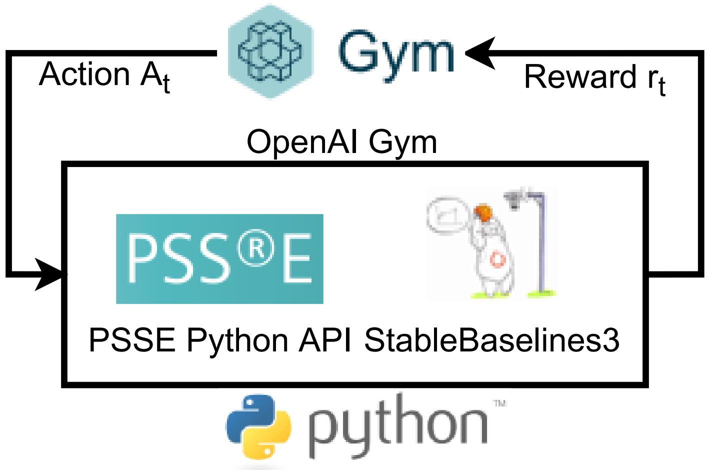

Figure 5.4 Framework of Deep RL studies using PSS/E, OpenAI Gym, and StableBaselines3

5.1.4 DRL Reward Function to Mitigate FIDVR

To evaluate the quality of action taken at each time instant, a reward function is designed considering the physical parameters and transient voltage recovery criterion by NERC.

The reward function is given by:

$$r_t = \begin{cases} -1000 & \text{if } V_i(t) \leq 0.9 \\ & \text{for } t \geq T_{cl} + 4 \\ c_1 \sum_i \triangle V_i(t) - c_2 \sum_j \triangle P_j(pu), & \text{otherwise} \end{cases}$$

$$\triangle V_i(t) = \begin{cases} \min\{V_i(t) - 0.45, 0\}, & T_{cl} \leq t \leq T_{cl} + 0.15 \\ \min\{V_i(t) - 0.65, 0\}, & T_{cl} + 0.15 \leq t \leq T_{cl} + 0.3 \\ \min\{V_i(t) - 0.75, 0\}, & T_{cl} + 0.3 \leq t \leq T_{cl} + 0.2 \\ \min\{V_i(t) - 0.90, 0\}, & T_{cl} + 3 \leq t \end{cases} \tag{5.6}$$

where T_{cl} is the fault clearing time instant.

The reward function has two parts: 1) total bus voltage deviation below the lower voltage envelope given by transient voltage recovery criterion. 2) total load shedding amount, where $\triangle P_j(pu)$ is the amount of load tripped in per unit at bus j at the time step t. c_1 and c_2 are weight factors for the two components of reward and are tuned heuristically combined with the prior knowledge of the environment.

5.2 Case Study

The developed deep reinforcement learning framework is used for optimal undervoltage load shedding to mitigate FIDVR. The DDPG algorithm is tested on the modified Nordic voltage stability system with select locations for grid-forming inverters, is shown in Figure 5.5. The OpenAI Baselines3 tool is used with PSS/E python API to learn a closed-loop control policy based on DDPG. The objective is to determine the amount of Motor-D load tripping at buses 42, 43, and 46, which are modeled as composite loads and thus cause delayed voltage recovery after fault clearance. The inputs to the algorithm are the voltage magnitudes at the high voltage side of the transformer connected to composite load buses. The coefficients for the reward function are taken as $c_1 = 260$ and $c_2 = 150$.

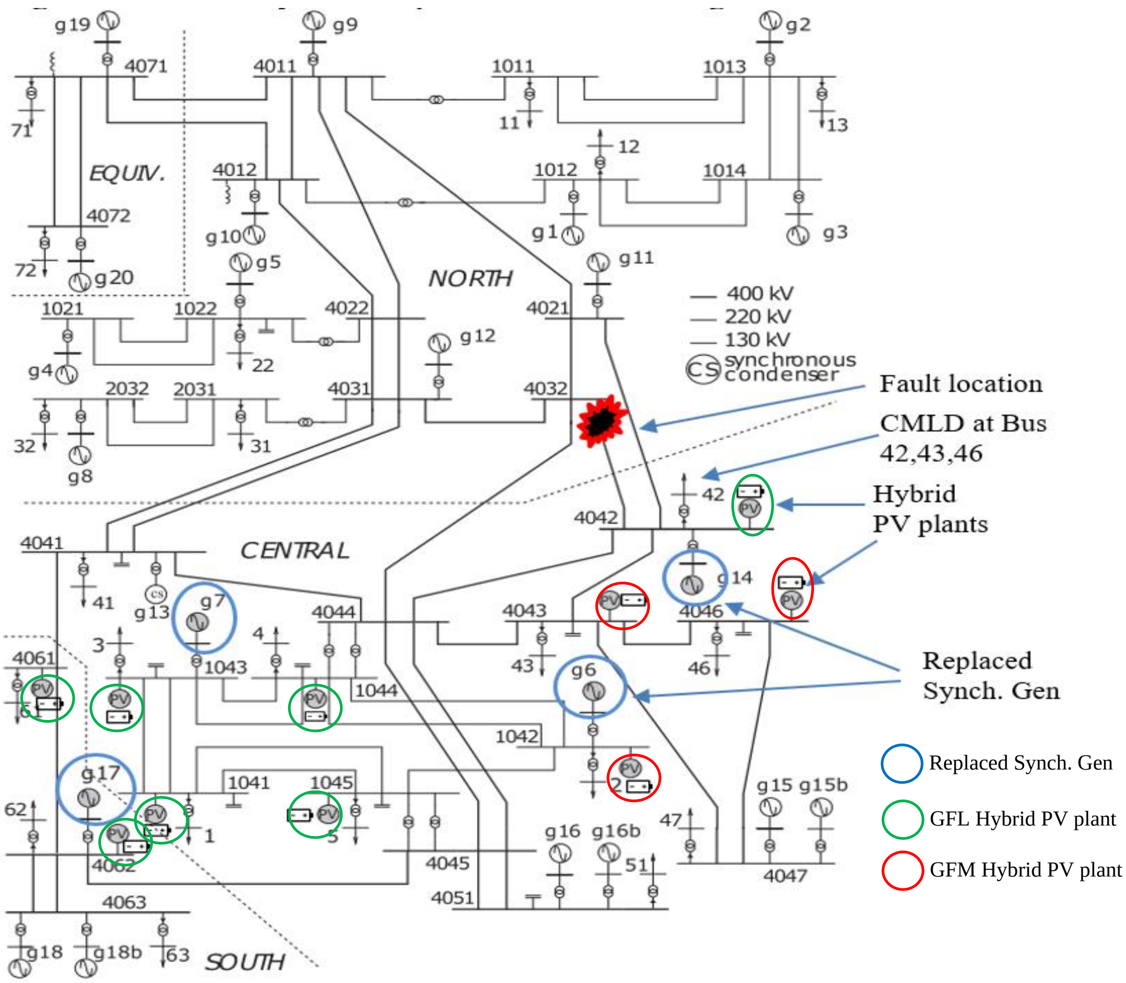

Figure 5.5 Modified Nordic voltage stability test system showing the location of GFL & GFM inverters in the system [35]

The control action is applied 1 second after the fault-clearing time ($T_{cl} = 1.1s$) to account for the communication, sensing, and computation delays. The maximum percentage of Motor-D loads that can be tripped is 60% of the initial Motor-D load. Other important hyperparameters are as follows: total interaction steps in training are 50,000; nodes in hidden layers Nh1 = Nh2 = 256; learning rate η = 0.00005; minimum exploration rate ϵmin = 0.02. Also, the learning starts at the 300th time step to give enough time to the DRL agent to explore the environment. During offline training, each episode begins flat for 1 second. A fault is applied at 1 second, lasting for 100 ms. The DRL agent takes observation and applies actions to the environment at 0.1 s time steps. Note that the DRL time step is different from the environment simulation time step, which is set to $\frac{1}{120}$s.

The model of hybrid PV plants used is shown and discussed in Section 2.5.

5.2.1 Case Study Results

The impact of different control parameters and control strategies is tested on the system for specific faults. A 3-phase fault is considered on lines 4032-4044 close to bus 4032. The fault is applied for 100 ms and cleared by opening the line between bus 4032-4044. This fault location is selected because it influences the hybrid PV systems and causes the motor to stall on the nearby loads; thus, the FIDVR phenomenon is observed. Table 5.1 describes different control cases for the hybrid PV plants.

Table 5.1 Case study scenarios with different controls using GFL & GFM inverters

Case	Description
Case-A	Const. real and reactive power injection (GFL Inverters)
Case-B	REPCA voltage control and Inverter-level Q/V control (GFL Inverters)
Case-C	Inverter-level coordinated reactive power/voltage (Q/V) Control Loop (GFL Inverters)
Case-D	Case-C + Load Control + DERs
Case-E	Grid Forming Inverters + Load Control + DERs

5.2.2 Optimal Load Tripping with Deep Reinforcement Learning

To comply with the voltage recovery criterion at all the buses, 50% of all motor-D loads need to be tripped. However, this load trip doesn't consider the sensitivity of the load trip to the voltage magnitude at each bus. Thus, the amount of load trip may be an over-design for the system.

Since the amount of load percentage needed to trip depends on the voltage sensitivity of that bus w.r.t system operating conditions, the same amount of load trip at all the composite load is not a suitable action. So, we employ the deep reinforcement learning framework to determine the amount of optimal load tripping.

The system is simulated using the Case-C control for hybrid PV plants since it provides the best dynamic voltage support to improve delayed voltage recovery. Thus, combining Case-C inverter controls with optimal load control using DRL will produce the best results for improvement in FIDVR.

The system is simulated as per the hyperparameters given in the previous section. The reward function converges as the training proceeds, as shown in Figure 5.6. The low reward value around the 5000th time-step indicates a bad exploration by the DRL agent. The optimal control action is tested on the system, and it gives a value of 2%, 38%, and 52% load trip for Loads 42,43,46, respectively. The voltage waveforms for the load are shown in Fig. 5.7.

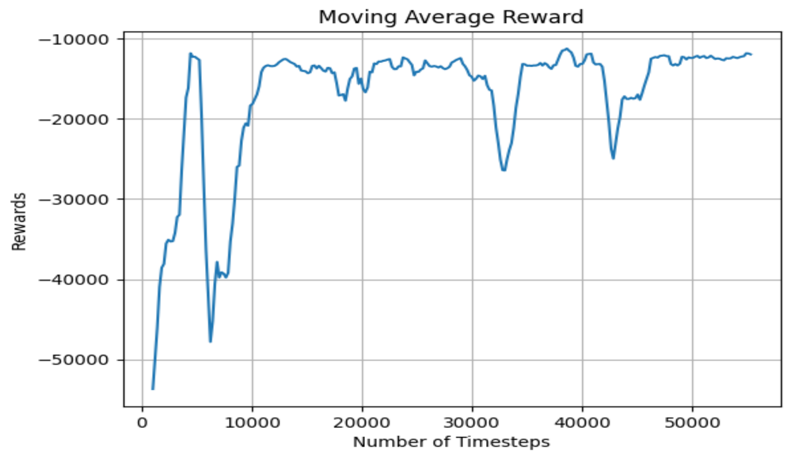

Figure 5.6: Moving average reward for the agent during training

Table 5.2 gives numerical values of the voltage recovery indices for all the case studies. The entropy value of a better voltage recovery case is less, so from Case-A to Case-D, the voltage recovery becomes better, as evident from Fig. 5.7. Also, for KL divergence, the value decreases, and for Case-D, the value is less than 9.75, i.e., the critical value of KL divergence, this shows that the last case complies with the NERC voltage recovery criterion.

Table 5.3 shows the comparison of load control for non-optimal load tripping, i.e., 50% of Motor-D tripping with the optimal tripping computed with the trained DRL agent. The optimal load tripping reduced the total amount of load tripped by about 30% compared to the non-optimal load trip. Also, as Case-D and Case-E simulate grid following vs. grid forming inverters, respectively, the results show a decrease in the amount of load while still complying with the transient voltage recovery criterion.

Table 5.2 Entropy & Kullback-Liebler Divergence values for different cases with GFL & GFM Inverters

Case	Entropy	KL Divergence
Case-A	1.1196	25.3434
Case-B	1.0641	19.4609
Case-C	0.9108	13.7850
Case-D	0.8149	9.5197
Case-E	0.8085	9.4989

Table 5.3 Comparison of the amount of load tripping with and without optimal load control

				Case-D (GFL)		Case-E (GFM)	
Bus #	**P (MW)**	**Motor-D (30%)**	**Non-Optimal tripping (MW)**	**Optimal tripping %**	**Optimal tripping (MW)**	**Optimal tripping %**	**Optimal tripping (MW)**
42	400	120	60	2	2.4	2	2.4
43	900	270	135	38	102.6	31	83.7
46	700	210	105	52	109.2	43	90.3
			300		**214.2**		**176.4**

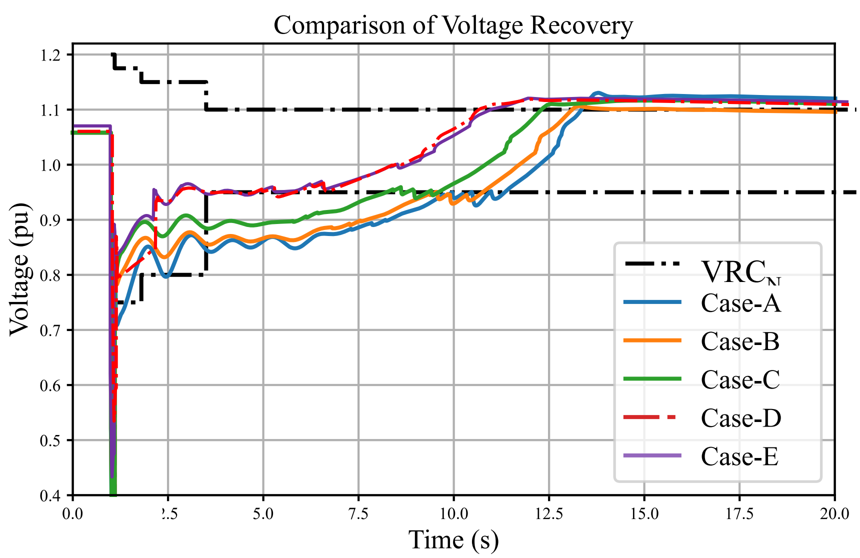

Figure 5.7 Voltage profile comparison for all control cases

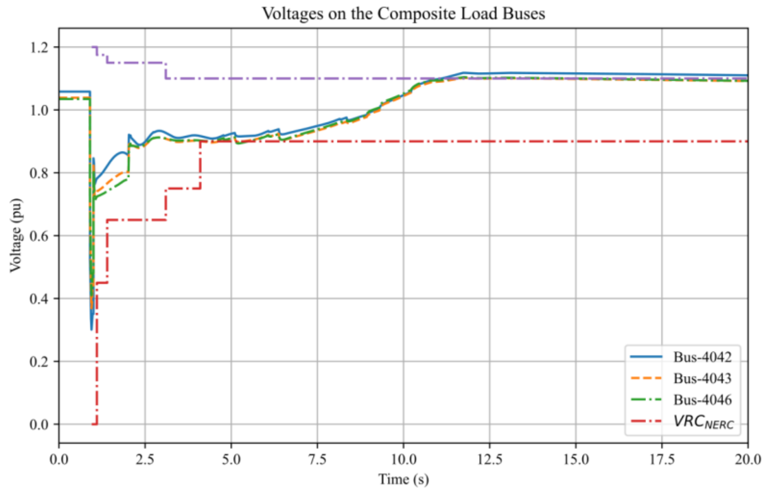

Figure 5.8 Voltage profile with optimal load tripping control

5.3 Discussion on results

The results given in the previous section give some good insights into the role of grid-forming inverters and data-driven control in mitigating delayed voltage recovery in a stressed power system with high penetration on IBRs. Based on the comparison of results for Case-D (with grid-following inverters) and Case-E (with grid-forming inverters), it is evident that grid-forming inverters mitigate the FIDVR to a greater extent compared to grid-following inverters. This is based on the difference in the inherent control structure of both types of inverters.

To comply with the transient voltage recovery criterion, grid-forming inverters decrease the amount of load needed to be tripped while reaching the same level of KL measure index as given by grid-following inverters.

The technical results underline the critical role of inverter operational principles in shaping delayed voltage recovery dynamics. While grid-forming inverters present a promising avenue, especially for grids with high inverter penetration, considerations around control strategies, integration levels, and the broader grid environment are important in ensuring voltage stability.

6. Conclusions

6.1 Summary

The rapid integration of renewable energy sources, especially photovoltaic systems, into the global energy grid necessitates innovative solutions to maintain and improve grid stability. This research has shown that data-driven controls, when combined with traditional power system methodologies, can provide effect solutions to enhance voltage stability through effective TSO-DSO interactions.

Our novel controller for hybrid PV plants has demonstrated its capability to reliably deliver the requested active/reactive power to the main grid. By leveraging physics-based, data-driven techniques, we've harnessed the full potential of IBRs, particularly storage units, for the mitigation of voltage instability. We used an entropy-based measure (KL measure) to quantify the severity of fault-induced delayed voltage recovery and used this metric to identify the most suitable and effective control mode for mitigation of FIDVR.

Moreover, we have developed a deep reinforcement learning (DRL) framework for power system control using an industry-standard power system solver. The DRL framework is tested on a modified IEEE Nordic74 voltage stability system for improvement in FIDVR. We selected a dynamic voltage support control for the hybrid PV plant in the system to provide maximum reactive power support. Hybrid PV plants have been shown to improve short-term voltage recovery performance using the selected voltage support control. Furthermore, we developed a deep reinforcement learning framework to compute the optimal amount of load tripping and dispatch set points for Hybrid PV plants to improv in FIDVR. We also investigated the role of grid-forming inverters in improving the short-term voltage response compared to grid-following inverters. Numerical simulations using the proposed framework show that adaptive load tripping, along with optimal control of grid-forming inverters, reduced the total amount of load tripped and improved the delayed voltage recovery by a significant margin when compared to grid-following inverters.

6.2 Future Work

While our research has paved a promising path toward a more resilient and efficient grid system, several avenues can be explored further:

- **Dynamic voltage control areas for IBRs:** Finding a control area around a hybrid PV (HPV) plant in which voltage during selected contingences can be influenced by dynamic Q-support from the Hybrid PV plant.
- **Identifying candidate locations for GFM inverters:** Most of the inverters in the power system are legacy inverters with grid-following control. Identifying the locations of the candidate inverters, which can be upgraded from grid-following to grid-forming control, is another future extension we are looking forward to.
- **Exploring frequency regulation with Hybrid PV plants:** With high penetration of non-synchronous generation, system inertia is diminishing rapidly, thus making the system prone to higher frequency deviations. While the current work explores the voltage support aspects of hybrid PV plants, we plan to extend the data-driven control technique to frequency and inertia regulation.

- **Integration with Other Renewable Energy Sources:** Extending our work to incorporate other renewable sources like wind and hydroelectric power could present a holistic solution for future green grids.
- **Consideration of Cybersecurity Challenges:** With an increasing reliance on data-driven and communication-based controls, future work should also factor in potential cybersecurity vulnerabilities and solutions.

The evolving landscape of power grids demands continuous research and innovation. It is hoped that this project will serve as a step towards building more resilient and sustainable energy grids for the future.

References

[1] U.S. Energy Information Administration, Annual Electric Generator Report. Accessed on Oct 25, 2022 at https://www.eia.gov/todayinenergy/detail.php?id=49756

[2] Maggie Kristian and Elizabeth Abramson, , Great Plains Institute, based on data from the MISO Generator Interconnection Queue as of January 26, 2020. https://www.betterenergy.org/blog/hybrid-resources-are-coming-to-miso-an-emerging-opportunity/.

[3] N. Hatziargyriou et al., "Definition and Classification of Power System Stability – Revisited & Extended," in IEEE Transactions on Power Systems, vol. 36, no. 4, pp. 3271-3281, July 2021, doi: 10.1109/TPWRS.2020.3041774.

[4] Midcontinent Independent System Operation (MISO), "MISO's Renewable integration impact assessment (RIIA)," February 2021, available at: https://cdn.misoenergy.org/RIIA%20Summary%20Report520051.pdf

[5] S. Sinha, P. Sharma, U. Vaidya and V. Ajjarapu, "Identifying causal interaction in power system: Information-based approach," 2017 IEEE 56th Annual Conference on Decision and Control (CDC), Melbourne, VIC, Australia, 2017, pp. 2041-2046, doi: 10.1109/CDC.2017.8263948.

[6] S. Eftekharnejad, V. Vittal, G. T. Heydt, B. Keel, and J. Loehr, "Impact of increased penetration of photovoltaic generation on power systems," IEEE Transactions on Power Systems, vol. 28, no. 2, pp. 893–901, 2013, doi: 10.1109/TPWRS.2012.2216294.

[7] A. R. R. Matavalam and V. Ajjarapu, "PMU-Based Monitoring and Mitigation of Delayed Voltage Recovery Using Admittances," IEEE Transactions on Power Systems, vol. 34, no. 6, pp. 4451–4463, Nov. 2019, doi: 10.1109/TPWRS.2019.2913742.

[8] A. A. R. Ramapuram Matavalam and V. Ajjarapu, "Sensitivity Based Thevenin Index With Systematic Inclusion of Reactive Power Limits," IEEE Transactions on Power Systems, vol. 33, no. 1, pp. 932–942, May 2017, doi: 10.1109/TPWRS.2017.2701811.

[9] Mitra and Parag, "Technical Guide on Composite Load Modeling," 2019, Accessed: Mar. 03, 2022. [Online]. Available: www.epri.com

[10] K. Kawabe, Y. Ota, A. Yokoyama, and K. Tanaka, "Novel Dynamic Voltage Support Capability of Photovoltaic Systems for Improvement of Short-Term Voltage Stability in Power Systems," IEEE Transactions on Power Systems, vol. 32, no. 3, pp. 1796–1804, May 2017, doi: 10.1109/TPWRS.2016.2592970.

[11] A. R. R. Matavalam, R. Venkatraman, and V. Ajjarapu, "Mitigating delayed voltage recovery using der & load control in distribution systems," in 2022 IEEE Power & Energy Society General Meeting (PESGM). IEEE, 2022, pp. 1–5.

[12] G. Lammert, D. Premm, L. D. P. Ospina, J. C. Boemer, M. Braun, and T. Van Cutsem, "Control of photovoltaic systems for enhanced short-term voltage stability and recovery," IEEE Transactions on Energy Conversion, vol. 34, no. 1, pp. 243–254, 2018

[13] S. R. Islam, D. Sutanto, and K. M. Muttaqi, "Coordinated Decentralized Emergency Voltage and Reactive Power Control to Prevent Long-Term Voltage Instability in a Power System,"

IEEE Transactions on Power Systems, vol. 30, no. 5, pp. 2591–2603, Sep. 2015, doi: 10.1109/TPWRS.2014.2369502.
[14] A. M. Howlader, S. Sadoyama, L. R. Roose, and Y. Chen, "Active power control to mitigate voltage and frequency deviations for the smart grid using smart PV inverters," Appl Energy, vol. 258, p. 114000, Jan. 2020, doi: 10.1016/J.APENERGY.2019.114000.
[15] N. Edoo, R. T. F Ah King, N. Manoj Kumar, and S. Kichou, "Techno-Economic Analysis of Utility-Scale Solar Photovoltaic Plus Battery Power Plant," Energies 2021, Vol. 14, Page 8145, vol. 14, no. 23, p. 8145, Dec. 2021, doi: 10.3390/EN14238145.
[16] M. Bortolini, M. Gamberi, and A. Graziani, "Technical and economic design of photovoltaic and battery energy storage system," Energy Convers Manag, vol. 86, pp. 81–92, Oct. 2014, doi: 10.1016/J.ENCONMAN.2014.04.089.
[17] NERC, "Energy Storage: Impacts of Electrochemical Utility-Scale Battery Energy Storage Systems on the Bulk Power System," 2021.
[18] NERC, "Reliability Guideline: BPS-Connected Inverter-Based Resource Performance," 2018.
[19] "IEEE Draft Standard for Interconnection and Interoperability of Inverter-Based Resources (IBR) Interconnecting with Associated Transmission Electric Power Systems," P2800/D6.3, December 2021, pp. 1–181, 2021.
[20] Z. Li, G. Yao, G. Geng, and Q. Jiang, “An efficient optimal control method for open-loop transient stability emergency control,” IEEE Transactions on Power Systems, vol. 32, no. 4, pp. 2704–2713, 2016.
[21] I. Genc, R. Diao, V. Vittal, S. Kolluri, and S. Mandal, “Decision treebased preventive and corrective control applications for dynamic security enhancement in power systems,” IEEE Transactions on Power Systems, vol. 25, no. 3, pp. 1611–1619, 2010.
[22] Y. Zhang, X. Shi, H. Zhang, Y. Cao, and V. Terzija, “Review on deep learning applications in frequency analysis and control of modern power system,” International Journal of Electrical Power & Energy Systems, vol. 136, p. 107744, 2022.
[23] D. Ernst, M. Glavic, and L. Wehenkel, “Power systems stability control: reinforcement learning framework,” IEEE transactions on power systems, vol. 19, no. 1, pp. 427–435, 2004.
[24] J. R. Vazquez-Canteli and Z. Nagy, “Reinforcement learning for demand ´ response: A review of algorithms and modeling techniques,” Applied energy, vol. 235, pp. 1072–1089, 2019.
[25] M. Pavella, D. Ernst, and D. Ruiz-Vega, “Closed-loop emergency control,” in Transient Stability of Power Systems. Springer, 2000, pp. 171–188.
[26] Q. Huang, R. Huang, W. Hao, J. Tan, R. Fan, and Z. Huang, “Adaptive power system emergency control using deep reinforcement learning,” IEEE Transactions on Smart Grid, vol. 11, no. 2, pp. 1171–1182, 2019.
[27] M. Zhou and Q. Huang, “Interpss: A new generation power system simulation engine,” arXiv preprint arXiv:1711.10875, 2017.

[28] Modeling and validation work group, “White paper on modeling and studying FIDVR events,” Western Electricity Coordinating Council, Technical Report, October 20, 2011.
[29] North American Electric Reliability Corporation, Reliability Standard TPL-001-4, Transmission System Planning Performance Requirements.
[30] M. Paramasivam,” Dynamic optimization based reactive power planning for improving short-term voltage performance”, PhD Dissertation, Iowa State University.
[31] North American Transmission Forum, Transient voltage criteria reference document, September 2016
[32] WECC Modeling and Validation Working Group, “Solar Photovoltaic Power Plant Modeling and Validation Guideline” Dec 9, 2019, Available: https://www.wecc.org/Reliability/Solar%20PV%20Plant%20Modeling%20and%20Validation%20Guidline.pdf
[33] S. Dasgupta, M. Paramasivam, U. Vaidya, and V. Ajjarapu, "Entropy-Based Metric for Characterization of Delayed Voltage Recovery," IEEE Transactions on Power Systems, vol. 30, no. 5, pp. 2460–2468, Sep. 2015, doi: 10.1109/TPWRS.2014.2361649.
[34] NERC, “Standard PRC-024-2-Generator Frequency and Voltage Protective Relay Settings”, available at: https://www.nerc.com/pa/Stand/Reliability%20Standards/PRC-024-2.pdf
[35] T. van Cutsem et al., "Test Systems for Voltage Stability Studies," IEEE Transactions on Power Systems, vol. 35, no. 5, pp. 4078–4087, Sep. 2020, doi: 10.1109/TPWRS.2020.2976834.
[36] T. P. Lillicrap, J. J. Hunt, A. Pritzel, N. Heess, T. Erez, Y. Tassa, D. Silver, and D. Wierstra, “Continuous control with deep reinforcement learning,” arXiv preprint arXiv:1509.02971, 2015
[37] Siemens PTI Power Technologies Inc., PSS/E 35.3.2, Application Program Interface (API), Vol. II, Dec 2021
[38] Brockman, G., Cheung, V., Pettersson, L., Schneider, J., Schulman, J., Tang, J. and Zaremba, W., 2016. Openai gym. arXiv preprint arXiv:1606.01540.
[39] Raffin, Antonin, Ashley Hill, Maximilian Ernestus, Adam Gleave, Anssi Kanervisto, and Noah Dormann. "Stable baselines3." 2019.
[40] Paul Krauss, “Analysis of Electric Machinery and Drive Systems”, 2nd Edition.
[41] M. Sarwar, A. R. R. Matavalam and V. Ajjarapu, "Deep Reinforcement Learning Framework for Short-Term Voltage Stability Improvement," 2023 IEEE Texas Power and Energy Conference (TPEC), College Station, TX, USA, 2023, pp. 1-6, doi: 10.1109/TPEC56611.2023.10078572.
[42] M. Sarwar, A. Reddy Ramapuram Matavalam and V. Ajjarapu, "Characterization and Mitigation of Fault Induced Delayed Voltage Recovery with Dynamic Voltage Support by Hybrid PV Plants," 2022 North American Power Symposium (NAPS), Salt Lake City, UT, USA, 2022, pp. 1-6, doi: 10.1109/NAPS56150.2022.10012146.

Part II

Grid forming Inverter Controls to Improve FIDVR While respecting Inverter Current Limitations

Hugo Villegas Pico
Abdelrehman Mannan, Graduate Student

Iowa State University

For information about this project, contact

Hugo Villegas Pico,
Iowa State University,
Department of Electrical and Computer Engineering,
Ames, Iowa, USA 50011-3060
Phone: 515-294-4889
Email: hvillega@iastate.edu

Power Systems Engineering Research Center

The Power Systems Engineering Research Center (PSERC) is a multi-university Center conducting research on challenges facing the electric power industry and educating the next generation of power engineers. More information about PSERC can be found at the Center's website: http://www.pserc.wisc.edu.

For additional information, contact:

Power Systems Engineering Research Center
Arizona State University
527 Engineering Research Center
Tempe, Arizona 85287-5706
Phone: 480-965-1643
Fax: 480-727-2052

Notice Concerning Copyright Material

Table of Contents

List of Figures

List of Tables

1. Introduction

1.1 Background

The U.S. Department of Energy reported that solar technologies could generate as much as 40% of the U.S. electricity supply by the year 2035 and 45% by 2050 [1]. Notably, 42% of the 2022 U.S. solar projects were to employ hybrid resources: photovoltaic (PV) arrays and battery energy storage (BES) [2]. Nevertheless, there are several challenges to be solved for the reliable integration of solar assets [1], [3], [4]. For instance, hybrid PV solar resources will be challenged to energize single-phase induction motors (SPIMs) after a black-out and ride through fault-induced delayed voltage recovery (FIDVR) events [1, p. 73].

Historically, restoration of SPIMs has been easily accomplished by synchronous generators [5], [6]. These generators have also been critical to source over-rated currents during FIDVR events to heat up SPIM thermal relays for their disconnection [7, pp. 846–849], [8]. FIDVR events materialize in the form of sustained low voltages that emerge from grid faults that cause the stalling of SPIMs driving residential air-conditioning (A/C) compressors [9]. Techniques to alleviate FIDVR include under-voltage load shedding [10]–[13], var-compensators [14], [15], admittance/impedance detection [16],[17], and motor under-speed tripping [18] to name a few.

1.2 Literature Review

At present, grid-forming (GFM) inverter-based resources (IBRs), such as wind and solar, are expected to power the U.S. grid-like synchronous machines [19]–[22]. However, one The problem with this transition is that GFM IBRs powered by hybrid resources are still under research [22], [23]. Further, a major concern is that GFM IBRs cannot source over-rated currents, which can jeopardize the starting up of SPIMs and the riding through of FIDVR events [4], [22]. Notably, SPIM restoration and FIDVR problems are likely to persist because residential A/C units are used in 87% of U.S. homes [24].

For the reliable integration of hybrid PV solar resources into the U.S. grid, which also extrapolates worldwide, it is critical to address the following research needs: (C1) A controller for dc-coupled hybrid resources that power GFM IBRs. Present GFM strategies do not consider IBRs powered by dc-coupled PV array and BES, e.g., see [22], [23], [25], [26]. (C2) A realistic compressor model to study restoration and FIDVR events of clusters of SPIMs. Behavioral models [27]–[29] do not capture the compressor nature during SPIM acceleration from a stall. Notably, detailed models are crucial for electromagnetic transient (EMT) studies, as recommended by the North American Electric Reliability Corporation (NERC) [30]. (C3) An analysis to ascertain whether SPIM thermal protection is still viable to mitigate FIDVR events. Present literature has not elucidated the impact of IBRs current-limitation on thermal protection [22], [23], [31]. (C4) A realistic analysis of the EMT performance of distribution feeders powered by hybrid GFM IBR during restoration and FIDVR events. Classical EMT studies consider that feeders are energized by stiff power sources [32], [33]. Notably, a recent positive-sequence study reports the instability of GFM IBRs during FIDVR events [31]. These challenges are addressed here via three contributions:

1) A controller for dc-link voltage regulation of GFM IBRs with dc-coupled PV array and BES, q.v. Section 2.1.1. The novelty is the engineering of simple anti-windup proportional-integral (PI) regulators to optimally charge and discharge the BES under varying solar irradiance.

2) A physics-based and computationally light compressor model with four compression stages, q.v. Section 2.2.2. The novelty is that it captures both SPIM acceleration and deceleration in EMT simulations, which contrasts behavioral ones for deceleration only [27]–[29].

3) A demonstration that IBR's current limitations will delay the tripping of SPIM thermal relays, implying longer FIDVR events, q.v. Section 3.1.1. Hence, protection is engineered to disconnect stalled SPIMs by estimating impedance and deceleration, q.v. Section 3.1.3.

These contributions are: (i) built on the reliable GFM technology using two-axis anti-windup PI regulators [34]; (ii) demonstrated via detailed EMT simulations of a classical distribution feeder [28], but powered only by hybrid IBRs; (iii) significant to achieve local energy-assured generation which NERC identifies as necessary for reliability and resilience [35, 2 p. 3]; (iv) crucial to satisfy NERC recommendations on EMT simulations [30]; and (v) important to address NERC guidelines on hybrid PV plant performance [36]. Here, GFM IBRs can stably withstand SPIM restoration and FIDVR transients.

1.3 Preliminaries

Figure 1.1 shows a GFM IBR powered by dc-coupled PV arrays and BES. It has a buck-boost converter (BBC), a dc-link capacitor, Cdc, a grid-side inverter (GSI), ac inductive capacitive (LC) filter, and step-up transformer (XFMR). The BBC switches are driven by a buck-boost modulator (BBM). The GSI switches are steered by ac voltage/current controllers and an extended sine triangle modulator (ESTM) [37, pp. 483– 485]. A set of IBRs are used to restore the feeder of Fig. 1.2.

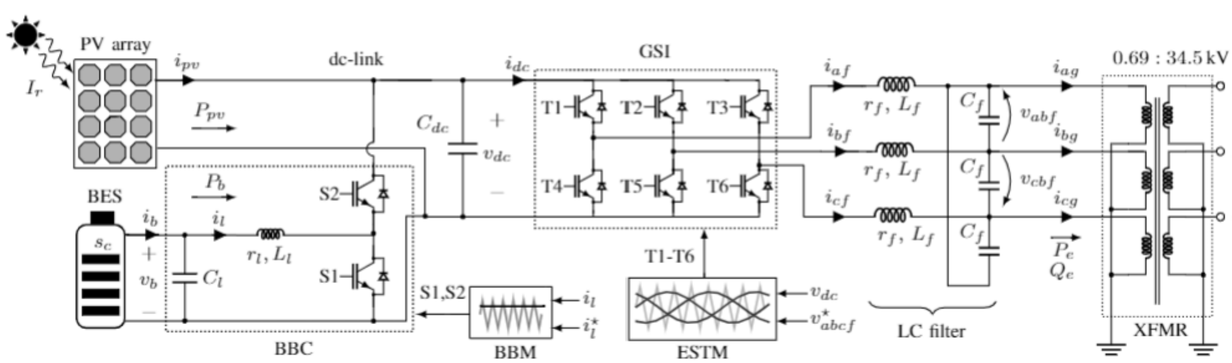

Figure 1.1 Grid-forming subsystem including PV array, battery energy storage (BES), buck-boost converter (BBC), buck-boost modulator (BBM), grid-side inverter (GSI), extended sine-triangle modulator (ESTM), and step-up transformer (XFMR) [36].

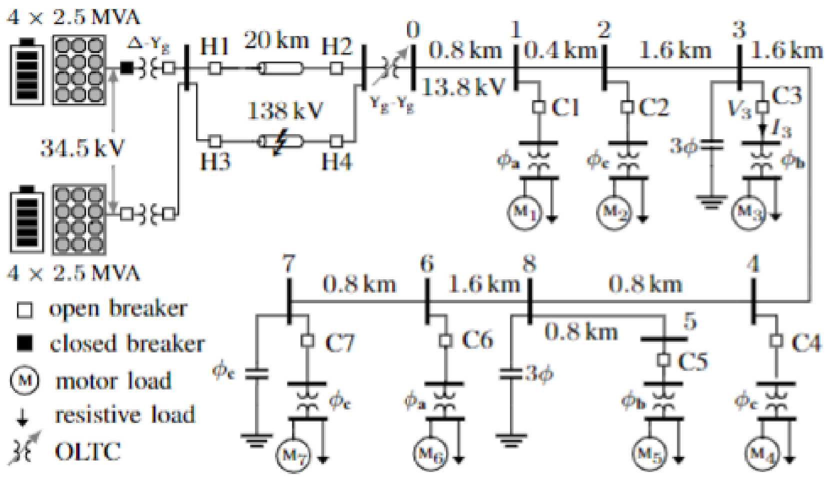

Figure 1.2 Radial feeder with clusters of single-phase motor and resistive

1.3.1 Grid-Forming Strategy

To control the GSI of Fig. 1.1, this work adopts the GFM technology of [34] which is illustrated in Fig. 1.3. The voltage and current controllers use qd-axis anti-windup PI regulators. In Figs. 1.3a and 1.3b, $v^c_{qdf} = K_v(\theta_c)[v_{abf}, v_{abf}]^T$, $i^c_{qdx} = K_i(\theta_c)[i_{ax}, i_{bx}]^T$, for $x \in \{f, g\}$, $i^{\dagger}_{qdf} = 3C_f\omega_b v^c_{qdc} + i^c_{qdg}$, and $v^c_{qdf} = [v^c_{df}, -v^c_{qf}]^T$. The matrices $K_v(\theta_c)$ and $K_i(\theta_c)$ are from [37, pp. 112–113]. The command $v^{\star}_{qdf} = [\sqrt{2/3}V^{\star}_f, 0]$ where $V^{\star}_f$ is the rms line-to-line voltage set-point. The reference frame angle $\theta_c \in [0, 2\pi)$ is from Fig. 1.3c. There, k_ω is a droop constant, ω_b is the base angular frequency, $P_{e,mx}$ is rated electric power, and $\widetilde{P_e}$ is a filtered version of $P_e = 3/2(v^c_{qf}i^c_{qg} + v^c_{df}i^c_{dg})$. The set points ω^*_c and P^*_e in Fig. 1.3c are used for frequency control and power dispatch.

In Fig. 1.3a and 1.3b, the function $\xi: \mathbb{R}^2 \text{ x } \mathbb{P} \rightarrow \mho$

$$\xi(u^*_{qd}, U_{mx}) = \begin{cases} \frac{U_{mx}}{U} & if\ U > U_{mx} \neq 0 \\ u^*_{qd} & otherwise \end{cases} \quad (1)$$

With $U = (u^{*2}_q + u^{*2}_d)^{1/2}$ serves to bound u^*_{qd} within an origin-centered circle of radius U_{mx}. This functionality maintains GSC current commands within ratings during large transients while automatically stopping PI integration to prevent instability [34]. The ESTM commands $v^{\star}_{abcf} = [v^{\star}_{af}, v^{\star}_{bf}, v^{\star}_{cf}]^T$ in Fig. 1.1 are mapped from $v^{\star}_{qdf}$ in Fig. 1.3b [37].

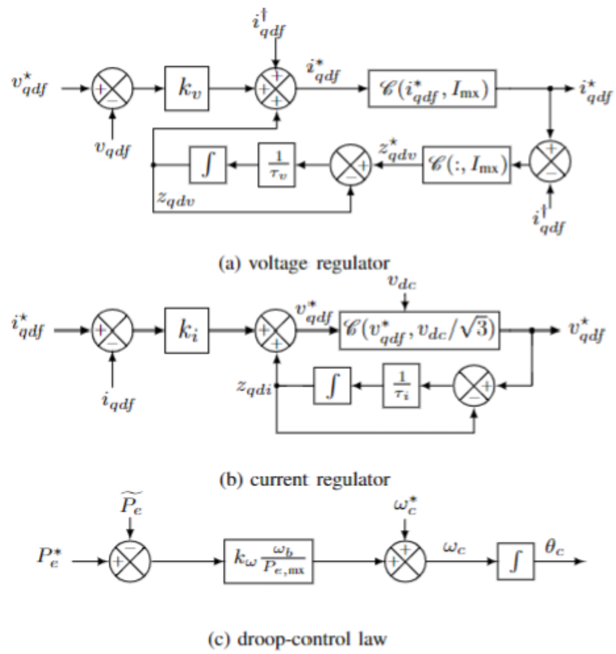

Figure 1.3 Grid-forming voltage and current PI regulators, as well as droop-control

1.3.2 Restoration of Distribution Feeders

GFM IBRs are challenged to start up clusters of SPIM loads and withstand FIDVR during restoration because of GSI current limitation [31], [39]. Notably, FERC and NERC have reported that restoration plans do consider instances of locked rotor currents by motors [5, p. 34]. In Fig. 1.2, for example, eight 2.5-MVA GFM IBRS as the one in Fig. 1.1 are challenged to energize 6.6-MW c.a. of SPIMs driving (compressors and condenser fans) and 1.4-MW of resistive loads.

A possible restoration plan for the grid in Fig. 1.2 is: (i) energize the 12-MVA 34.5/138-kV Δ-Yg transformers of each PV plant by closing their circuit breakers; (ii) energize the 138- kV overhead transmission lines by closing H1–H4 which in turn power the Yg-Yg transformer and buses '0' to '8'; and (iii) sequentially energize each cluster of 177 SPIMs driving A/C compressors and resistive loads by closing breakers C1 to C7. The on-load tap changer (OLTC) [next to the bus '0' in Fig. 1.2] serves to compensate for voltage drops in the 138-kV transmission lines as well as the Δ-Yg and Yg-Yg transformers. Next, this work develops the technology to materialize the restoration of feeders using hybrid IBRs.

1.4 Report Organization

The remainder of this report is as follows. Section 2 discusses the control of hybrid PV plants with grid-forming control as well as restoration and FIDVR events. Section 3 develops controls for motor stalling protection and compares the response of IBR and synchronous generators. Section 4 develops three case studies, and Section 5 concludes the report.

2. Control of Hybrid Resources

The main novelty of this section is a control strategy to charge or discharge the BES by using the BBC and the BBM, q.v. Fig. 2.2. From Fig. 1.1, one can realize that the battery may be charged if: (i) the power transferred to the ac grid P_e (plus losses) is less than the maximum PV power P_{pv} and (ii) the state of charge (SoC), s_c is less than the maximum SoC, $\overline{s_c}$. Conversely, the battery may be discharged if: (i) P_e (plus losses) is greater than the maximum P_{pv} and (ii) s_c is greater than the minimum SoC, $\underline{s_c}$. This task is achieved by calculating an optimal dc voltage set point, as explained next.

2.1 Dc Voltage Set-Point for Optimal Hybrid Operation

To optimally harvest PV array power P_{pv} of Fig. 1.1 for ac generation and battery usage during grid-forming operation, it is necessary to estimate the voltage set-point v_{dc}^* so that $P_{pv}\ (v_{dc})$ is maximum when $v_{dc} \rightarrow v_{dc}^*$. As done in [40], such estimation is achieved by using an abstract model of the PV array as well as the measured voltage v_{dc} and current i_{pv} in Fig. 1.1. The PV array in Fig. 1.1 comprises of Np parallel-connected strings, each of which has Ns series-connected PV modules. Each module is modeled using a single-diode equivalent circuit [41]. From measured v_{dc} and i_{pv} in Fig. 1.1, an estimation of the light-generated current, i_g, of each PV module is [40]:

$$\widehat{i_g} = i_d + i_{sh} + i_{pv}/Np \quad \text{where} \quad i_d = i_0\left(e^{\frac{v_d}{v_T}} - 1\right) \tag{2}$$

$$v_d = \frac{v_{dc}}{\mathrm{Ns}} + R_s i_{pv} \quad \text{and} \quad i_{sh} = \frac{v_d}{R_{sh}} \tag{3}$$

Which serves as input to calculate the $v_d = v_d^*$ that maximizes:

$$\frac{P_{pv}(v_d)}{NsNp} = v_d i_{gd}(v_d) - R_s\left(i_{gd}(v_d) - \frac{v_d}{R_{sh}}\right)^2 - \frac{v_d^2}{R_{sh}} \tag{4}$$

Where $i_{gd}(v_d) = i_g - i_0\left(e^{\frac{v_d}{v_T}} - 1\right)$ (5)

In (2)–(5): (i) the parameters v_T , i_0, R_s and R_{sh} and (ii) the variables i_g, v_d, and i_d are defined in [41]. The maximizer $v_d = v_d^*$ is unique because $P_{pv}(v_d)$ of (4) is concave on v_d [40]. Hence, v_d^* is uniquely determined by computing the zero of $dP_{pv}(v_d)/dv_d$ via convergent Newton Raphson iterations [40]. The optimal v_{dc}^* is obtained from:

$$v_d^* = \frac{R_{sh}}{R_s+R_{sh}}\left(\frac{v_{dc}^*}{Ns} + R_s i_{gd}(v_d^*)\right) \tag{6}$$

Please, recall that $i_{gd}(v_d)$ is defined in (5)

2.1.1 Dc-Link Voltage Control

The novelty of this subsection is a control strategy to regulate the dc-link voltage, v_{dc}, of the GFM in Fig. 1.1. The strength of the proposed dc-link voltage control strategy is its simplicity which is important for industry adoption. In particular, v_{dc} is regulated by steering the dc-link capacitor energy $E^*_{dc} = \frac{1}{2}C_{dc}v_{dc}^2$ so that it follows the set-point

$$E^*_{dc} = \frac{1}{2}C_{dc}\max\{(v^*_{dc})^2, (v_{mn})^2\} \tag{7}$$

where v^*_{dc} is from (6) for maximum PV power harvesting. Here, v_{mn} ensures maintaining minimum dc-link voltage during low irradiance events for GSI control [40]. Specifically, the regulation of E_{dc} (or v_{dc}) is achieved by steering i_l of Fig. 1.1 so that it follows:

$$i_l^\star = \mathcal{J}(i_l^*, \underline{i_l^\star}, \overline{i_l^\star}) \text{ with } i_l^* = k_{dc}(E^\star_{dc} - E_{dc}) + z_{dc} \tag{8}$$

$$\text{and} \qquad \frac{d}{dt}z_{dc} = \frac{1}{\tau_{dc}}(-z_{dc} + i_l^\star) \tag{9}$$

This control law, shown in Fig. 4, is a one-axis or univariate PI regulator with anti-windup capability [34]. The parameters k_{dc} and τ_{dc} are the proportional and integration-time constants, respectively. The saturation function: $\mathcal{J}$: ℝ x ℝ x ℙ→ ℝ:

$$\mathcal{J}(x, \underline{x}, \overline{x}) = \begin{cases} x & if\ x \in [\underline{x}, \overline{x}] \\ \underline{x} & if\ \ x < \underline{x} \\ \overline{x} & if\ \ x > \overline{x} \end{cases} \tag{10}$$

of (8) serves to: (i) ensure the BES SoC $s_c \in [\underline{s_c}, \overline{s_c}]$ and (ii) ensure the command $i_l \in [\underline{i_l}, \overline{i_l}]$. Specifically, for (8):

$$\overline{i_l^\star} = \begin{cases} 0 & if\ \ s_c \le \underline{s_c} \\ \overline{i_l} & if\ \ s_c > \underline{s_c} \end{cases} \quad \text{and} \quad \underline{i_l^\star} = \begin{cases} \underline{i_l} & if\ \ s_c < \overline{s_c} \\ 0 & if\ \ s_c \ge \overline{s_c} \end{cases} \tag{11}$$

In this research work, it is assumed that s_c is observable; $\underline{s_c}$ and $\overline{s_c}$ are minimum and maximum SoC limits. Next, i_l of (8) steers the BBC of Fig. 1.1 for charging or discharging the BES.

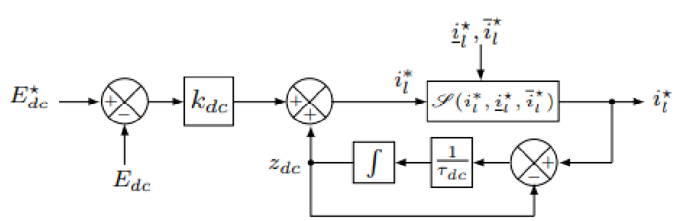

Figure 2.1 Dc-link voltage PI regulator to control v_dc of Fig. 1.1

2.1.2 Buck-Boost Control

The novelty of this subsection is the current controller and the BBM of Fig. 2.2 as using one-axis anti-windup PI regulators. They are engineered to steer the BBC of Fig. 1.1 for charging and discharging the BES as well as the seamless grid-forming operation of the GSI. In particular, the mission of the current controller in Fig. 2.2a is to drive $i_l \rightarrow i_l^\star$ of (8) by generating modulation index commands, $d_b^\star$ or $d_c^\star$, for boost or buck operation.

The modulator in Fig. 2.2b generates PWM commands to turn on and off the switches S1 and S2 in Fig. 1.1 to discharge and charge the BES, respectively.

The buck or boost mode in Fig. 5b is selected via:

$$\gamma^\star = \begin{cases} 0 & if\ i_l^\star \geq 0 \quad for\ boost\ mode \\ 1 & if\ i_l^\star < 0 \quad for\ buck\ mode \end{cases} \tag{12}$$

For boost mode, the modulation index set-point satisfies:

$$d_b^\star = \mathcal{I}(d_b^*, 0, \overline{d_b^\star}) \text{ with } d_b^* = k_b(\widetilde{\iota_l} - i_l^\star) + z_b \tag{13}$$

$$\text{and} \qquad \frac{d}{dt} z_b = \frac{1}{\tau_b}(\text{-}z_b + d_b^\star) \tag{14}$$

which is the anti-windup PI regulator on the top of Fig. 2.2a. The parameters k_b and τ_b are proportional and integration-time constants. The filtered current $\widetilde{\iota_l}$ in (13) [and (16)] satisfies:

$$\frac{d}{dt}\widetilde{\iota_l} = \frac{1}{\tau_l}(\text{-}\widetilde{\iota_l} + i_l) \tag{15}$$

with i_l in Fig. 1. For buck mode, the modulation index:

$$d_c^\star = \mathcal{I}(d_c^*, 0, \overline{d_c^\star}) \text{ with } d_c^* = k_c(i_l^\star - \widetilde{\iota_l}) + z_c \tag{16}$$

$$\text{and} \qquad \frac{d}{dt} z_c = \frac{1}{\tau_c}(\text{-}z_c + d_c^\star) \tag{17}$$

which is the anti-windup PI regulator in the bottom of Fig. 2.2a. The parameters k_c and τ_c are proportional and integration-time constants.

The limits $\overline{d_b^\star}$ of (13) and $\overline{d_c^\star}$ of (16) satisfy:

$$\overline{d_b^\star} = \begin{cases} 1 & if\ s_c > \underline{s_c}\ and\ i_l^\star > 0 \\ 0 & otherwise \end{cases} \tag{18}$$

$$\overline{d_c^\star} = \begin{cases} 1 & if\ s_c < \overline{s_c}\ and\ i_l^\star < 0 \\ 0 & otherwise \end{cases} \tag{19}$$

They serve to not overcharge the BES if the SoC, s_c, is too high and block battery discharging if s_c is too low. Please note in Fig. 2.2a that the modulation indices $d_b^\star$of (13) and $d_c^\star$ of (16) are commands to the BBM in Fig. 2.2b. Also note in Fig. 2.2b that each modulation index is compared against a triangular waveform w with switching period τsw for activation of S1 and S2. The switch activation commands, S1 and S2, are delayed by τd to prevent shoot-through [37, p. 420].

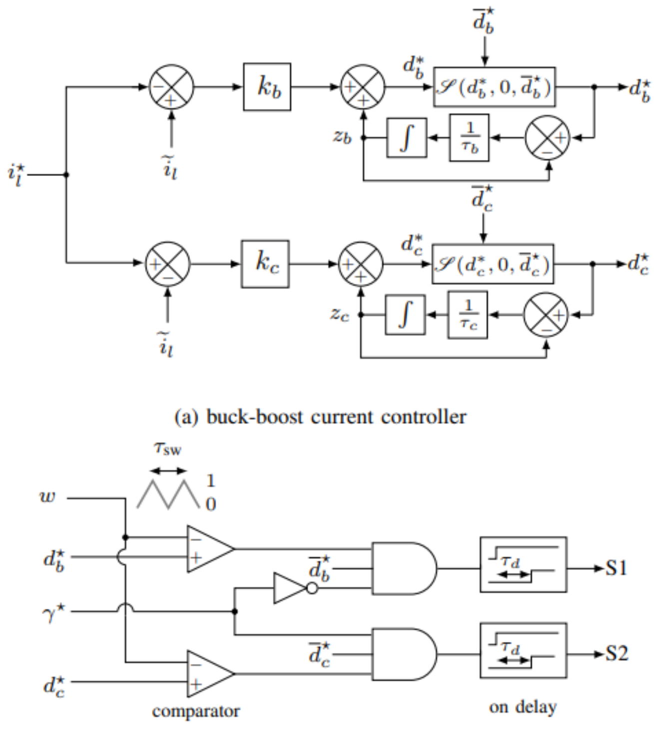

(b) buck-boost modulator (BBM)

Figure 2.2 Buck-boost current controller and its modulator.

2.2 Compressor Model

The novelty is a computationally-light physics-based model of a residential A/C compressor, q.v. Fig. 2.2. This model is critical for EMT studies of restoration and FIDVR events involving GFM IBRs. Compressor modeling is labeled as complicated [28]; thus, behavioral models are used [27]–[29].

2.2.1 Behavioral Compressor Model

A motor-compressor subsystem is depicted in Fig. 2.3. A SPIM is used to drive two piston-cylinder assemblies [42]. In Fig. 2.3a, the rotor angular speed, ω_m, and position, θ_m meet:

$$\frac{d}{dt}\omega_m = \frac{1}{J}(T_e - T_m) \quad \text{and} \quad \frac{d}{dt}\theta_m = \omega_m \tag{20}$$

The inertia constant, J, aggregates the impact of the rotor, pistons, and counterweights [42] on rotor dynamics; assume rigid connecting rods of length l.2 The nature of electrical torque, T_e, is rigorously modeled [28], [44]; but, the mechanical torque, T_m, is behaviorally represented [8],

[28]. Because T_e and T_m in (20) are algebraically additive, they are both important for restoration and FIDVR analyses.

Behaviorally, $T_m \approx T_{speed} + T_{av}$ for (20) where [28]: (i) T_{speed} is proportional to ω_m^2 and (ii) T_{av} (of triangular shape) is dependent on θ_m and a user-defined amplitude. In an EMT implementation, T_{av} is kept at zero until the SPIM rotor has surpassed a certain speed in time [27, p. 26–27]. This practice constraints engineers to simulate SPIM impacts on restoration and FIDVR events if the rotor does not accelerate due to high compressor torque, low ac voltage, or wrong choice of start-run capacitors. A realistic compressor model follows.

2.2.2 Realistic Compressor Model

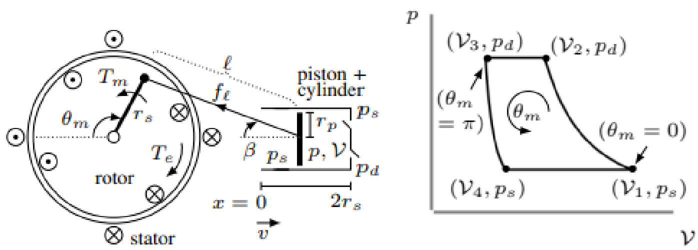

(a) motor and compressor assembly (b) p vs. $\mathcal{V}$ behavior

Figure 2.3 Motor and compressor assembly and compressor pressure vs. volume characteristic. Only one piston-cylinder set out of two is illustrated.

The parameters and variables to model a reciprocating compressor are shown in Fig. 2.3a. The torque T_m of (20) meets:

$$T_m = D_p\omega_m^2 + T(\theta_m, \omega_m) + T(\theta_m + \pi, \omega_m) \tag{21}$$

if $|\omega_m| > 0$; otherwise $T_m = 0$. In (21): (i) $D_p\omega_m^2$ is from an oil pump and (ii) $T(\theta_m, \omega_m)$ and $T(\theta_m + \pi, \omega_m)$ are by two twin compressor pistons that are π rad out of phase [42]. Specifically:

$$T(\theta_m, \omega_m) = (\sin\theta_m \cos\beta - \frac{r_s}{2l}\sin 2\theta_m) r_s f_l \tag{22}$$

Where $f_l \cos\beta = D_f v + f_p$ (23)

$$\cos\beta = \sqrt{1 - \frac{r_s^2}{l^2}\sin^2\theta_m} \tag{24}$$

under the assumption of stiff connecting rods of length l, each transmitting force f_l , q.v. Fig. 2.3a. Note that (22) is from the component of f_l that is perpendicular to the radius r_s. Also, the horizontal projection of f_l in (23) transmit the forces developed by piston friction $D_f v$ and cylinder pressure f_p. In (23), D_f is a friction constant and v is the piston speed:

$$v(\theta_m, \omega_m) = r_s \omega_m \sin\theta_m - \frac{1}{2}\frac{\omega_m l}{cos\beta}\frac{r_s^2}{l^2} \sin 2\theta_m \tag{25}$$

Further, the force f_p , developed by the gas-refrigerant pressure p in a sealed compressor for (23) satisfies:

$$f_p = \pi r_p^2 (p - p_s). \tag{26}$$

In Fig. 2.3b, the behavior of p $vs.$ V for isentropic 3 compression, discharge, expansion, and intake stages satisfies:

$$p = \begin{cases} \min\left\{p_s\left(\frac{V}{V_1}\right)^{m_{12}}, p_d\right\} & if\ |\theta_m| \in [0, \pi) \\ \max\left\{p_s\left(\frac{V}{V_4}\right)^{m_{34}}, p_s\right\} & otherwise \end{cases} \tag{27}$$

With $V = V_3 - \frac{V_1 - V_3}{2r_s}(x - r_s)$, (28)

$$m_{12} = \frac{\ln\left(\frac{p_d}{p_s}\right)}{\ln\left(\frac{V_2}{V_1}\right)}, \text{ and } m_{34} = \frac{\ln\left(\frac{p_d}{p_s}\right)}{\ln\left(\frac{V_3}{V_4}\right)} \tag{29}$$

In (26) and (27), p_s is the suction pressure and p_d the discharge pressure. The min and max operators in (27) serve to automatically switch the discharge-to-expansion and intake-to-compression processes at $|\theta_m| = \pi$ and $|\theta_m| = 2\pi$, respectively, q.v. Fig. 2.3b. This novelty relieves the complex task of modeling the dynamics of discharge and intake valves, e.g., see [42]. In (28), the piston position $x \in [0, 2r_s]$ is from:

$$x(\theta_m) = r_s - r_s cos\theta_m + lcos\beta - l \tag{30}$$

Please, note that p of (27) and V of (28) depend on θ_m of (20). Also, note that (22) require computationally light operations via (23)–(30) for given θ_m and ω_m from (20)

3. Motor Stalling Protection

It is shown here that thermal relays will face longer tripping times to disconnect stalled SPIMs when powered by IBRs than by synchronous machines. Thus, an electronic protection is engineered by estimating SPIM impedance and acceleration.

3.1 Classical Thermal Protection

The tripping time of a thermal relay is [46]:

$$t_{rly} = \tau_{rly} \ln\left(\frac{I_m^2 - I_{m,opr}^2}{I_m^2 - I_{m,rly}^2}\right) \quad for\ I_m > I_{m,rly} \tag{31}$$

Here, τ_{rly} is the relay thermal time constant, I_m is the present rms current of the SPIM undergoing stalling, $I_{m,opr}$ is the rms current of a SPIM previous to stalling, and $I_{m,rly}$ is the pickup current of the thermal relay. In this work, $I_m \in \{I_m^{\diamond}, I_m^{\lhd}\}$ where $I_m^{\diamond}$ and $I_m^{\lhd}$ are respectively the SPIM rms currents produced by an IBR and a machine, q.v. Fig. 3.1a and 3.1b.

In Fig. 3.1a, the SPIM current when powered by an IBR is:

$$I_m^{\diamond} = \frac{1}{1+jB_f(jX_g+jX_l+Z_m)}\widetilde{I_f} \tag{32}$$

Where $\widetilde{I_f} = \min\{I_f^*, I_{mx}\}\angle\,\phi_f$ is from the current command:

$$I_f^*\angle\,\phi_f = \frac{jB_f(jX_g+jX_l+Z_m)+1}{jX_g+jX_l+Z_m}\widetilde{V_f^*} \tag{33}$$

for $\widetilde{V_f^*} = V_f^{\star}\angle 0$. Here, $V_f^{\star}$ and I_{mx} are respectively the IBR voltage set-point and its rated current. To the Authors' understanding, (32) and (33) have not been posed in the literature for analysis of thermal relays because they are a consequence of Section 1.3.1. The parameter X_l encapsulates the reactances of transformers and transmission lines and Z_m models the impedance of the SPIM.

From (32)–(33), the rms voltage magnitude of:

$$\widetilde{V_f} = (jX_g + jX_l + Z_m)\widetilde{I_m^{\diamond}} \tag{34}$$

in Fig. 3.1a is maintained at $V_f^{\star}$ only if $I_f^* \leq I_{mx}$ as a result of the voltage regulator with current limiter discussed in Section 1.3.1. Otherwise, the voltage magnitude of (34) drops because of (32) and (33). In the proposed technique, $\widetilde{I_m^{\diamond}}$ of (32) and Fig. 3.1a is contrasted against the one in Fig. 3.1b:

$$I_m^{\lhd} = \frac{\tilde{E}}{jX_d'+jX_l+Z_m} \tag{35}$$

With $\tilde{E} = E\,\angle 0$ the voltage behind a transient reactance, X_d' , of a classical synchronous machine model [7].

In Fig. 3.1c, $I_m^{\diamond}$ and $I_m^{\triangleleft}$ can be as high as 2.25 p.u. and 4.83 p.u., respectively. Hence, the thermal relay can trip only as fast as $t_{rly}^{\diamond}$= 13.24 s and $t_{rly}^{\triangleleft}$= 1.44 s if ω_m= 0 (i.e., when the motor stalls) for the inverter and machine cases, respectively. Notably, a tripping time of $t_{rly}^{\diamond}$ = 13.24 s is relatively long with respect to $t_{rly}^{\triangleleft}$ = 1.44 s. Hence, an approach to stalling protection for converter-based grids is proposed in Section 3.1.3 and tested in the EMT domain in Section 4. In Fig. 3.1, the ratings of the IBR and the synchronous machine are assumed to be twice of that of the SPIM. To generate Fig. 3.1c, E = 1.05, X_d' = 0.075, X_l= 0.05, X_g = 0.025, B_f= 0.48, V_f^* = 1.0, I_{mx} = 2.0, $I_{m,opr}$ = 1.0, τrly = 10 s, and ω_m = 0 p.u. The value of Zm is from Fig. 3.2; its calculation for any ω_m follows.

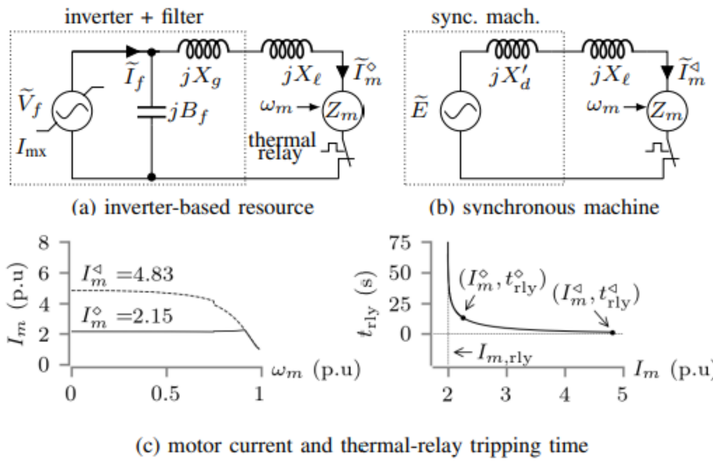

Figure 3.1 SPIM current when powered by IBR vs. synchronous generator

3.2 Asymmetrical Motor Impedance

The impedance Z_m of an asymmetrical motor with start-run capacitor for (32)–(35) as function of ω_m of (20) is :

$$Z_m(\omega_m) = \frac{\widetilde{V_{sm}}}{\widetilde{I_{sm}}+\widetilde{I_{sa}}} \tag{36}$$

where the currents $\widetilde{I_{sm}}$ and $\widetilde{I_{sa}} = N_{ma}\widetilde{I_{sa}'}$ sa respectively model the main and auxiliary winding ones (q.v. Fig. 3.2a) and meet:

$$\begin{bmatrix} \widetilde{V_{sm}} \\ \widetilde{V_{sa}'} \end{bmatrix} = \begin{bmatrix} Z_{11}(\omega_m) & Z_{12}(\omega_m) \\ Z_{21}(\omega_m) & Z_{22}(\omega_m) \end{bmatrix} \begin{bmatrix} \widetilde{I_{sm}} \\ \widetilde{I_{sa}'} \end{bmatrix} \tag{37}$$

The entries of this 2-by-2 matrix derive by studying in the frequency domain the two-axis circuit of [44, Fig. 1.3]. The entry $Z_{22}(\omega_m)$ encapsulates the switching of C_m in Fig. 9a for start C_m = C_{start} if ω_m < 0.75 p.u. and run C_m = C_{start} + C_{run} if $\omega_m \geq$ 0.75 p.u. In (36) and (37), $\widetilde{V_{sa}'}$= Nma $\widetilde{V_{sm}}$ and $\widetilde{V_{sm}}$ = Vm,rtd∠0 where Nma = Nm/Na is the main-to-auxiliary winding turn ratio and Vm,rtd is the rms rated voltage. The SPIM and capacitor parameters are from Table 4.3 in

Section 4. There, $|Z_m|$ is relatively low even if ω_m = 0.85 p.u. The jump of $\angle|Z_m|$ occurs when ω_m = 0.75 p.u. because C_m = C_{start} + C_{run}→ C_{start} [q.v. C_m in Fig. 3.2] when dω_m /dt < 0.

3.3 Proposed Electronic Stalling Protection

An electronic approach is proposed to disconnect a stalled SPIM powered by IBRs before under-voltage load shedding relays disconnect a complete feeder [11]. In Fig. 3.2b, the principle is to open the contactor when the SPIM impedance is relatively low and its rotor is decelerating. The novelty is that deceleration is estimated from impedance which is feasible only if impedance is monotonically increasing on rotor speed.

The estimated SPIM impedance with start-run capacitor is:

$$\widetilde{|Z_m|} = \frac{\sqrt{\Phi_v}}{\sqrt{\Phi_i}+\varepsilon} \tag{38}$$

$$\frac{d}{dt}\Phi_v = \frac{1}{\tau_c}(-\Phi_v + v_m^2) \quad and \quad \frac{d}{dt}\Phi_i = \frac{1}{\tau_c}(-\Phi_i + i_m^2) \tag{39}$$

The respective states Φ_v and Φ_i serve to filter the squares of the time-domain values of v_m and i_m in Fig. 3.2a. The time constant τ_c = 10/ω_b where ω_b is the rated electrical angular frequency. The parameter ε in (38) is a relatively small value to prevent division by zero when $i_m(t) = 0$.

To determine whether the rotor is decelerating, e.g., after a fault, consider the indicator function $\mathcal{J}$: $\mathbb{R} \rightarrow \mathbb{R}$:

$$\mathcal{J}\left(\frac{\mathrm{d}\widetilde{\omega_m}}{dt}\right) = \begin{cases} 1 & if \quad \frac{\mathrm{d}\widetilde{\omega_m}}{dt} < -\epsilon_\omega \\ 0 & \quad otherwise \end{cases} \tag{40}$$

$$\frac{d}{dt}\widetilde{\omega_m} = \frac{1}{\tau_f}\left(-\widetilde{\omega_m} + \omega_m^\dagger\right) \quad \text{with } \omega_m^\dagger = \mathcal{L}(\widetilde{|Z_m|}) \tag{41}$$

where ϵ_ω > 0 is a small parameter and $\widetilde{\omega_m}$ is the filtered version of the estimated rotor speed, $\omega_m^\dagger$, which is obtained from $\widetilde{|Z_m|}$ of (38) via (41). In (41), $\mathcal{L}$: Z → $\boldsymbol{\Omega}$ is a lookup table that is constructed offline from calculated coordinated pairs (|$|Z_m|$, ω_m), q.v. Section 3.1.2. Ascertaining acceleration/deceleration is possible only if $|Z_m|$ is monotonically increasing on ω_m which applies here, q.v. Otherwise, deceleration could be wrongly determined.

Lemma 1: $\frac{d|Z_m|}{dt} \neq 0$ and $\frac{d\omega_m}{dt}$ have the same signs only if $|Z_m|$is monotonically increasing on ω_m.

Proof: From the chain rule of time-domain quantities:

$$\frac{d|Z_m|}{dt} = \frac{d|Z_m|}{d\omega_m}\frac{d\omega_m}{dt} \tag{42}$$

the time-derivative signs are equal only if $\frac{d|Z_m|}{d\omega_m}$ > 0.

The stalling protection of Fig. 3.2b steers the status of the two-pole contactor in Fig. 3.2a via the following command:

$$c^* = \begin{cases} 0 & if \ \widetilde{|Z_m|} < |Z_m|^* \ and \ \mathcal{L}\left(\frac{d\widetilde{\omega_m}}{dt}\right) = 1 \\ h^* & otherwise \end{cases} \tag{43}$$

The contactor is open when $c^* = 0$ and closed if $c^* = 1$. The parameter $|Z_m|^*$ in (43) is a minimum permissible motor impedance when the rotor is decelerating. Please, recall from (41) that $\mathcal{L}\left(\frac{d\widetilde{\omega_m}}{dt}\right)$ of (40) can be determined from impedance as long as Lemma 1 holds. The command c^* of (43) is delayed by τ_p seconds in Fig. 3.2b using a binary off delay for relay coordination proposes. Motors that are electrically far from a substation may be set to trip faster than closer ones. During normal operation, c^* of (43) follows the command, $h^* \in \{0, 1\}$, from a home controller, q.v. Fig. 3.2b.

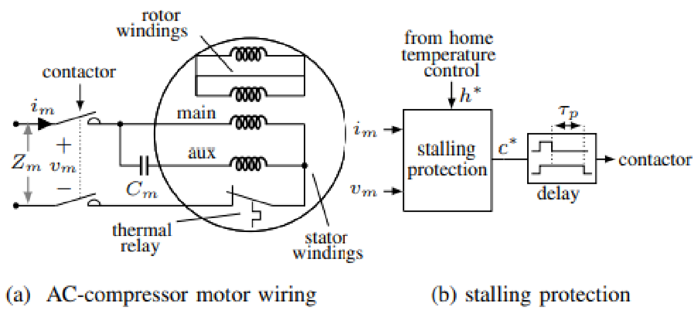

Figure 3.2 A/C-compressor motor including a two-pole contactor, a thermal relay, start-run capacitor C_m ∈ {C_start, C_start + C_run}, and proposed protection.

4. Case Studies

The dynamic performance of two hybrid PV power plants energizing the 13.8-kV radial feeder in Fig. 1.2 is analyzed via three case studies. Each power plant of Fig. 1.2 has four 2.5-MVA/0.69-kV IBRs as the one in Fig. 1.1. The dc-link of each IBR is powered by a 2.0-MW PV array and a 2.0-MWh BES. The first case study shows restoration performance under varying solar irradiance. The second and third case studies demonstrate the performance of the realistic compressor model in Section 2.2, the classical thermal relay in Section 3.1.1, and the proposed electronic stalling protection in Section 3.1.3 during FIDVR instances because of a fault in the 138-kV transmission circuit, q.v. Fig. 1.2. The sequential times when the breakers of Fig. 1.2 close, tc, and open, to, are in Table 4.1. The circuit breakers of both power plans are closed at t = 0.6 s.

These studies are conducted via a detailed EMT model of Fig. 1.2 which was implemented on PSCAD v5.0. The PSCAD simulations, using a 2 µs time step, were conducted on a desktop with 32 GB of RAM and a four-core 3.5-GHz Intel® Xeon® i3 processor. The time to simulate 40 s of reality was 50 min ca. The optimal set-point $v_{dc}^{*}$from Section 2.1.1 is computed using a custom FORTRAN script which is executed every 50 ms in PSCAD. In Fig. 1.2, the PV power plants are connected to the distribution feeder via two 138-kV sub-transmission lines and represented with frequency-dependent models [47]. Each distribution line of Fig. 1.2, e.g., the one connecting buses '0' and '1,' is modeled using a Π-section as in [28]. The physical and control parameters of the PV subsystem in Fig. 1.1 are in Table 4.2. Table 4.3 reports the parameters of the reciprocating compressor in Fig. 2.3 and the SPIM parameters. The SPIM is rated for 4.524 kW, 230 Vrms, and 60 Hz; the parameters are scaled from the ones explained in [44]. The compressor model is implemented via a custom FORTRAN script in PSCAD.

Table 4.1 Timed circuit breaker events for Fig. 1.2

breaker	H1	H2	C1	H3	H4	C2	C3	C4	C5	C6	C7
t_c (s)	5	5.5	7	7.5	8	10	13	16	19	22	25
t_o (s)	-	-	-	33.1	33.1	-	-	-	-	-	-

Table 4.2 Parameters for a hybrid PV inverter and its controls

par.	values	units	par.	values	units	par.	values	units	par.	values	units
C_{dc}	64.0	mF	L_l	0.1	mH	κ_{dc}	40	A/kJ	τ_v	20	ms
r_f	6.0	mΩ	κ_b	0.038	1/A	τ_{dc}	10	ms	κ_ω	0.05	p.u.
L_f	0.1515	mH	τ_b	2	ms	κ_i	0.3	V/A	v_{mn}	1.2	kV
C_f	0.9	mF	κ_c	0.038	1/A	τ_i	2.0	ms	$\bar{i}_l$	3.5	kA
r_l	15.7	mΩ	τ_c	2	ms	κ_v	0.54	A/V	$\underline{i}_l$	−3.5	kA
τ_l	0.54	ms	τ_{sw}	2	ms	$\bar{s}_c$	0.9	p.u.	$\underline{s}_c$	0.1	p.u.

Table 4.3 Compressor and SPIM parameters

compressor [48]			SPIM [44]		
par.	values	units	par.	values	units
r_s	0.01	m	r_r	0.74	Ω
r_p	0.022	m	$X_{\ell r}$	0.38	Ω
ℓ	0.095	m	r_{sm}	0.36	Ω
p_s	0.47/68	MPa/psi	$X_{\ell sm}$	0.50	Ω
p_d	1.034/150	MPa/psi	r_{sa}	1.29	Ω
$\mathcal{V}_1$	6.55×10^{-5}	m^3	$X_{\ell sa}$	0.58	Ω
$\mathcal{V}_2$	2.95×10^{-5}	m^3	X_m	16.72	Ω
$\mathcal{V}_3$	4.91×10^{-6}	m^3	C_{start}	120	μF
$\mathcal{V}_4$	1.03×10^{-5}	m^3	C_{run}	20	μF
D_f	500	Ns/m	N_{ma}	1/1.18	-
D_p	0.3	Ns^2/m			

4.1 Case I : Restoration Under Varying Solar Irradiance

The restoration of Fig. 1.2 is conducted as in Section 1.3.2. It considers the realistic compressor model in Section 2.2. Because the behavioral model is not suited to represent SPIM acceleration, q.v. Section 3.

The results of this case study are reported in Figs. 4.1–4.3. Figure 4.1 illustrates the dynamic performance of one hybrid GFM IBR as the one in Fig. 1.1 during step-wise variations of solar irradiance, Ir, in per unit of 1, 000 W/m2 . In particular, one can learn from Fig. 4.1 that: (A) Ir steps up from 0.5 to 1.0 at t = 10.0 s, then drops to 0.0 at t = 15.0 s to challenge control of the hybrid system. (B) At t = 15.0 s, the PV-array power Ppv → 0 MW because Ir → 0. (C) The dc-link voltage drops from 1.6 kV to vmn = 1.2 kV as a consequence of (B); recall vmn is defined in Section 2.2. (D) The battery SoC, sc, increases because Ppv > Pe for t ∈ [0, 15]s, q.v. Section 2. (E) sc decreases because Ppv < Pe for t ∈ (15, 20]s. (F) sc is almost constant because Ppv ≈ Pe for t ∈ (20, 30]s. (G) Battery power [q.v. Fig. 1.1] changes at t = 15.0 s from Pb = −1.75 MW charging [buck mode in Section 2.1.2] to Pb = 0.7 MW discharging [boost mode] because of (B). (H) The short-lived overshoots in ac power Pe [q.v. Fig. 1.1] are because of the start-up of SPIMs.

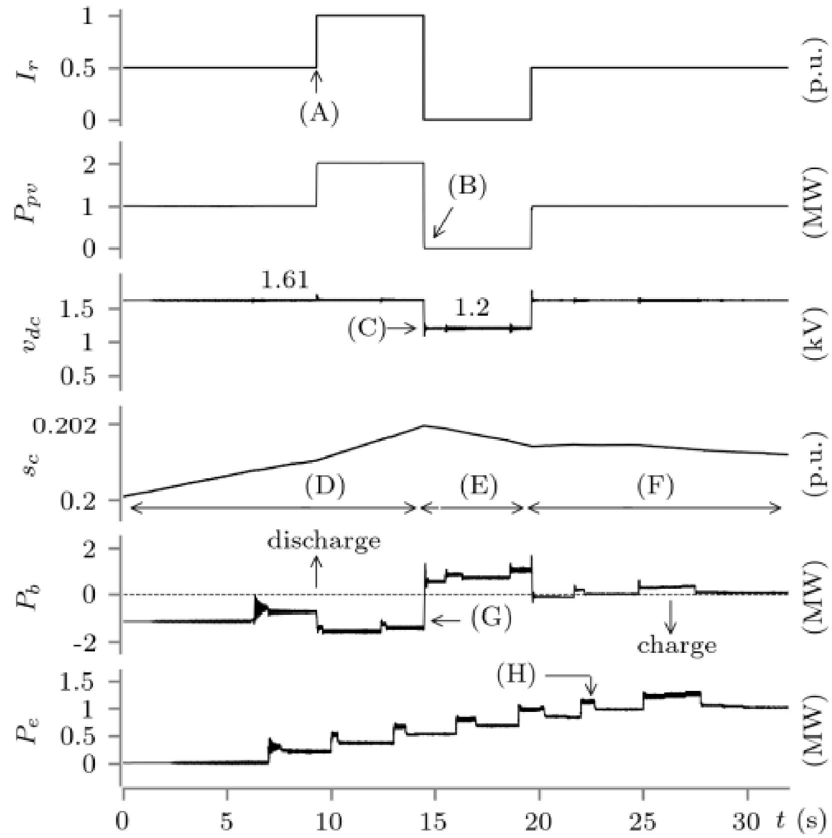

Figure 4.1 Case I: Performance of one IBR as in Fig. 1 during restoration.

The behaviors of voltages, currents, motor speeds, and OLTC of Fig. 1.2 during the restoration are reported in Fig. 4.2. Each $V_{\ i}$ and $I_{\ i}$ with i ∈ {0, 1, 2, . . . , 7} are: (i) the rms single phase voltage observed at the i-th 13.8-kV bus and (ii) rms single-phase current flowing into the SPIM and resistive load cluster, e.g., V3 and I3 in Fig. 1.2 correspond to phase 'b' (or φb). Each per-unit rotor speed $\omega_{m,i}$ in Fig. 4.2 corresponds to one machine within the Mi motor cluster of Fig. 1.2. In Fig. 4.2, one can learn that: (A) The rms phase voltages V1–V7 are as high as 1.08 p.u. when the feeder energizes because of the feeder capacitors. (B) The voltage dips for each Mi is because of the SPIM start-up current. (C) The start-up current of SPIM cluster M1, for example, is a high as 0.39 p.u. (1.0-kA base) which contrast its steady state current of 0.085 p.u. (D) The rotor speed of one motor in cluster M7 slowly rises from stand still in contrast to the others because V7 is relatively low. (E) The frequency, f_e, drops from 1.0 p.u. of 60 Hz to 0.991 p.u. at t = 19 s because of SPIM M5 acceleration, then it rises to 0.996 p.u. because the SPIMs reach about rated speed. Note f_e gradually deviates from the set-point ω_c^* = 1.02 p.u. of Fig. 1.3c because load is gradually energized. The fast transients of f_e, e.g., by t = 5.0 s, is because of transmission-line energization. (F) The OLTC tap increases to keep the voltage of bus '0' of Fig. 1.2 around 1.075 p.u. which is selected so to compensate for the voltage drop impacting M7.

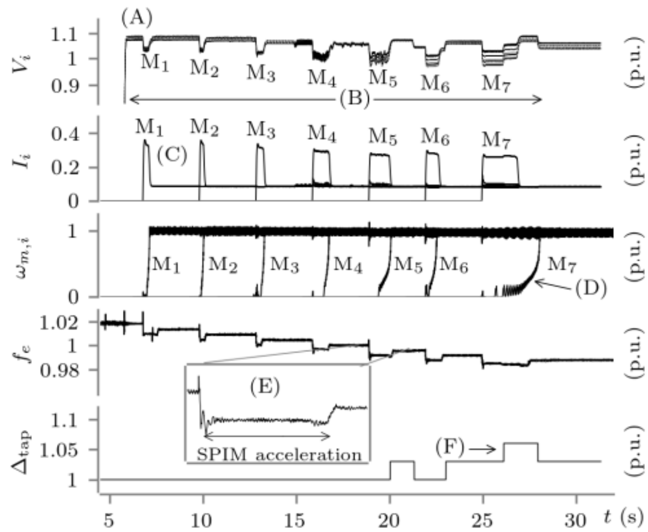

Figure 4.2 Case I: Behavior of voltages, currents, motor speed, grid frequency, and OLTC tap of Fig. 1.2 during the restoration.

Figure 4.3 reports the physical variables of one compressor in M7. During start-up, the compressor slowly changes its piston position x, pressure p, and volume V because T_e of (20) is relatively low due to V7 in Fig. 4.2.

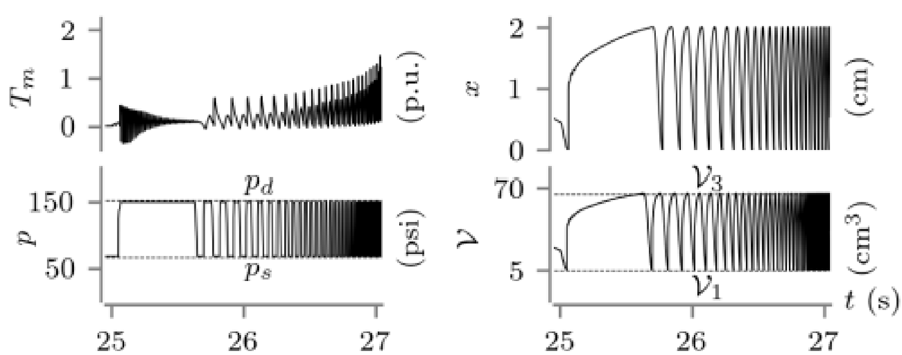

Figure 4.3 Case I: Behavior of a realistic compressor during M7 cluster start-up.

4.2 Case II : FIDVR Event with Realistic Compressor

This study contrasts the performance of Fig. 1.2 when the compressors are represented via: (i) the realistic model in Section 2.2.2 and (ii) the behavioral one in Section 2.2.1. The FIDVR event is triggered by a fault between phase 'c' and ground at the middle of the line between the breakers H3 and H4 in Fig. 1.2. The SPIMs are equipped with thermal relays having τ_{rly}= 10.0 s and $I_{m,rly}$ = 2.0 p.u. in its SPIM base, q.v. Section 4.1. The results are reported in Figs. 4.4–4.6.

One can learn from Fig. 4.4 that: (A) The realistic compressor model leads to voltage recovery at t = 36.9 whereas the behavioral counterpart at t = 37.5 s because mechanical torque impacts the current observed by the thermal relay. (B) Current withdrawn by the SPIMs driving the behavioral compressor model can be higher than when driving the realistic one. (C) After stalling, the SPIMs that drive the realistic compressor try to re-accelerate which contrasts the fully stalled state by SPIMs driving the behavioral compressor model. (D) The per unit temperature Θ of motor M7 is relatively high due to the longer start-up time, q.v. Fig. 4.2. In contrast, when using the behavioral model, the temperature of all motors is relatively low because the compressor is disconnected during startup [27, p. 26–27]. The motors trip when Θ reaches Θ*= 1.0 p.u.

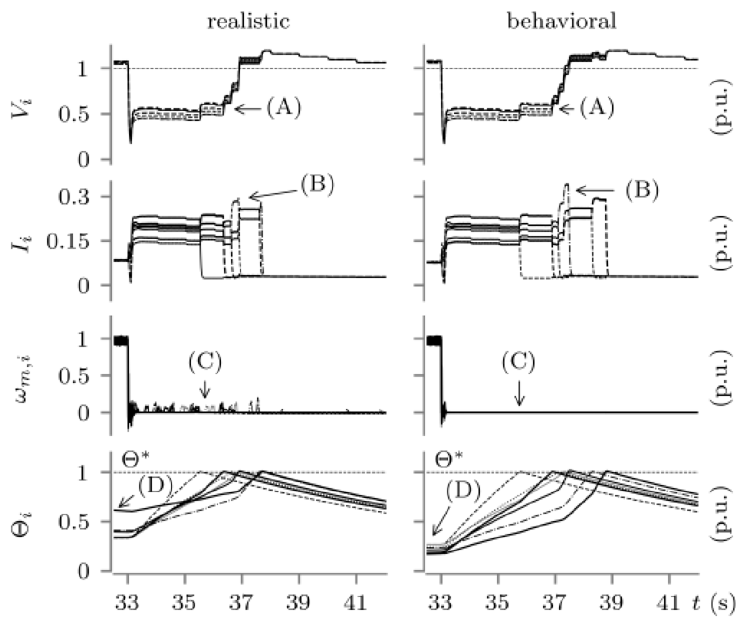

Figure 4.4 Case II: FIDVR performance using the realistic and behavioral compressor models.

Figure 4.5 reports the mechanical and electrical torques of one motor within the cluster M5. The realistic T_m resembles a combination of sinusoidal waveforms (q.v. Section 2.2.1) whereas the behavioral T_m is a triangular waveform. Notably, the electromagnetic torque T_e is different for the realistic and behavioral cases as depending on rotor speed and position which is impacted by T_m.

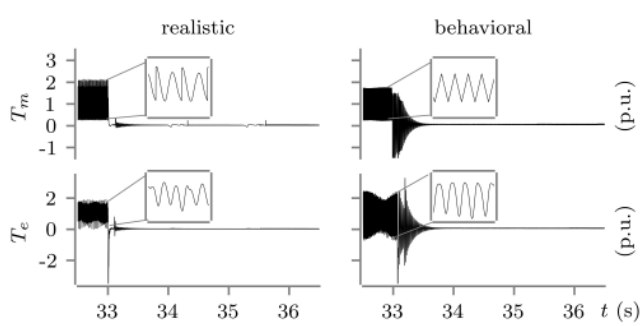

Figure 4.5 Case II: SPIM mechanical and electrical torque performance when using realistic and behavioral compressor models during a FIDVR event.

Figure 4.6, on the other hand, reports the currents and voltages at the terminals of one GSI of Fig. 1. In Fig. 4.6: (A) After the fault at t = 33.0 s, the instantaneous currents, i_{af} , can be as high as 3.7 kA which is 20% higher than the inverter rating 3.0 kA; inverters can withstand such short-lived currents. (B) The voltage waveforms do not recover to their rated values after the fault is cleared at t = 33.1 s because of motor stalling and GFM current limitation. (C) Reactive power, Q_e, automatically rises from 0.3 Mvar to 1.7 Mvar after the fault in phase 'c' is cleared because the IBR controls of Section 1.3.1 are engineered to regulate terminal voltages which remain relatively low during the FIDVR event, hence currents are steered to rated values.

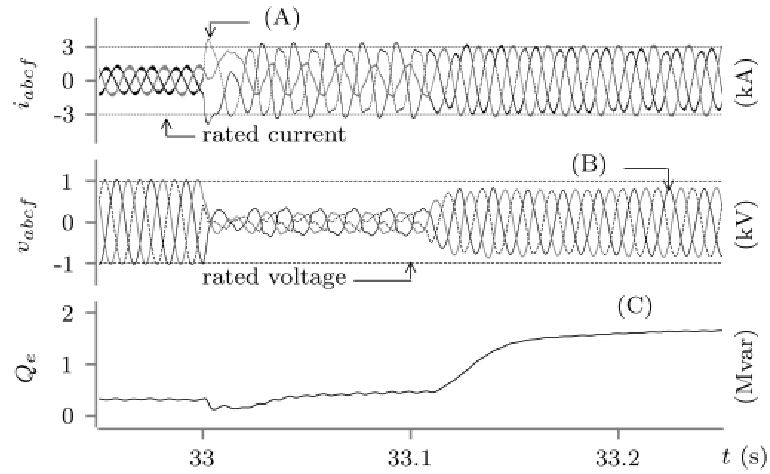

Figure 4.6 Case II: Inverter currents (i_af, i_bf , i_cf) voltages (v_abf , v_bcf , v_caf) and reactive power (Q_e) injected during the fault, q.v. Fig. 1.1.

4.3 Case III : FIDVR Event with Electronic Protection

This subsection contrasts the response of the electronic protection in Section 3.1.3 against the thermal relay in Section 3.1.1. It also considers the realistic compressor model in Section 2.2.2 during a FIDVR event. Here, each off delay time $\tau_{p,i}$= 1.0 + 0.25 · (7 − i), i = 1, 2, . . . , 7 (q.v. τ_p in Fig. 3.2b) is used in each Mi motor cluster of Fig. 1.2. This delay is judiciously selected so that, for example, the 6- th motor cluster trips after 0.25 s of the 7-th one if stalling happens in both clusters; note that M7 is at the feeder tail, hence coordinated for relatively fast tripping.

The results of this case are in Fig. 4.7 and 4.8. Figure 4.7 reports that: (A) The electronic relay leads to voltage recovery at t = 35.0 whereas the thermal relay counterpart at t = 37.5 s because electronic approach does not require heating for tripping. (B) When using the electronic protection, the rotor speed of clusters M1, M2, and M3 recover. In contrast, none of the cluster speeds recover when using the thermal relay

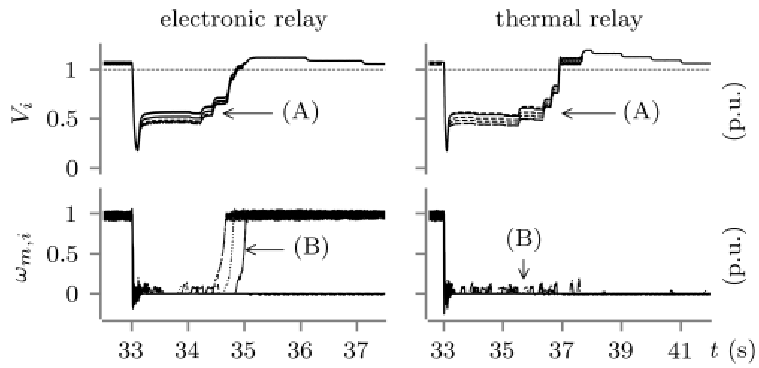

Figure 4.7 Case III: FIDVR performance using electronic and thermal relays.

In Fig. 4.8, one can recognize that: (A) The estimated impedance $|\widetilde{Z_{m,\iota}}|$ via (38) is lower than the set-point $|Z_m^*|$ = 0.27 p.u. for (43) after the fault at t = 33.0 s because the SPIM speeds are decreasing. (B) The impedances of the SPIM clusters that have tripped (M4, M5, M6, M7) are relatively large which is expected, q.v. (38). (C) Deceleration is correctly estimated on all motors after t = 33.0 s (q.v. (41), ϵ_ω = 0.01) which enables SPIM tripping during the FIDVR event. Recall that low-impedance and deceleration causes SPIM tripping, q.v. (43). Overall, the electronic relays contributed to the recovery of three SPIM clusters, i.e., 3×177 = 531 A/C units, q.v. Fig. 1.2. In contrast, the thermal relay did not support the speed recovery of any SPIM cluster.

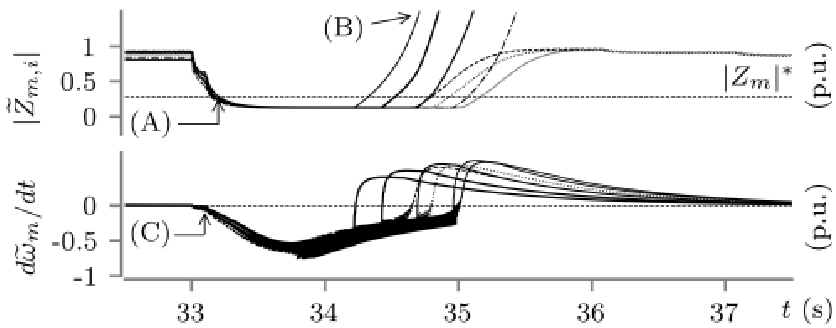

Figure 4.8 Case III: Estimated impedance and rotor deceleration/acceleration.

5. Conclusions

This work has engineered the technology for hybrid GFM IBRs so that they can: (i) optimally transfer power from a dc-coupled photovoltaic array and battery into an ac grid during restoration and (ii) stably withstand FIDVR events because of SPIM stalling. To that end, it was engineered in Section 2.1.2 anti-windup proportional-integral (PI) regulators to optimally charge and discharge the BES. It was shown in Section 4.1 that the controller performs well under varying solar irradiance during restoration. In Section 2.2.1, it was also derived a physics-based and computationally light compressor model for EMT studies of FIDVR events of grids with GFM IBRs and residential A/C units. In Section 4.2, the physics-based compressor model contrasts the performance of the behavioral representation discussed in Section 2.2.1. In Section 3.1.1, it was shown that IBR current limitations would delay the tripping of SPIM thermal relays which implied longer FIDVR events. Hence, an electronic protection was set forth in Section 3.1.3 to disconnect stalled SPIMs by estimating impedance and rotor deceleration. It was showcased in Section 4.3 that several A/C units can recover when using the electronic relay.

Overall, the developments and analyses of Sections 1.3-4.3 are instrumental to: (i) design hybrid PV plants for local reliability and resilience [35], [36] and (ii) conduct realistic EMT simulations of feeder restoration and FIDVR events 10 involving SPIMs and residential A/C compressors [30]. Future work will address hybrid configurations including wind and hydrogen fuel cells and FIDVR co-simulation in the EMT and phasor domains with a variety of A/C subsystems.

References

[1] "Solar futures study," U.S. Dept. of Energy, Tech. Rep., Sep. 2021.

[2] Lawrence Berkely Nat. Lab., Berkeley, CA, USA, Hybrid Power Plants: Status of Operating and Proposed Plants, 2022 Edition. (Aug. 18, 2022). Accessed: May. 12, 2023. [Online Video]. Available: https: //www.youtube.com/watch?v=LYFi4Gx7OAQ.

[3] Y. Lin et al., "Research roadmap on grid-forming inverters," Nat. Renewable Energy Lab., Tech. Rep. NREL/TP-5D00-73476, Nov. 2020.

[4] ——, "Pathways to the next-generation power system with inverter based resources: Challenges and recommendations," IEEE Electrific. Mag., vol. 10, no. 1, pp. 10–21, Mar. 2022.

[5] "FERC-NERC-regional entity joint review of restoration and recovery plans: Blackstart resources availability," FERC and NERC, Tech. Rep., May 2018.

[6] J. O'Brien et al., "Electric grid blackstart: Trends, challenges, and opportunities," Pacific Northwest Nat. Lab., Tech. Rep. PNNL-29118, Oct. 2020.

[7] P. M. Anderson, C. Henville, R. Rifaat, B. Johnson, and S. Meliopoulos, Power System Protection, 3rd ed. New York, USA: Wiley-IEEE Press, 2022.

[8] "NERC technical reference document, dynamic load modeling," North American Electric Reliability Corporation (NERC), Tech. Rep., Dec. 2016.

[9] B. Williams, W. Schmus, and D. Dawson, "Transmission voltage recovery delayed by stalled air conditioner compressors," IEEE Trans. Power Syst., vol. 7, no. 3, pp. 1173–1181, Aug. 1992.

[10] C. Taylor, "Concepts of undervoltage load shedding for voltage stability," IEEE Trans. Power Del., vol. 7, no. 2, pp. 480–488, Apr. 1992.

[11] D. Tziouvaras, "Relay performance during major system disturbances," in 60th Ann. Conf. Protective Relay Engineers, College Station, TX, USA, Mar. 27–29, 2007, pp. 251–270.

[12] S. M. Halpin, K. A. Harley, R. A. Jones, and L. Y. Taylor, "Slopepermissive under-voltage load shed relay for delayed voltage recovery mitigation," IEEE Trans. Power Syst., vol. 23, no. 3, pp. 1211–1216, Aug. 2008.

[13] H. Bai and V. Ajjarapu, "A novel online load shedding strategy for mitigating fault-induced delayed voltage recovery," IEEE Trans. Power Syst., vol. 26, no. 1, pp. 294–304, Feb. 2011.

[14] L. Taylor and S.-M. Hsu, "Transmission voltage recovery following a fault event in the metro Atlanta area," in Proc. IEEE Power Eng. Soc. Summer Meeting, Seattle, WA, Jul. 16–20, 2000.

[15] J. Kueck, D. Kosterev, J. Undrill, and J. Eto, "Voltage sag and recovery influence for modeling motor loads," in 2014 IEEE PES T&D Conf. and Expo., Chicago, IL, Apr. 14–17, 2014.

[16] S. M. Hashemi, M. Sanaye-Pasand, and M. Abedini, "Under-impedance load shedding: a new preventive action against voltage instability," IET Gen., Trans. & Distribution, vol. 13, no. 2, pp. 201–208, Nov. 2019.

[17] A. R. R. Matavalam and V. Ajjarapu, "PMU-based monitoring and mitigation of delayed voltage recovery using admittances," IEEE Trans. Power Syst., vol. 34, no. 6, pp. 4451–4463, Nov. 2019.

[18] Y. Dong et al., “An emergency-demand-response based under speed load shedding scheme to improve short-term voltage stability,” IEEE Trans. Power Syst., vol. 32, no. 5, pp. 3726–3735, Sep. 2017.

[19] B. Kroposki et al., “Achieving a 100% renewable grid: Operating electric power systems with extremely high levels of variable renewable energy,” IEEE Power Energy Mag., vol. 15, no. 2, pp. 61–73, Mar-Apr. 2017.

[20] R. H. Lasseter, Z. Chen, and D. Pattabiraman, “Grid-forming inverters: A critical asset for the power grid,” IEEE Trans. Emerg. Sel. Topics Power Electron., vol. 8, no. 2, pp. 925–935, Dec. 2020.

[21] J. Matevosyan et al., “A future with inverter-based resources: Finding strength from traditional weakness,” IEEE Power Energy Mag., vol. 19, no. 6, pp. 18–28, Nov-Dec. 2021.

[22] B. Kroposki et al., “UNIFI specification for grid-forming inverter-based resources-version 1,” Tech. Rep. UNIFI-2022-2-1, Dec. 2022.

[23] D. Venkatramanan et al., “Grid-forming inverter technology specifications: A review of research reports and roadmaps,” Tech. Rep. UNIFI2022-1-1, Nov. 2022.

[24] D. Mayclin. Air conditioning accounts for about 12% of U.S. home energy expenditures. [Online]. Available: https://www.eia.gov/ todayinenergy/detail.php?id=36692

[25] X. Quan et al., “Photovoltaic synchronous generator: Architecture and control strategy for a grid-forming PV energy system,” IEEE Trans. Emerg. Sel. Topics Circuits Syst., vol. 8, no. 2, pp. 936–948, Jun. 2020.

[26] F. Zhao et al., “Control interaction modeling and analysis of grid forming battery energy storage system for offshore wind power plant,” IEEE Trans. Power Syst., vol. 37, no. 1, pp. 497–507, Jan. 2022.

[27] Y. Liu, “Modeling of air-conditioner compressor single phase induction motor for transient analysis,” M.S. thesis, Dept. Elect. Eng., Arizona State University, Tempe, AZ, USA, 2012.

[28] Y. Liu, V. Vittal, J. Undrill, and J. H. Eto, “Transient model of air-conditioned compressor single phase induction motor,” IEEE Trans. Power Syst., vol. 28, no. 4, pp. 4528–4536, Nov. 2013.

[29] D. Kosterev et al., “Load modeling in power system studies: WECC progress update,” in Proc. IEEE Power Energy Soc. Gen. Meet. Convers. Del. Elect. Energy 21st Century, Pittsburgh, PA, Jul. 20–24, 2008.

[30] “Electromagnetic Transient Modeling for BPS Connected Inverter-Based Resources—Recommended Model Requirements and Verification Practices: NERC Reliability Guidelines,” North American Electric Reliability Corporation, Tech. Rep., Mar. 2023.

[31] P. Mitra, L. Sundaresh, and D. Ramasubramanian, “Stability of inverter-based resource (IBR) dominated systems with different types of local loads,” CIGRE Sci & Eng., no. 28, Mar. 2023.

[32] Q. Huang and V. Vittal, “Application of electromagnetic transienttransient stability hybrid simulation to FIDVR study,” IEEE Trans. Power Syst., vol. 31, no. 4, pp. 2634–2646, Jul. 2016.

[33] K. G. Ravikumar, S. Manson, J. Undrill, and J. H. Eto, “Analysis of faultinduced delayed voltage recovery using EMTP simulations,” in Proc. IEEE/PES Transmiss. Distribution Conf. Expo., Dallas, TX, May. 3–5, 2016.

[34] H. N. Villegas Pico and V. Gevorgian, "Blackstart capability and survivability of wind turbines with fully rated converters," IEEE Trans. Energy Convers., vol. 37, no. 4, pp. 2482–2497, Dec. 2022.
[35] North American Electric Reliability Corporation, "Statement of the North American Electric Reliability Corporation," in 2021 Ann. Commissioner-led Reliability Tech. Conf., Sep. 2021. [Online]. Available: https://www.ferc.gov/media/nerc-panel1
[36] "Performance, Modeling, and Simulations of BPS-Connected Battery Energy Storage Systems and Hybrid Power Plants: Reliability Guidelines," North American Electric Reliability Corporation, Tech. Rep., Jun. 2023.
[37] P. C. Krause, O. Wasynczuk, S. D. Sudhoff, and S. Pekarek, Analysis of Electric Machinery and Drive Systems, 3rd ed. New York, USA: Wiley-IEEE Press, 2013.
[38] M. Chandorkar, D. Divan, and R. Adapa, "Control of parallel connected inverters in standalone ac supply systems," IEEE Trans. Ind. Appl., vol. 29, no. 1, pp. 136–143, Feb. 1993.
[39] H. Jain, G.-S. Seo, E. Lockhart, V. Gevorgian, and B. Kroposki, "Blackstart of power grids with inverter-based resources," in Proc. IEEE Power Energy Soc. Gen. Meetings, Montreal, QC, Canada, Aug. 2–6, 2020.
[40] S. Roy and H. N. Villegas Pico, "Transient stability and active protection of power systems with grid-forming PV power plants," IEEE Trans. Power Syst., vol. 38, no. 1, pp. 897–911, Jan. 2023.
[41] M. G. Villalva, J. R. Gazoli, and E. R. Filho, "Comprehensive Approach to Modeling and Simulation of Photovoltaic Arrays," IEEE Trans. Power Electron., vol. 24, no. 5, pp. 1198–1208, May. 2009.
[42] HVAC School, USA, See What's Inside a Reciprocating Compressor. (Jul. 11, 2018). Accessed: May. 12, 2023. [Online Video]. Available: https://www.youtube.com/watch?v=F12WccGuiSw.
[43] S.-R. Hsieh and S. W. Shaw, "The dynamic stability and nonlinear resonance of a flexible connecting rod: Continuous parameter model," Nonlinear Dyn., vol. 4, pp. 573–603, Dec. 1993.
[44] P. C. Krause, "Simulation of unsymmetrical 2-phase induction machines," IEEE Trans. Power App. Syst., vol. 84, no. 11, pp. 1025–1037, Nov. 1965.
[45] D. Ndiaye and M. Bernier, "Dynamic model of a hermetic reciprocating compressor in on-off cycling operation," Appl. Thermal Eng., vol. 30, no. 8, pp. 792–799, 2010.
[46] S. Zocholl and G. Benmouyal, "On the protection of thermal processes," IEEE Trans. Power Del., vol. 20, no. 2, pp. 1240–1246, Apr. 2005.
[47] J. R. Marti, "Accurate modeling of frequency dependent transmission lines in electromagnetic transient simulations," IEEE Trans. Power App. Syst., vol. PAS-101, pp. 147–155, Jan. 1982.
[48] "Bristol reciprocating compressor H22J363ABCA," Accessed: May. 4, 2023. [Online]. Available: https://www.insco.com/2580858/p/n/ bristol-compressors-h22j363abca.

Part III

Testing and Validation Utilizing a Real-time Hardware-in-Loop (HIL) Transmission-Distribution Testbed

Sanjeev Pannala
Anurag Srivastava (Former Co-PI)
Liadi Akande, Graduate Student

Washington State University

For information about this project, contact

Sanjeev Pannala,
Washington State University,
School of Electrical Engineering and Computer Science,
Pullman, Washington, USA 99164-2752
Phone: 509-715-8183
Email: sanjeev.pannala@wsu.edu

Power Systems Engineering Research Center

The Power Systems Engineering Research Center (PSERC) is a multi-university Center conducting research on challenges facing the electric power industry and educating the next generation of power engineers. More information about PSERC can be found at the Center's website: http://www.pserc.wisc.edu.

For additional information, contact:

Power Systems Engineering Research Center
Arizona State University
527 Engineering Research Center
Tempe, Arizona 85287-5706
Phone: 480-965-1643
Fax: 480-727-2052

Notice Concerning Copyright Material

Table of Contents

List of Figures

List of Tables

1. Introduction

WSU team worked on three different topics including the ZIP load model estimation and network aggregation, T&D co-simulation, and FIDVR problem with hybrid Solar PV system.

Project team validated the developed approaches using a real-time simulation testbed that incorporates the sensing and communication delays involved in the monitoring and control strategy. The testbed utilized RTDS and OPAL-RT based co-simulation framework to exchange data between transmission-distribution operations for analyzing various operating conditions. Tests system was also used to synthesize the data required to validate the ZIP Load model estimation and verify the hybrid solar PV-assisted voltage support to address the FIDVR from single-phase induction motors within HVAC systems.

1.1 Report Organization

The remainder of this report is as follows. Section 2 discusses validation using a real-time hardware-in-the-loop (HIL) transmission-distribution testbed. Section 3 gives conclusion of this part of this report along with possible future extensions of this work.

2. Validation utilizing a real-time hardware-in-loop (HIL) transmission-distribution testbed

WSU team worked on three different topics including the ZIP load model estimation and network aggregation, T&D co-simulation and FIDVR problem with hybrid Solar PV system.

Project team validated the developed approaches using a real time simulation test bed that incorporates the sensing and communication delays involved for the monitoring and control strategy. The testbed utilized RTDS and OPAL-RT based co-simulation framework to exchange data between transmission-distribution operations for analyzing various operating conditions. Tests system was used to synthesize the data required for validating the ZIP Load model estimation and also verifying the hybrid solar PV assisted voltage support to address the FIDVR from single-phase induction motors within HVAC systems.

2.1 ZIP Load Model Estimation and Network Aggregation

Power system operation, planning and control relies heavily on accurate system load modelling. Load modelling in power systems has largely involved load models in transmission systems and aggregated load models for distribution systems at the substation level. However, with the advent of power electronics, distributed generation units and advanced automation, distribution systems can often act as generating sources thereby changing the traditional one-directional power flow model to a bi-directional one. Moreover, with the presence of different types of generating units in the form of renewables and other power electronic loads, distribution system load models are bound to be varying throughout the day. All this makes control and planning of the distribution grid a hard task to undertake from a transmission standpoint.

Load modelling in distribution systems is hence an important subject of research in recent years. Load modelling assists in various power system applications like Volt-Var control, power system planning, demand response, voltage stability, power system management, optimal power flow etc. Without accurate load modelling, power system operators will come up with non-optimal and even infeasible control setpoints which can be detrimental to reliable and safe power system operation and control. Generally, load models are of two types -(a) static, (b) dynamic and (c) composite. Static load models represent load models whose behavior is time-invariant in nature and which assists in steady state power system operation and control. Dynamic load models, on the other hand, are time-varying and assists in power system dynamics and stability issues. Composite load models are a combination of static and dynamic load models and are often used for a more realistic analysis of power systems. Finding accurate parameters in load models are classified in - (a) component-based and (b) measurement based [1], [2]. While component based methods involves mathematical or statistical models of load behavior, measurement based methods rely on measurements taken at the load level to assess its behavior on power systems. The major advantage of measurement based approaches is that load models can be derived for any type of loads integrated to the network once local measurements are available. However, input measurements need to be robust and clean to assess the parameters. The literature vastly provides methods to find equivalent load models for distribution systems aggregated at the transmission level [3]–[5]. The aggregated models are useful to the power system operators for taking decisions and control power system operation reliably in real-time. The aggregated load model is often represented in two major formulations depending on power system states like voltage and frequency- (a) ZIP (Z=constant impedance, I=constant current and P=constant power) form and (b) Exponential form. In this paper, we focus on ZIP model based load modelling using measurements obtained in distribution power systems.

Most of the literature involves aggregated ZIP load models of distribution systems from the transmission standpoint [6]. Our work, however, focuses mostly on accurately modelling distribution systems in presence of voltage dependent loads and distributed energy resources (DERs). This paper produced accurate ZIP load models that can be used to represent equivalent distribution load at bulk power system level.

This work provides two novel techniques to model distribution systems as a ZIP element utilizing field power and voltage measurements. The first technique is a least square estimation based, and the second one is a machine learning assisted load estimation approach. Both techniques are validated in IEEE 33 bus distribution system modeled in HYPERSIM Opal-RT, while the nodal power and voltage measurements are inputs to the approaches. The impact of DERs on load parameter estimation is captured in the estimation studies by considering different penetration levels. The estimated load parameters are tested with respect to the extended model in HYPERSIM Opal-RT, and both techniques provide reasonably good accuracy. The techniques are then validated considering the presence of Gaussian noise in measurement data.

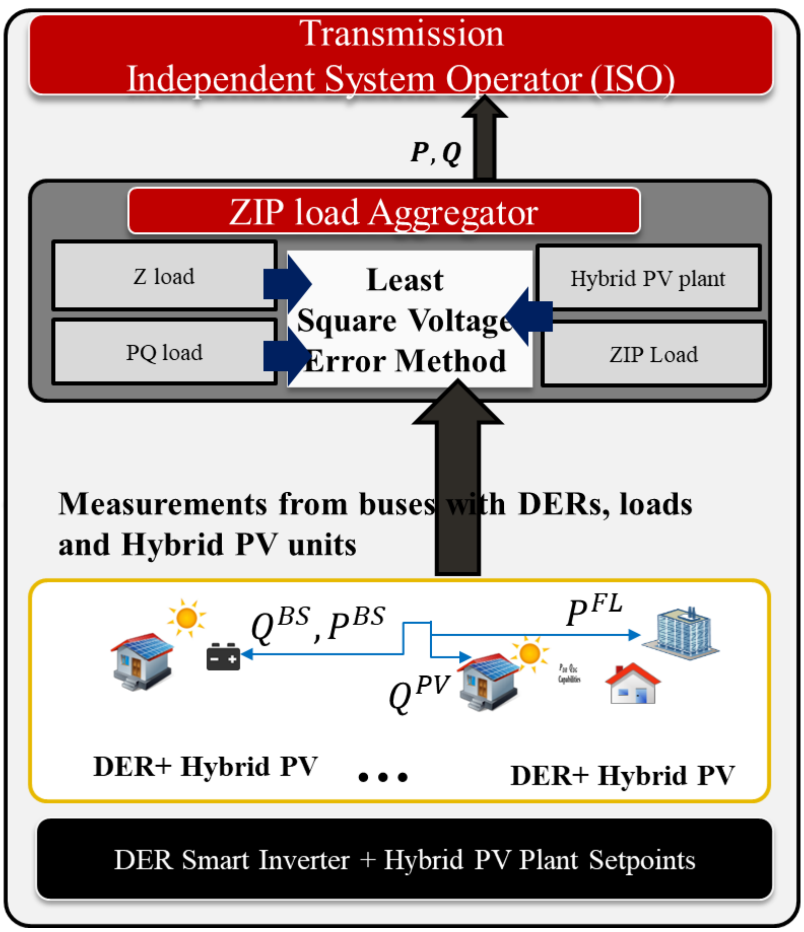

Figure 2.1 ZIP load model estimation

2.2 System Modeling

2.2.1 IEEE 33 Bus Distribution System without DER

The IEEE 33 bus radial feeder is considered in this work as shown in Fig. 2. Certain bus loads are modified and are made voltage dependent following the ZIP impedance representation. The loads represented in ZIP form consists of a load-fraction proportional to bus voltage, the other load fraction proportional to voltage squared and the rest is a constant power load. Both active and reactive power loads are modified to include voltage dependency in the feeder. As can be observed that loads in bus 21,22, 14, 15, 16, 17, 18, 29, 30, 31, 32, 33, 23, 24, 25 are modified to become voltage dependent loads.

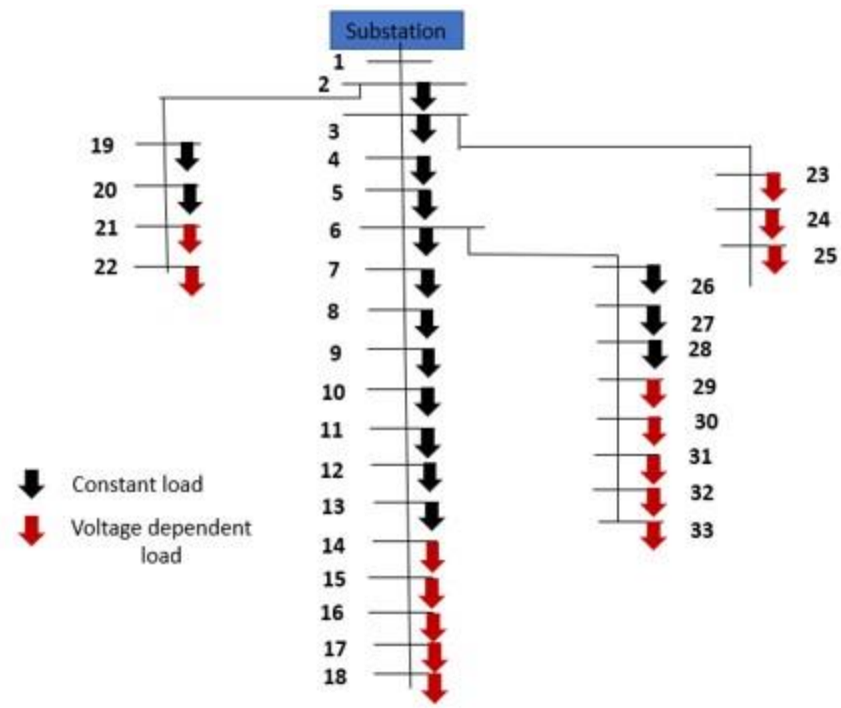

Figure 2.2 IEEE 33 bus feeder with voltage dependent loads

2.2.2 IEEE 33 bus feeder with DERs

Four photovoltaic systems (PV1, PV2, PV3, PV4) are integrated in the IEEE 33 bus feeder at buses 22, 18, 33 and 25 to represent the network with DERs. The capacities of the PV units are (PV1=930 kVA, PV2= 360 kVA, PV3= 1.32 MVA, PV4=1.1 MVA) respectively. C. Equivalent model of IEEE 33 bus feeder The IEEE bus feeder in Fig. 2 and the modified feeders with DERs in Fig. 3 are utilized as power system models to validate the proposed algorithms. Nodal power and voltage measurements from these models are input to the algorithms which then generate estimated load parameters. The load parameters are then used to reduce the extended models to reduced models as in Fig. 4. As can be observed that the sections 2-22, 6-18, 6-33 and 3-25 of the actual models are reduced to ZIP load equivalents connected at buses 2, 6, 6 and 3 respectively.

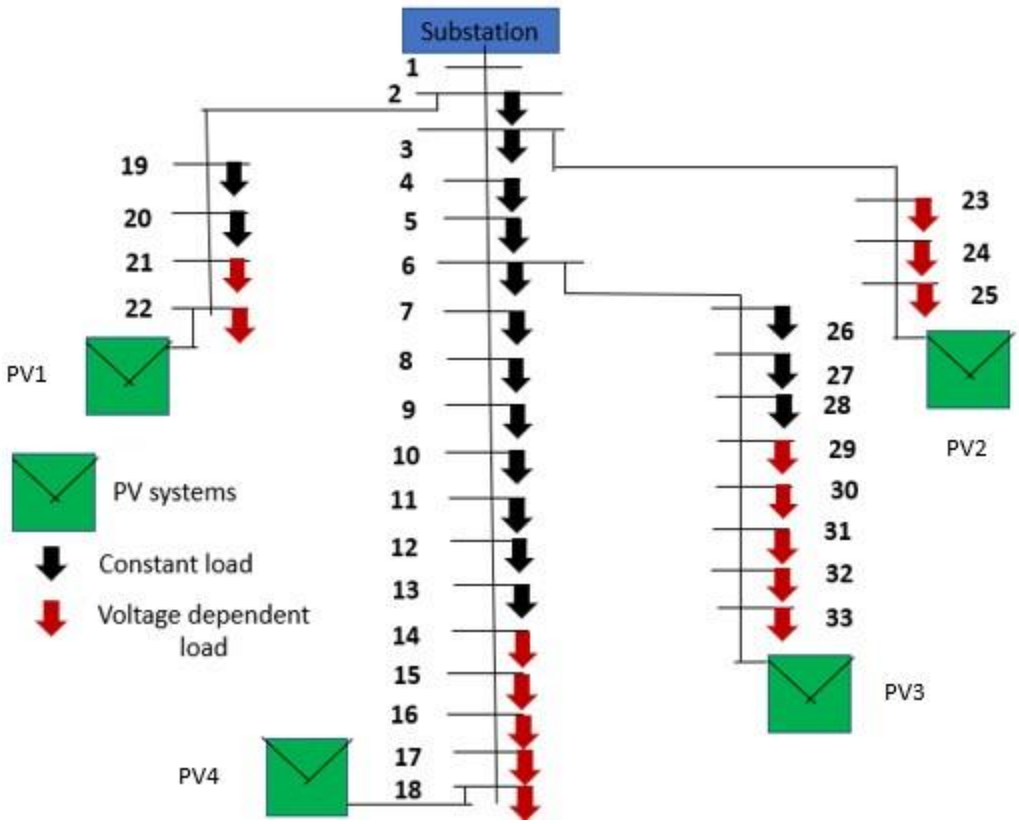

Figure 2.3 IEEE 33 bus feeder with voltage dependent loads and DERs

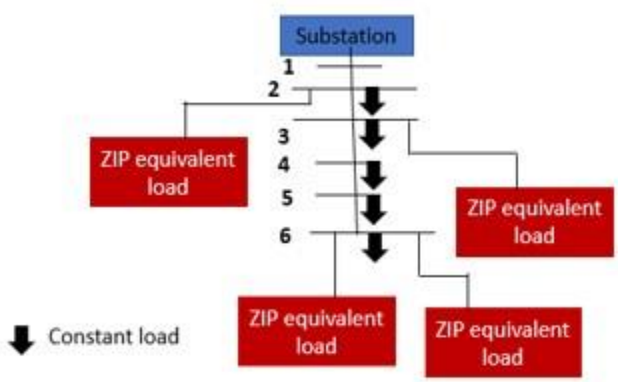

Figure 2.4 IEEE 33 bus feeder with voltage dependent loads and DERs

2.3 Approach

This section presents brief mathematical description of ZIP parameter estimation approaches and the estimation window extraction approach. The first approach is a least squares regression-based method called LSVE. The second method describes ML-based load parameter estimation and the framework for supervised learning-based estimation. Detailed information can be found in the paper that was archived for the project [7].

2.3.1 LS regression assisted with Variable Elimination (LSVE)

In this sub-section, we present the least squares problem for estimating ZIP load parameters, followed by the formulation of the regression problem with variable elimination. Given a set of voltage and power measurements from a µPMU at a specific bus between times t_{start} and t_{end}, the least-squares regression parameter estimation problem is specified as:

$$\min_{\lambda} \; f_p(\lambda)$$

Such that,

$$f_p(\lambda) = \sum_{t=t_{start}}^{t_{end}} |P(t) - \lambda A_i(t)|^2$$

$$A_i = [V(t)^2, V(t), 1]^T$$

$$\lambda = [\lambda_z, \lambda_i, \lambda_p]$$

$$\lambda_z \geq 0, \; \lambda_i \geq 0$$

$$\lambda_z = P_b\alpha_z, \; \lambda_i = P_b\alpha_i, \; \lambda_p = P_b\alpha_p$$

$$\alpha_z + \alpha_i + \alpha_p = 1$$

2.3.2 ML-based Load Parameter Estimation (ML-LPE)

This sub-section outlines the formulation of the load parameter estimation problem using supervised machine learning. The training data is labeled with target variables and numerical features. The ML learners are trained to predict the load parameters (αz, , αi , αp) once labeled training data is available. The ML based parameter estimation problem is mathematically defined as follow

$$X_f = F_{feats}(V, P)$$

$$\alpha_{zip} = f_{ml}(X_f)$$

$$\alpha_{zip} = [\alpha_z,, \; \alpha_i, \; \alpha_p]$$

Detailed discussion of formulations can be found in the archived paper [7].

2.4 Test Cases and Results Summary:

The IEEE 33 bus network along with DERs are modelled in OPAL-RT HYPERSIM. Thereafter, a system disturbance over a certain time period is introduced whereby the the system states change over the same time period. In this work, we introduce substation voltage change over a period of 10 seconds as the only system-level disturbance whereby loads are fixed and DER power outputs are fixed depending on their penetration levels. Power measurements in the form of active power flow and reactive power flow at branches (2-19), (3- 23), (6-7), (6-26) are recorded at 120 samples per seconds which is a standard sampling rate for phasor measurement units. Voltages at buses 2, 3, 6 are also recorded at the same sampling rate. The power and voltage measurements are then utilized by both approaches LSVE and MLLPE to estimate ZIP parameters.

In this work ML-LPE is implemented using random forest regressor trained using training data generated from large number of offline simulations. Consequently, these ZIP parameters are replaced in the actual model to get a reduced model. A steady state comparison of the actual and reduced model is also performed in this section. Both these evaluation approaches are considered for three scenarios - (a) IEEE 33 bus system without DERs ,(b) IEEE 33 bus system with DERs with 40% penetration and (c) IEEE 33 bus system with DERs with 100% penetration.

Case a): Without DERs

Table 2.1 Comparison of Bus voltages- (No DERs)

Bus voltages	Actual model	Reduced Model
Bus 2	0.997	0.997
Bus 3	0.983	0.983
Bus 4	0.972	0.982
Bus 5	0.962	0.973
Bus 6	0.952	0.964

Case b): With DERs and 40% penetration

Table 2.2 Comparison of Bus voltages- (DERs +40%)

Bus voltages	Actual model	Reduced Model
Bus 2	0.998	0.998
Bus 3	0.985	0.986
Bus 4	0.975	0.985
Bus 5	0.969	0.974
Bus 6	0.959	0.971

Case c): With DERs and 100% penetration

Table 2.3 Comparison of Bus voltages- (DERs +100%)

Bus voltages	Actual model	Reduced Model
Bus 2	0.998	0.998
Bus 3	0.987	0.986
Bus 5	0.978	0.978
Bus 6	0.971	0.971

2.4.1 Network Aggregation

This work aims to improve the observability of a given distribution system while providing a reduced-order system that can be reflected in the transmission side and save computational costs. In this task, we made network reduction for the distribution system and provide an aggregated DER/IBRs equivalent model, aggregated loss equivalent model that can be used for network reduction. Currently, we have selected the ZIP load model as a preliminary test and validated it. The ZIP load model is a static model to represent voltage dependency, which is defined as:

$$W_P = P_b(V(t)^2 Z_P + V(t) I_P + P),$$
$$W_Q = Q_b(V(t)^2 Z_Q + V(t) I_Q + Q),$$

where W_P and W_Q are the real and reactive power. The mathemtical model for real power satisfies the constraint $Z_P + I_P + P = 1$ for $Z_P \geq 0$, $I_P \geq 0$, and $P \geq 0$. Similarly, the conditions are also satisfied for W_Q. The purpose is to find the optimal parameters of the equivalent load model by parameter estimation and investigate the possibility of using ZIP parameters for the model aggregation and network reduction. Detailed netwrok aggregation results and analysis can be found in the paper [8].

2.5 T&D Co-Simulation Analysis

we have developed the transmission and distribution systems on two real-time simulators i.e RTDS and Opal-RT. As mentioned in the previous report, our work was to create an IEEE 9-bus transmission system on a Real-Time Digital Simulator (RTDS) and an IEEE 33-bus distribution feeder on OPAL-RT. In addition, the developed distribution system contains μ-PMUs, loads, and hybrid PV plants. The modeled PMUs on the testbed include virtual PMUs by processors in both simulators. For Transmission and Distribution (T&D) ElectroMagnetic Transient (EMT) co-simulations, we created a communication layer through TCP/IP for data exchange between the transmission and distribution systems.

Aggregated modified 33-node distribution network connected to Bus-6 of transmission system. Aggregated DER capacity of 10 MW is also connected to bus-6. Total Distribution system netload without DERs is 19.5MW. T&D co-simulation test setup can be seen in Fig.5

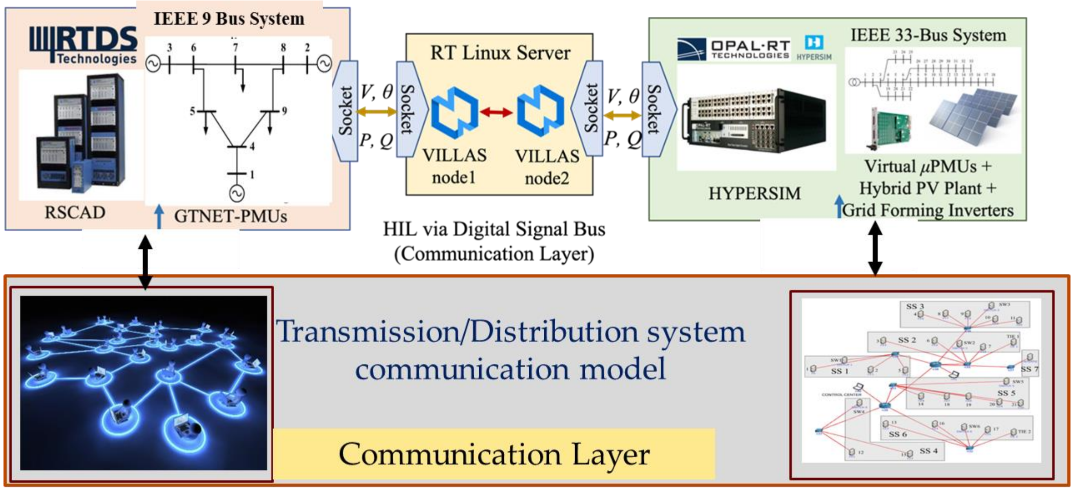

Figure 2.5 T&D Co-Simulation test setup.

2.5.1 Test performed for T&D co-simulation.

LLLG fault of 100 ms introduced in both cases on a line between bus6 and bus9 with and without DER. In later case, random noise with scaling 0.05 is introduced in simulations to DER control commands dispatched from the Transmission system. High noise produces PQ control error that causes oscillation in net load at bus6, which can be seen in the Fig. 7. There is no change in voltage waveform as the plan capacity is small compared to total transmission system load.

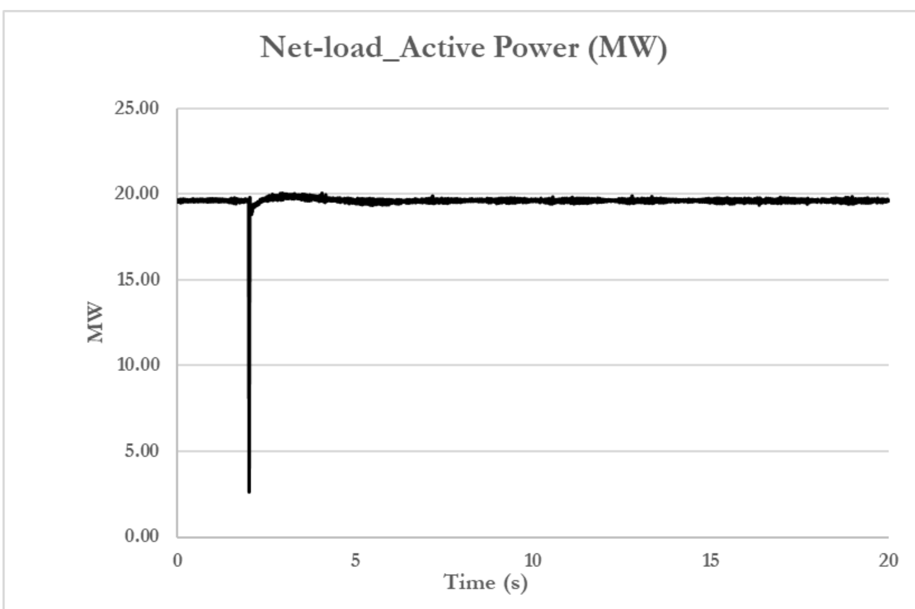

Figure 2.6 Net load power at Bus-6 without DER for fault at 2s

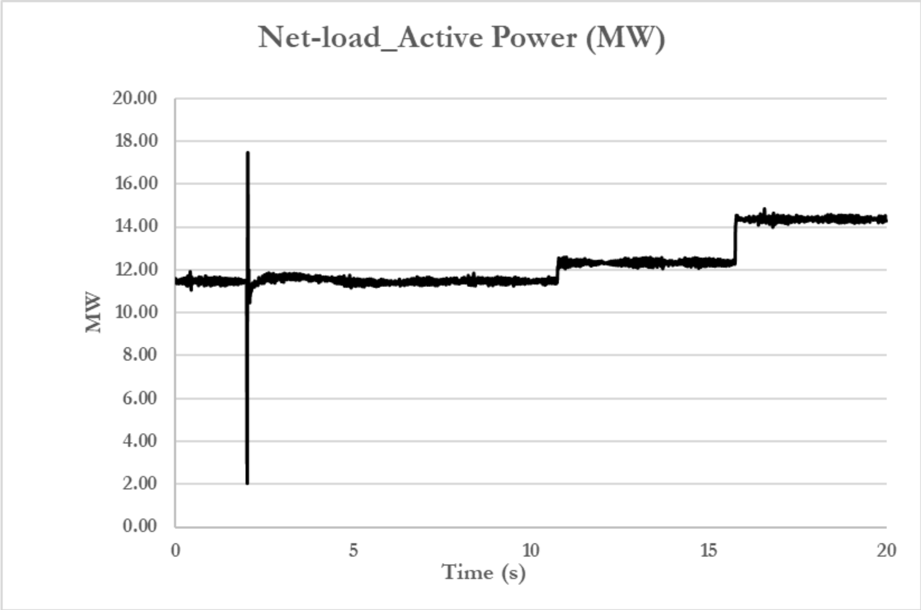

Figure 2.7 Net load power at Bus-6 with DER for fault at 2s

2.6 FIDVR with and without Hybrid Solar PV System

We worked on the delayed voltage recovery problem from single phasor motor pump load including agriculture pump, heating ventilation and air conditioning (HVAC) systems.

IEEE 9 bus system is considered as transmission system to reproduce the bulk power system characteristics, we worked with ISU team to get the FIDVR voltage behavior in digital real-time simulations. At bus-5, 27 MVA single phase HVAC motor load, three phase motor of 40 MVA and 67 MVA PQ load are connected to represent composite load from real-world scenario. Test system was modeled in RSCAD/RTDS software for transient simulations with 50 microsecond timestep for mimicking the true transient behavior of transmission systems. Standard capacities of IEEE 9 bus system are not altered for better comparison with ISU results. Test system in RSCAD is shown in Figure 2.8.

There are two cases considered for the study to verify the faster voltage recovery with hybrid solar PV systems.

Case 1: without hybrid solar PV

Case 2: with hybrid solar PV

A representative hybrid PV unit (5 MW PV+ 1.2 MW BESS) was placed at bus-3, which close to bus-9.

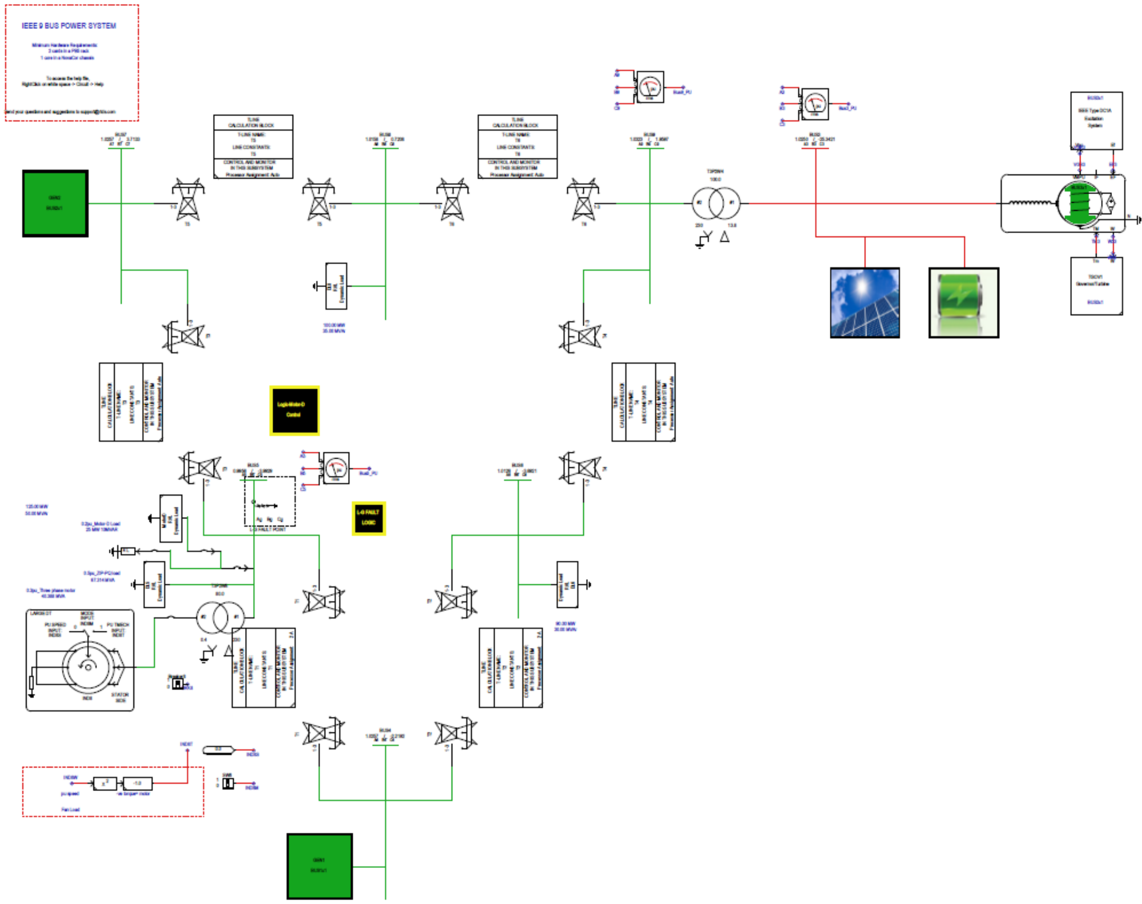

Figure 2.8 IEEE 9 Bus Transmission system with hybrid Solar PV system in RSCAD.

2.6.1 Transmission System Without Hybrid Solar PV

A LLLG fault of 100 ms is introduced at Bus-5 without enabling the hybrid solar PV plant. System bus voltage waveforms are shown in the Fig. 9. Fault induces delayed voltage recovery in bus-5 voltage as it consists of HVAC loads and there is minimal deviation in remaining bus voltages.

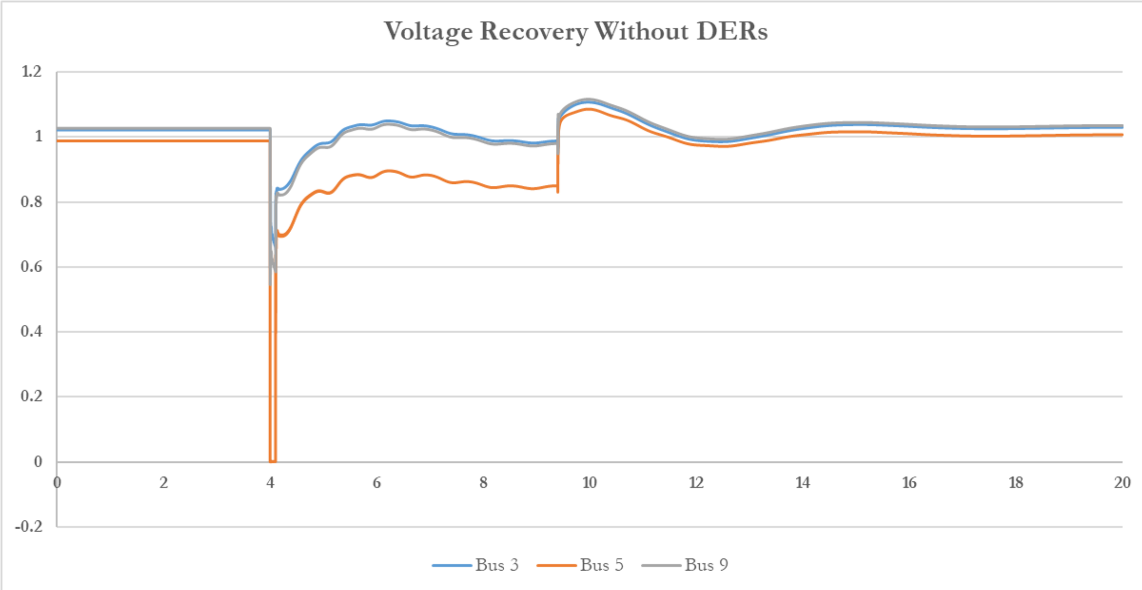

Figure 2.9 Bus voltage waveforms without Hybrid PV

2.6.2 Transmission System With Hybrid Solar PV

In this case, same LLLG fault of 100 ms is introduced at Bus-5 by including hybrid solar PV plant. System bus voltage waveforms are shown in the Fig. 10. Solar PV unit is operating in grid following mode and BESS was also activated in case of fault. Improved voltage recovery can be seen in the Fig. 10. A zoomed window captured in Fig. 12 clearly showcases improvement in voltage recovery with hybrid PV. Voltage enhancement was low due to limited hybrid PV plant capacity. There is a possibility of improving voltage better with higher hybrid solar PV units. Due to the limited processing capabilities of RTDS at WSU, low scale hybrid PV plant capacity was simulated in real- time simulators.

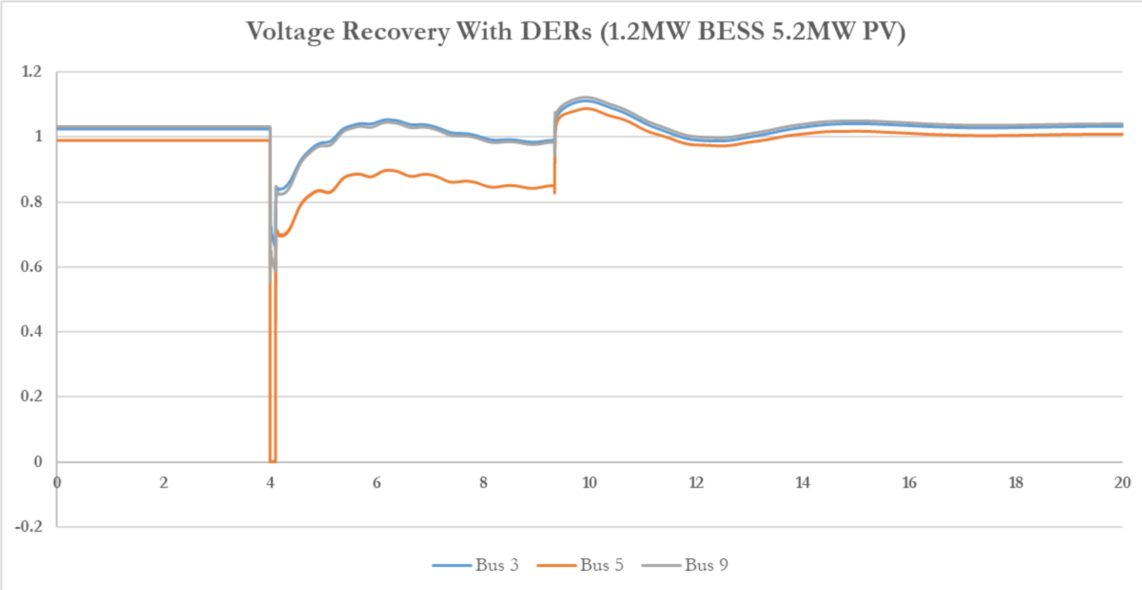

Figure 2.10 Bus voltage waveforms with Hybrid PV

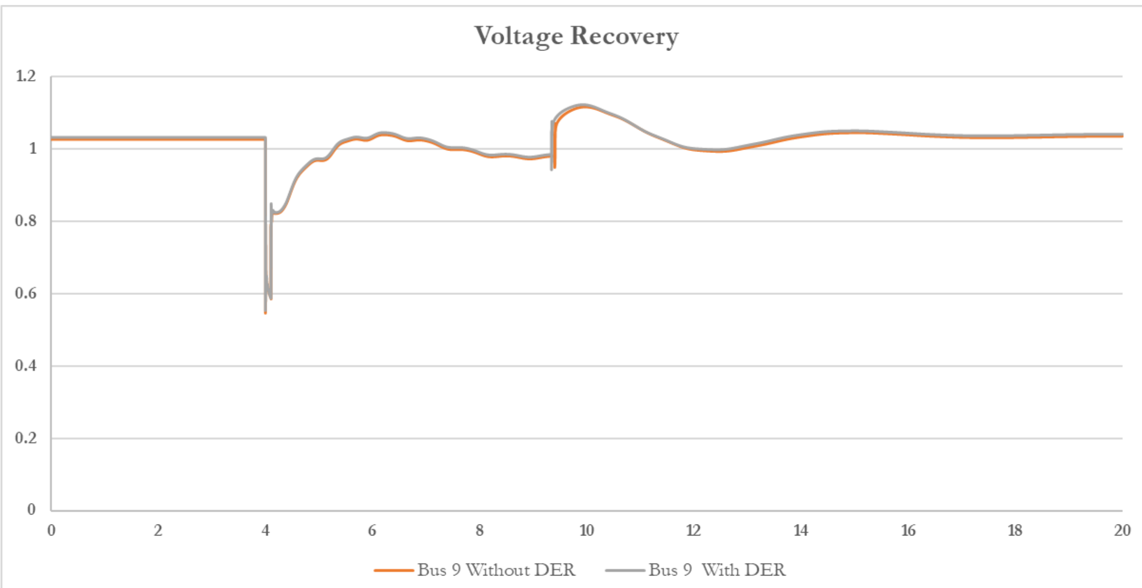

Figure 2.11 Comparison bus-9 voltage with and without Hybrid PV

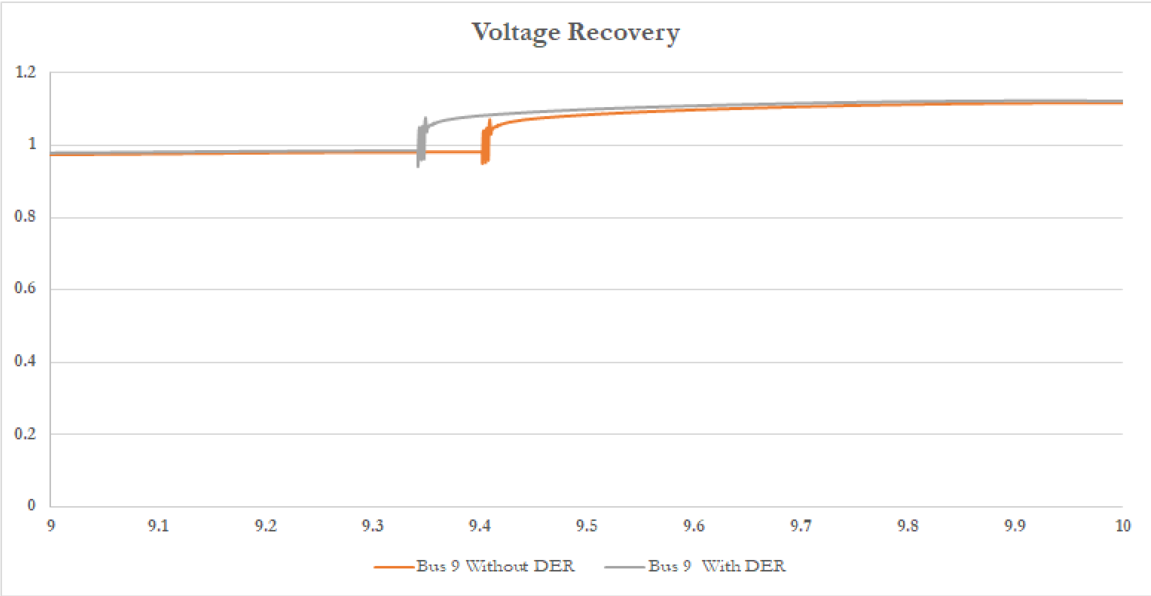

Figure 2.12 A zoomed window of Fig. 11

3. Conclusion

WSU team developed the ZIP load model estimation algorithms using LSVE and ML methods and also validated them using modified IEEE 33 bus system with DERs. T&D co-simulation was performed with IEEE 9 bus and 33 bus systems with help of RTDS and Opal-RT simulators. An enhanced voltage recovery of transmission system with hybrid PV plant is also demonstrated using real time digital simulators. WUS team worked with ISU team for model developments and successful validation.

3.1 Future work

- FIDVR Simulation with T&D Systems
- Testing voltage recovery improvement using hybrid PV Plants (i.e. PV+BESS) using Realtime Testbed
- Voltage stability assessment with aggregated ZIP loads plus DERs

References

[1] A. Shahsavari, M. Farajollahi, and H. Mohsenian-Rad, “Individual load model parameter estimation in distribution systems using load switching events,” IEEE Transactions on Power Systems, vol. 34, no. 6, pp. 4652– 4664, 2019.

[2] A. Arif, Z. Wang, J. Wang, B. Mather, H. Bashualdo, and D. Zhao, “Load modeling—a review,” IEEE Transactions on Smart Grid, vol. 9, no. 6, pp. 5986–5999, 2017.

[3] J. Ungerland, N. Poshiya, W. Biener, and H. Lens, “A voltage sensitivity based equivalent for active distribution networks containing grid forming converters,” IEEE Transactions on Smart Grid, vol. 14, no. 4, pp. 2825– 2836, 2023.

[4] S. D. ukic and A. T. Sari ´ c, “Dynamic model reduction: An overview of ´ available techniques with application to power systems,” Serbian journal of electrical engineering, vol. 9, no. 2, pp. 131–169, 2012.

[5] G. Chaspierre, G. Denis, P. Panciatici, and T. Van Cutsem, “A dynamic equivalent of active distribution network: Derivation, update, validation and use cases,” IEEE Open Access Journal of Power and Energy, vol. 8, pp. 497–509, 2021.

[6] M. Cui, J. Wang, Y. Wang, R. Diao, and D. Shi, “Robust time-varying synthesis load modeling in distribution networks considering voltage disturbances,” IEEE Transactions on Power Systems, vol. 34, no. 6, pp. 4438–4450, 2019.

[7] N.Patari, S.Rizvi ,S.Pannala and A.Srivastava “Aggregated ZIP Load Estimation Method for DER Integrated Distribution Systems “ communicated to IEEE PES Transaction (Archived).

[8] M. Menazzi, C. Qin and A. K. Srivastava, "Enabling Resiliency Through Outage Management and Data-Driven Real-Time Aggregated DERs," in IEEE Transactions on Industry Applications, doi: 10.1109/TIA.2023.3285516.